Hiroshima University Doctoral Thesis

Chemistry of Multiradicals Embedded in Cyclic Paraphenylene Units

(湾曲したパラフェニレンで繋がれたマルチラジカルの化学)

Basic Chemistry Program

Graduate School of Advanced Science and Engineering

Hiroshima University

March 2024

Yuki Miyazawa

Main Articles

(1) 1,3-Diradicals Embedded in Curved Paraphenylene Units: Singlet versus Triplet State and In-Plane Aromaticity.
Yuki Miyazawa, Zhe Wang, Misaki Matsumoto, Sayaka Hatano, Ivana Antol, Eiichi Kayahara, Shigeru Yamago, and Manabu Abe.
J. Am. Chem. Soc. **2021**, *143*(19), 7426−7439.

(2) Generation and Characterization of a Tetraradical Embedded in a Curved Cyclic Paraphenylene Unit.
Yuki Miyazawa, Zhe Wang, Sayaka Hatano, Ryukichi Takagi, Hideto Matsuoka, Naoka Amamizu, Yasutaka Kitagawa, Eiichi Kayahara, Shigeru Yamago, and Manabu Abe
Chem. Eur. J. **2023**, *29*, e202301009.

Supplemental Articles

(1) SOMO−HOMO Conversion in Triplet Carbenes.
Ryo Murata, Zhe Wang, Yuki Miyazawa, Ivana Antol, Shigeru Yamago, and Manabu Abe.
Org. Lett. **2021**, *23*, 4955−4959.

(2) Energetically More Stable Singlet Cyclopentane-1,3-diyl Diradical with π-Single Bonding Character than the Corresponding σ-Single Bonded Compound.
Qian Liu, Keita Onishi, Yuki Miyazawa, Zhe Wang, Sayaka Hatano, and Manabu Abe.
J. Am. Chem. Soc. **2023**, *145*(49), 27089−27094.

Table of Contents

Chapter 1. General Introduction

Section 1.1: Open-shell molecules.

Open-shell molecules with unpaired electrons have been widely studied today since Gomberg discovered the existence of triphenylmethyl radical (Figure 1.1a) in 1900,[1] due to their unique electronic structure and physical properties. Open-shell molecules with two unpaired electrons can be classified as biradicals or diradicals, depending on the strength of the interaction between the radicals (Figure 1.1b)[2]. When there is almost no interaction between the two radicals, they are classified as biradicals and are considered to behave as two doublet species. On the other hand, when there is interaction, they are classified as diradicals and can form singlet or triplet states depending on their spin state. Furthermore, diradicals can be classified into two types: localized and delocalized, and delocalized diradicals can be classified into two types: Kekulé and non-Kekulé. For example, Kekulé-type diradicals such as Thiele's hydrocarbons (n = 1, n: number of benzene rings in the linker site) and Tschitschibabin's hydrocarbons (n = 2, Figure 1.1c)[3] take a singlet ground state and can be constructed a quinoidal from described by the resonance structure. In addition to the increase in molecular stability due to the formation of a closed shell, the quinoidal form has a small HOMO-LUMO energy gap and is expected to exhibit high redox activity and photoresponsivity in the visible light region[4]. On the other hand, Non-Kekulé-type diradicals, such as Schlenk's hydrocarbons and tetramethyleneethane (TME) diradical (Figure 1.1d,e)[5], take the triplet ground state and have potential applications in paramagnetic materials, but they are generally unstable at room temperature and the generation is limited to low-temperature matrix conditions to inhibit polymerization. However, kinetically stabilized triangulene (Figure 1.1f) has a triplet ground state and is stable at room temperature, as reported[6]. Furthermore, the development of paramagnetic molecules is anticipated. The spin state of an open-shell molecule plays a significant role in physical properties, and controlling the spin state is a major research topic.

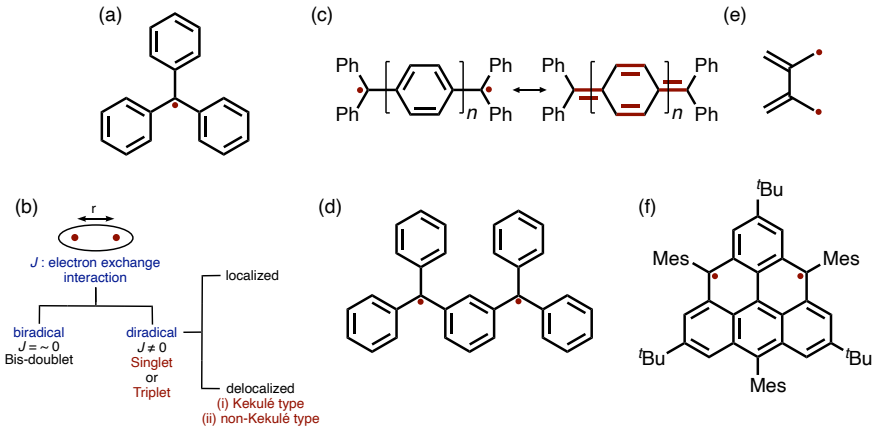

Figure 1.1: (a) Triphenyl methyl radical. (b) Types of diradicals. Selected example of organic diradicals. (c) Thiele's hydrocarbon (n = 1) and Tschitschibabin's hydrocarbon (n = 2). (d) Schlenk's hydrocarbon (e) tetramethyleneethane diradical. (f) Kinetically stabilized triangulene.

Section 1.2: Chemistry of cyclopentane-1,3-diradical and controlled of their ground spin state.

One of the examples of localized diradical, cyclopentane-1,3-diradical (**DR**, Figure 1.2a**)**, their ground spin state can be controlled by the M atom at the 2-position and substituent R effects have been reported[2,7]. When spatially distant two p orbitals on the radical carbons of the 1,3-position interact (through space interaction, Figure 1.2b), they are divided into two types of molecular orbitals: the energetically stable bonding orbital Ψ_S and the energetically unstable Ψ_a. In addition to this, the interaction with the orbital in 2-position leads to further splitting of the molecular orbital (through bond interaction, Figure 1.2c). If the substituent R at 2-position is an electron-withdrawing group (EWG) such as OH and F groups (M = C), Ψ_S orbital interacted with pseudo p orbital formed by the energetically lower $\sigma^*_{C\text{-}EWG}$. As a result, the energy level of Ψ_S was stabilized and take the singlet ground state (Type 1 diradical). On the other hand, in the case of an electron-donating group (EDG) such as H, CH_3, and SiH_3 group, the Ψ_S orbital interacted with pseudo p orbital formed by the energetically high $\sigma_{C\text{-}EDG}$. As a result, the energy level of Ψ_S was destabilized and take the triplet state in the case of R = H and CH_3 due to the degenerate two orbitals Ψ_S and Ψ_a, and the singlet state in the case of R = SiH_3 (Type 2 diradical). An exception is when the element M in the 2-position is another 14-element group such as Si or Ge, the ground spin state is singlet even in the case of R = H and CH_3. The reason is that the energy of $\sigma_{M\text{-}EDG}$ is lower than that of $\sigma_{C\text{-}EDG}$, making weaker through-bond interaction.

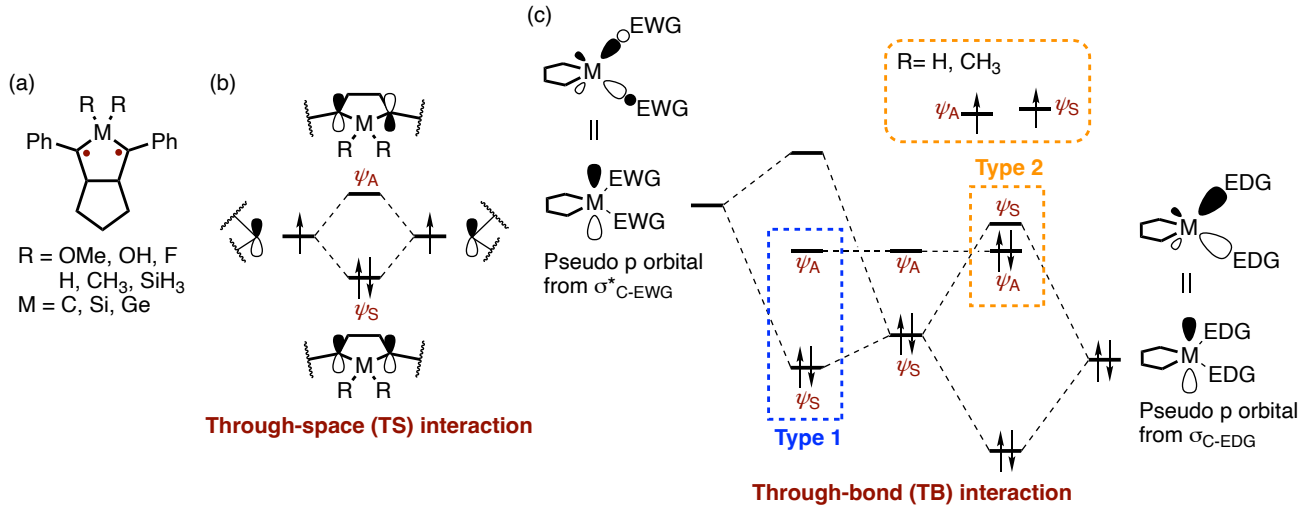

Figure 1.2: (a) cyclopentane-1,3-diradical. (b) Through-space interaction of p-orbitals at 1,3-position of cyclopentane-1,3-diradical. (c) Through-bond interaction of substituent effect at 2 positions.

Section 1.3: The orbital interaction of benzene and curved benzene.

The simplest aromatic hydrocarbon, benzene, has two degenerate orbitals and exists stably as a closed-shell molecule. Considering the curve of the 1,4-position in benzene[8], the energy levels of Ψ_3 and Ψ_5, which have no orbital interaction at the 1,4-position, are expected to remain almost unchanged (Figure 1.3). On the other hand, the orbital Ψ_2 is expected to be destabilized due to the loss of interaction with the neighboring p orbital and the antibonding interaction due to the inversion of the 1,4-position p orbital. In contrast, the Ψ_4 orbital is expected to be stabilized by the bonding interaction due to the inversion of the p orbital at the 1,4-position. As a result, diradicality is expected to occur at the 1,4 positions because curving the benzene ring would generate a new degenerate orbital. A possible method of forming of the curved benzene system is to construct a macrocyclic structure.

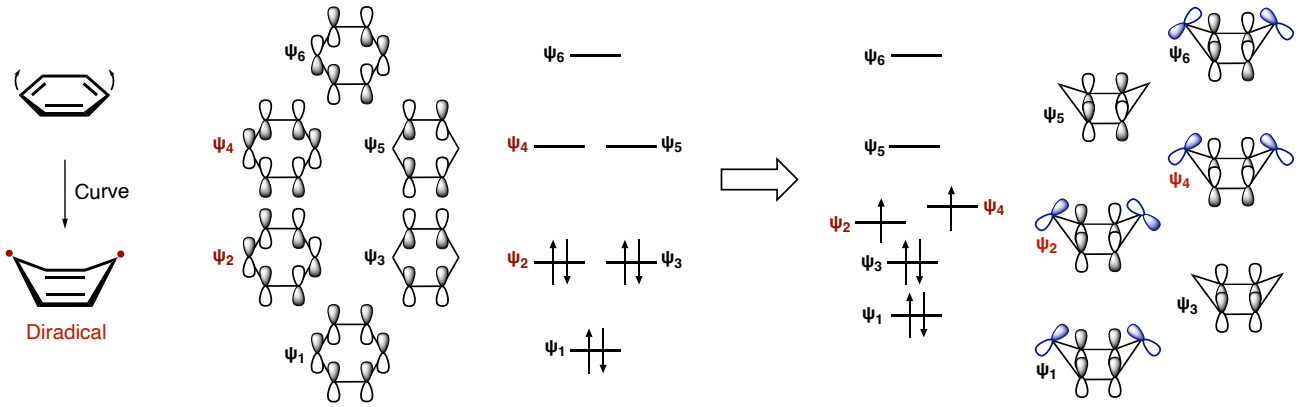

Figure 1.3: The orbital interaction of benzene and curved benzene.

Section 1.4: Chemistry of cycloparaphenylene.

Cycloparaphenylene (CPP), in which all benzene rings are connected at the para position to form a beautiful ring structure, has long been proposed as the smallest unit of carbon nanotubes, but synthesis has not been achieved due to its high strain energy derived from the ring structure. However, the first synthesis was reported in 2008 by Jasti and coworkers [9](Figure 1.4a), and since then, Itami and Yamago have reported a number of synthetic methods (Figure 1.4b, c) and the unique ring size property of CPPs[10]. Recently, the use of gold complexes has been reported to give high yields of 6CPP under mild conditions[11] (Figure 1.4d). One characteristic of CPPs is having a unique HOMO-LUMO energy gap[12] (Figure 1.5). In the case of linear paraphenylene molecules, when the number of benzene rings in the molecule increases, the conjugated system expands, and the energy gap becomes smaller. While in the case of CPP, the HOMO-LUMO gap becomes smaller as the number of benzene rings decreases. This behavior is caused by an increase in the contribution of the quinoidal form due to spin interactions induced by distortion of the benzene ring in the macrocyclic structure.

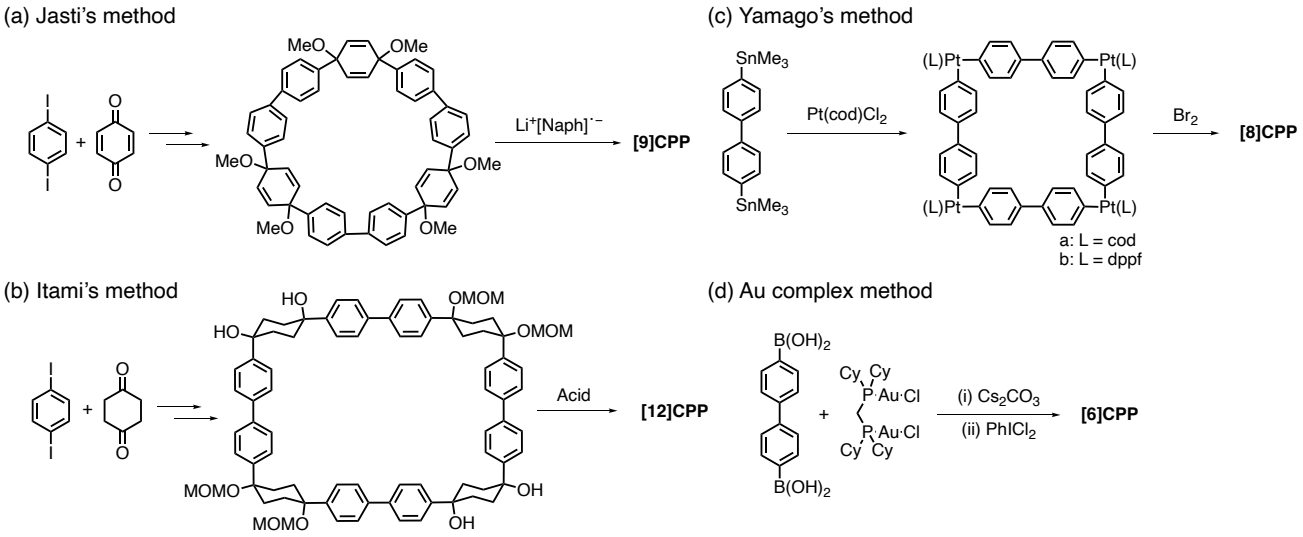

Figure 1.4: Selected example of synthesis method of cycloparaphenylene.

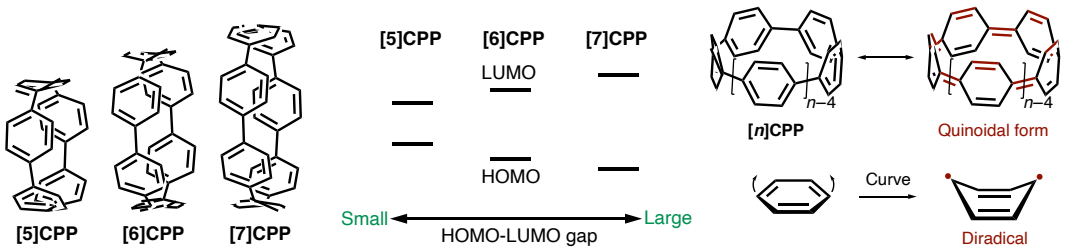

Figure 1.5: Unique HOMO-LUMO energy gaps of cycloparaphenylene and factors.

Section 1.5: The study of aromaticity.

One of the important concepts in organic chemistry is aromaticity. The stability and reactivity of compounds can be understood by the aromaticity concept. Hückel's rule is a well-known for determining whether compounds have aromaticity or not[13]. The rule predicts that cyclic conjugated planar polyenes in the $(4n+2)\pi$ system will exhibit aromaticity, while those in the $4n\pi$ system will exhibit anti-aromaticity. Molecular orbital theory can be used to explain how this aromaticity is produced (Figure 1.6a). Considering the molecular orbitals of 1,3,5-hexatriyne and benzene as an example, a total of six p orbitals can be written for hexatriyne, and the six p electrons are accommodated in order from the lowest energy orbital Ψ_1 to Ψ_3. The HOMO-LUMO gap ΔE would be between Ψ_3 and Ψ_4. Next, consider the case where the carbons at the 1 and 6 positions of hexatriyne are joined to form benzene. If the p orbitals on the carbons at the 1 and 6 positions are in phase, they are stabilized, and if they are out of phase, they are destabilized. As a result, the Ψ_3 orbital is more stable, the Ψ_4 orbital is destabilized, ΔE is larger, and the molecule becomes more stable. In planar molecules such as benzene, the p orbitals lie perpendicular to the planar surface, while in the case of CPP, the p orbitals lie parallel to the planar surface (Figure 1.6b). Therefore, it can be expected to have in-plane aromaticity due to the p orbital through the entire ring, which is considered to be an annulene[14]. However, in the case of CPP, they are 4nπ system and are expected to have in-plane antiaromaticity. While in the case of two-electron oxidized CPP dications, they exhibit in-plane aromaticity and have been reported to be isolable and photo responsive in the near infrared region[15].

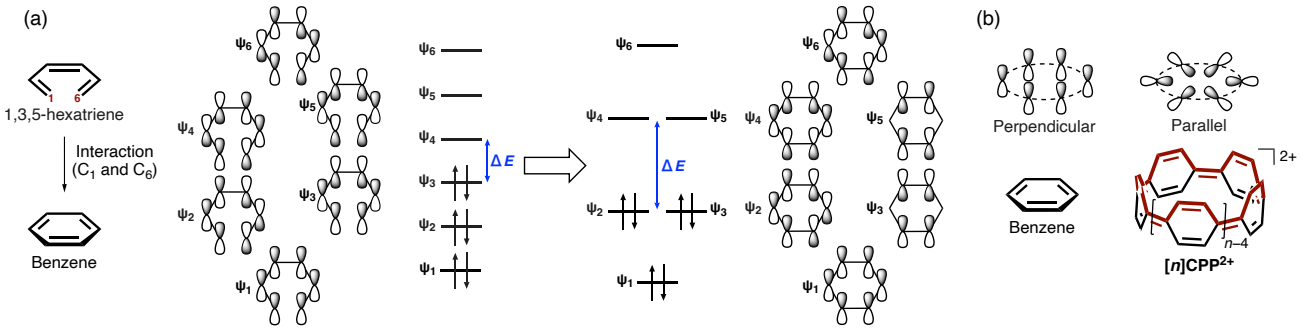

Figure 1.6: (a) Aromatic stabilization of benzene. (b) Two types of arrangement of p-orbitals.

Section 1.6: The study of this thesis.

In this study, we focused on multiradicals in the macrocyclic structure (Figure 1.7). For the generation of multiradical in the ring structure, the use of photodenitrogenation of the azo moiety (**AZ**) was considered. In the case of multiradical in the macrocyclic structure, not only bonding interactions through π-conjugation system between radicals, but also diradicality of 1,4-posion in benzene induced by the ring structure are expected to construct a quinoid form with a longer π-conjugated system than that of the linear one. In addition, there have been few studies on the behavior of multiradical in the macrocyclic framework, and what kind of spin states they form, as well as their physical properties and reactivity, are of interest. In the first chapter, the properties of the macrocyclic azo molecule **AZ-6CPP** and the behavior of the photogenerated diradical **DR-6CPP** were investigated, and in the second chapter, the properties of **2AZ-8CPP** with two azo units and the behavior of the photogenerated tetraradical **2DR-8CPP** were investigated.

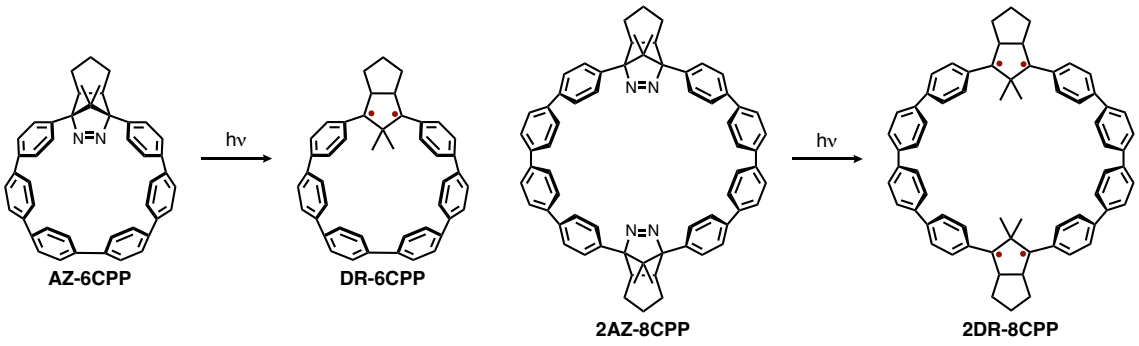

Figure 1.7: Macrocyclic azo compound and photo-generated multiradical.

Reference.

1. (a) Gomberg, M. *J*. *Am*. *Chem*. *Soc*. **1900**, *22*, 757. (b) Gomberg, M. *Chem*. *Ber*. **1900**, *33*, 3150.
2. Abe, M. *Chem*. *Rev*. **2013**, *113*, 7011–7088.
3. (a) Thiele, J.; Balhorn, H. *Chem*. *Ber*. **1904**, *37*, 1463. (b) Tschitschibabin, A. E. *Chem*. *Ber*. **1907**, *40*, 1810. (c) Montgomery, L, K.; Huffman, J. C.; Jurczak, E. A.; Grendze, M. P. *J*. *Am*. *Chem*. *Soc*. **1986**, *108*, 6004−6011.
4. (a) Sun, Z.; Ye, Q.; Chi, C.; Wu, J. *Chem*. *Soc*. *Rev*. **2012**, *41*, 7857–7889. (b) Hwang, H.; Khim, D.; Yun, J.-M.; Jung, E.; Jang, S.-Y.; Jang, Y. H.; Noh, Y.-Y.; Kim, D.-Y. *Adv*. *Funct*. *Mater*. **2015**, *25*, 1146–1156 (c) Venkateshvaran, D.; Nikolka, M.; Sadhanala, A.; Lemaur, V.; Zelazny, M.; Kepa, M.; Hurhangee, A.; Kronemeijer, J.; Pecunia, V.; Nasrallah, I.; Romanov, I.; Broch, K.; McCulloch, I.; Emin, D.; Olivier, Y.; Cornil, J.; Beljonne, D.; Sirringhaus, H. *Nature*. **2014**, *515*, 384–388.
5. (a) Schlenk, W.; Brauns, M. *Chem*. *Ber*. **1915**, *48*, 661. (b) Matsuda, K.; Iwamura, H. *J*. *Am*. *Chem*. *Soc*. **1997**, *119*, 7412–7413
6. Arikawa, S.; Shimizu, A.; Shiomi, D.; Sato, K.; Shintani, R. *J*. *Am*. *Chem*. *Soc*. **2021**, *143*, 19599−19605.
7. (a) Abe, M.; Ishihara, C.; Tagegami, A. *J*. *Org*. *Chem*. **2004**, *69*, 7250–7255. (b) Abe, M.; Abe, M.; Ye, J.; Mishima, M. *Chem*. *Soc*. *Rev*. **2012**, *41*, 3808–3820.
8. (a) Bickelhaupt, F. *Pure Appl*. *Chem*. **1990**, *62*, 373−382. (b) Jenneskens, L.W.; Vaneenige, E.N.; Louwen, J.N. *New J*. *Chem*. **1992**, *16*, 775−779. (c) Dewar, M.J.S.; Wade, L.E. *J*. *Am*. *Chem*. *Soc*. **1977**, *99*, 4417−4424. (d) Matsumoto, M.; Antol, I.; Abe, M. *Molecules*. **2019**, *24*(1), 209.
9. Jasti, R.; Bhattacharjee, J.; Neaton, J. B.; Bertozzi, C. R. *J*. *Am*. *Chem*. *Soc*. **2008**, *130*, 17646–17647.
10. (a) Takaba, H.; Omachi, H.; Yamamoto, Y.; Bouffard, J.; Itami, K. *Angew*. *Chem*. *Int*. *Ed*. **2009**, *48*, 6112–6116. (b) Yamago, S.; Watanabe, Y.; Iwamoto, T. *Angew*. *Chem*. *Int*. *Ed*. **2010**, *49*, 757–759.
11. Yoshigoe, Y.; Tanji, Y.; Hata, Y.; Osakada, K.; Saito, S.; Kayahara, E.; Yamago, S.; Tsuchido, Y.; Kawai, H. *JACS Au*. **2022**, *2*, 1857–1868.
12. Iwamoto, T.; Watanabe, Y.; Sakamoto, Y.; Suzuki, T.; Yamago, S. *J*. *Am*. *Chem*. *Soc*. **2011**, *133*, 8354−8361.
13. (a) Hückel, E. *Z*. *Physik* **1931**, *70*, 204–286. (b) Hückel, E. *Z*. *Physik* **1931**, *72*, 310–337. (c) Hückel, E. *Z*. *Physik* **1932**, *76*, 628–648.

14 (a) McEwen, A. B.; Schleyer, P. v. R. *J*. *Org*. *Chem*. **1986**, *51*, 4357−4368. (b) Fokin, A. A.; Jiao, H.; Schleyer, P. v. R. *J*. *Am*. *Chem*. *Soc*. **1998**, *120*, 9364−9365.

15 (a) Toriumi, N.; Muranaka, A.; Kayahara, E.; Yamago, S.; Uchiyama, M. *J*. *Am*. *Chem*. *Soc*. **2015**, *137*, 82−85. (b) Masumoto, Y.; Toriumi, N.; Muranaka, A.; Kayahara, E.; Yamago, S.; Uchiyama, M. *J*. *Phys*. *Chem*. *A* **2018**, *122*, 5162−5167

Chapter 2. 1,3-Diradicals Embedded in Curved Paraphenylene Units: Singlet versus Triplet State and In-Plane Aromaticity

Section 2.1: Introduction to this paper.

The quinoid structure is expected to have high redox activity and photo-responsive properties in the visible and near-infrared region due to the small HOMO-LUMO gap[(1)]. The quinoid structures are constructed by bonding interactions between radicals, but their length is limited (about three benzene rings) due to the loss of aromatic stability of cross-linking units such as benzene (Figure 2.1a). Therefore, we focused on the quinoidal properties induced by the curved structure and expected to construct a quinoidal structure with a longer π-conjugated system than the linear structure. So, the synthesis of macrocyclic azo molecules **AZ-[*n*]CPP** (*n* : number of benzene ring) that are the precursors of diradical **DR-[*n*]CPP** has been initiated (Figure 2.1b).

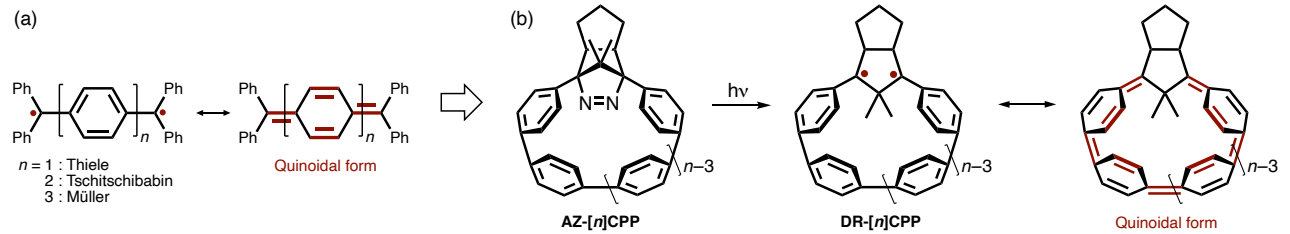

Figure 2.1: (a) The formation of quinoidal structure by bonding interaction. (b) macrocyclic azo and diradical compound.

Section 2.2: Synthesis of macrocyclic azo compound **AZ-6CPP**.

To investigate the behavior of multiradical in the macrocyclic skeleton, the synthesis of a macrocyclic molecule containing azo units was attempted. It is well known that the synthesis of macrocyclic compounds is difficult due to their high strain energy. In addition, the introduction of a thermally unstable azo (**AZ**) unit makes the reaction difficult to adapt to high temperature conditions, requiring the selection of appropriate precursors. As a result of the attempt, the compound **5** was synthesized by adding linear azo molecule **1** which was synthesized by using 4'- bromoacetophenone and methyl 4-bromobenzoate as starting materials in 5 steps[(2a)] to a ketoacetal compound using an organo-lithium reagent, followed by acid hydrolysis[(2b)] and a similar addition reaction. Ni-catalyzed intramolecular cyclization of this precursor followed by reductive aromatization[(2c)] achieved **AZ-6CPP**, with six benzene rings, in a total of 11 steps and an overall yield of 1% (Scheme 2.1).

Scheme 2.1: Synthesis of macrocyclic azo compound **AZ-6CPP**. (a) −78°C: 1 h + 6 h, –78°C → 0°C: 30 min. (b) r.t: 10.5 h. (c) −78°C: 40 min + 4 h 40 min, –78°C → 0°C: 20 min. (d) 0°C → r.t: 11.5 h, 13 % yield (4 steps). (e) 70°C: 50 min + 2.5 h, 91 % yield. (f) −78°C: 2 h, 66 % yield.

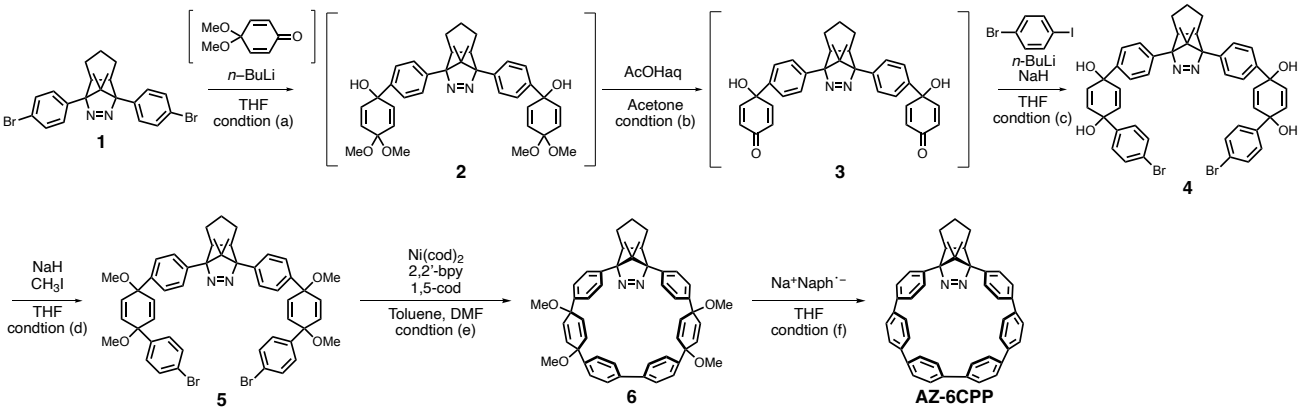

Section 2.3: The character of macrocyclic azo compound **AZ-6CPP**.

In the ^{1}H NMR spectrum (C_6D_6/400 MHz) of **AZ-6CPP**, signals originating from the methyl group of the azo skeleton appear significantly in the high magnetic region (δ −2.36 and −0.49 ppm, Figure 2.2a). The shielding effect of the adjacent benzene ring by constructing a ring structure was reflecting these characteristic signals of methyl groups. Single crystals were successfully prepared by evaporation at room temperature using a solution of chloroform and a few drops of MeOH, and single crystal X-ray structure analysis was conducted. A curved structure was confirmed with an average dihedral angle of 17.2° and a benzene ring curvature angle of 17.7° (Figure 2.2b).

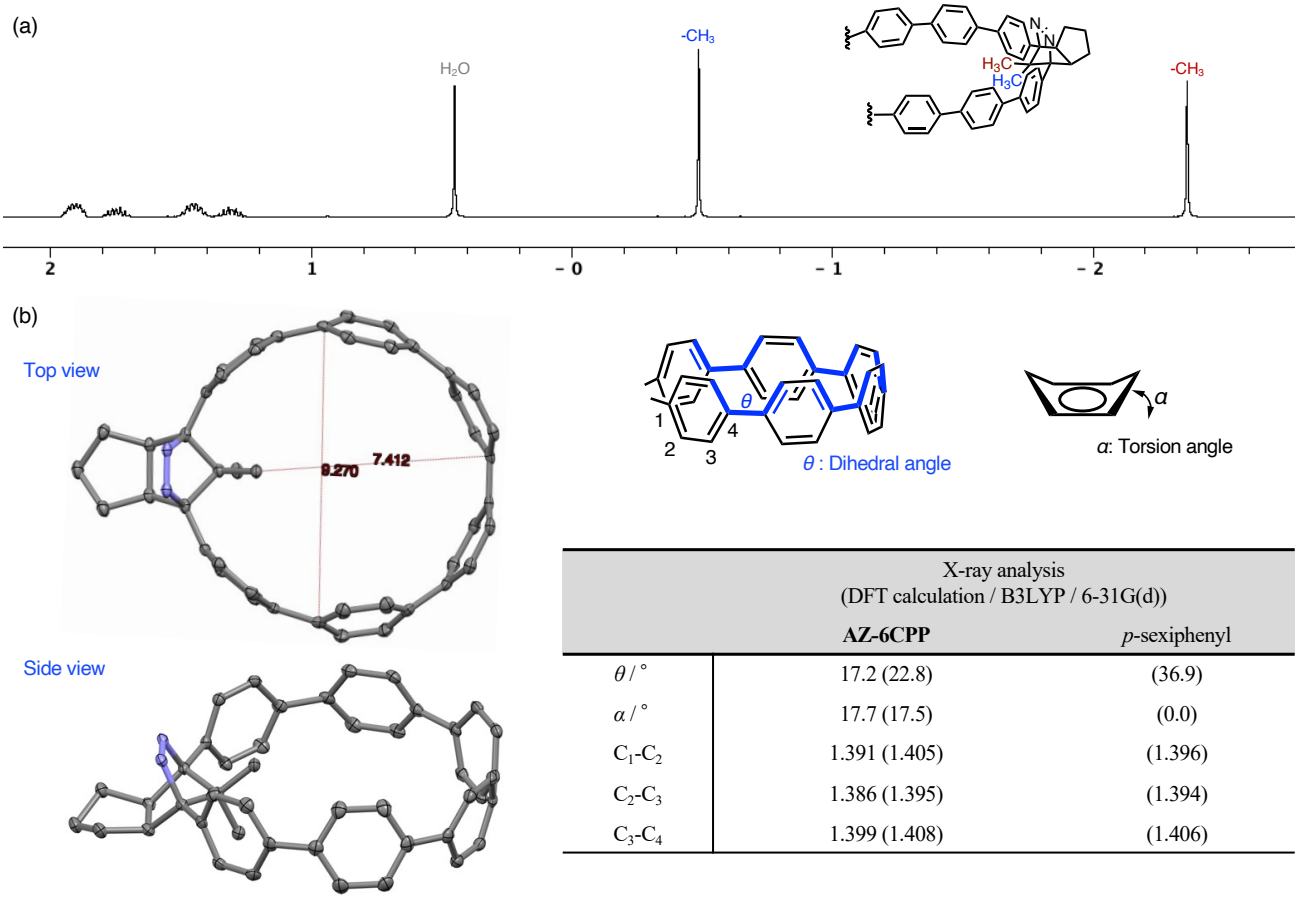

	X-ray analysis (DFT calculation / B3LYP / 6-31G(d))	
	AZ-6CPP	*p*-sexiphenyl
θ / °	17.2 (22.8)	(36.9)
α / °	17.7 (17.5)	(0.0)
C_1-C_2	1.391 (1.405)	(1.396)
C_2-C_3	1.386 (1.395)	(1.394)
C_3-C_4	1.399 (1.408)	(1.406)

Figure 2.2: (a) ^{1}H NMR spectrum of **AZ-6CPP** in C_6D_6 (400 MHz) (b) Single crystal X-ray structure of **AZ-6CPP** with thermal ellipsoids at 50% probability (gray, carbon; blue, nitrogen). Hydrogen atoms and solvent molecules are omitted for clarity.

UV-visible absorption measurements in benzene solution and TD-DFT calculations at the RB3LYP/6-31G(d)[3] level of theory have been conducted. A broad absorption at approximately 400 nm resulting from the HOMO−LUMO transition ($S_0 \rightarrow S_1$) and a structured band at about 330 nm that corresponding to the HOMO−1−LUMO and HOMO−LUMO+2 transitions ($S_0 \rightarrow S_5$) were found (Figure 2.3a,b). The weak absorption of the n-π* transition originating from the -N=N- chromophore, usually seen around 350 nm, could not be confirmed because it overlapped with the strong absorption of the π conjugation system. It has been reported that the HOMO−LUMO transition is forbidden in the case of a small ring CPP such as 6CPP due to its high symmetric structure, but the introduction of the azo skeleton breaks the symmetry of the para-phenylene moiety and allows for the HOMO−LUMO transition. A structured fluorescence emission was observed for 400

nm excitation with peak wavelengths at 475 nm and 505 nm and the S_1 state energy was estimated to be about 66 kcal mol^{-1}(Figure 2.3c). The fluorescence quantum yields and lifetimes were determined to be 79 % and 5.0 ns, 62 % and 4.2 ns under nitrogen and air, respectively. The triplet energy of **AZ-6CPP** was computed to be 55.6 kcal mol^{-1} at the UB3LYP/6-31G(d) level of theory and the energy difference with the S_1 and T_1 state was estimated to 10 kcal mol^{-1}. This energy gap is smaller than that of the singlet oxygen energy ($^1\Delta_g$ = 22.5 kcal mol^{-1}). Therefore, the reason for the lower fluorescence quantum yields in the presence of oxygen was due to the quenching of the S_1 state by spin-orbit coupling with oxygen[4]. The fluorescence quantum yield of [5-8]CPP has been reported to be less than 10 %[5] but **AZ-6CPP** has a high emission property. The embedded azo moiety significantly changed the electronic transition and emission character of the π-conjugated system in this molecule. No phosphorescence was observed even in the 2-MTHF matrix condition at 77 K.

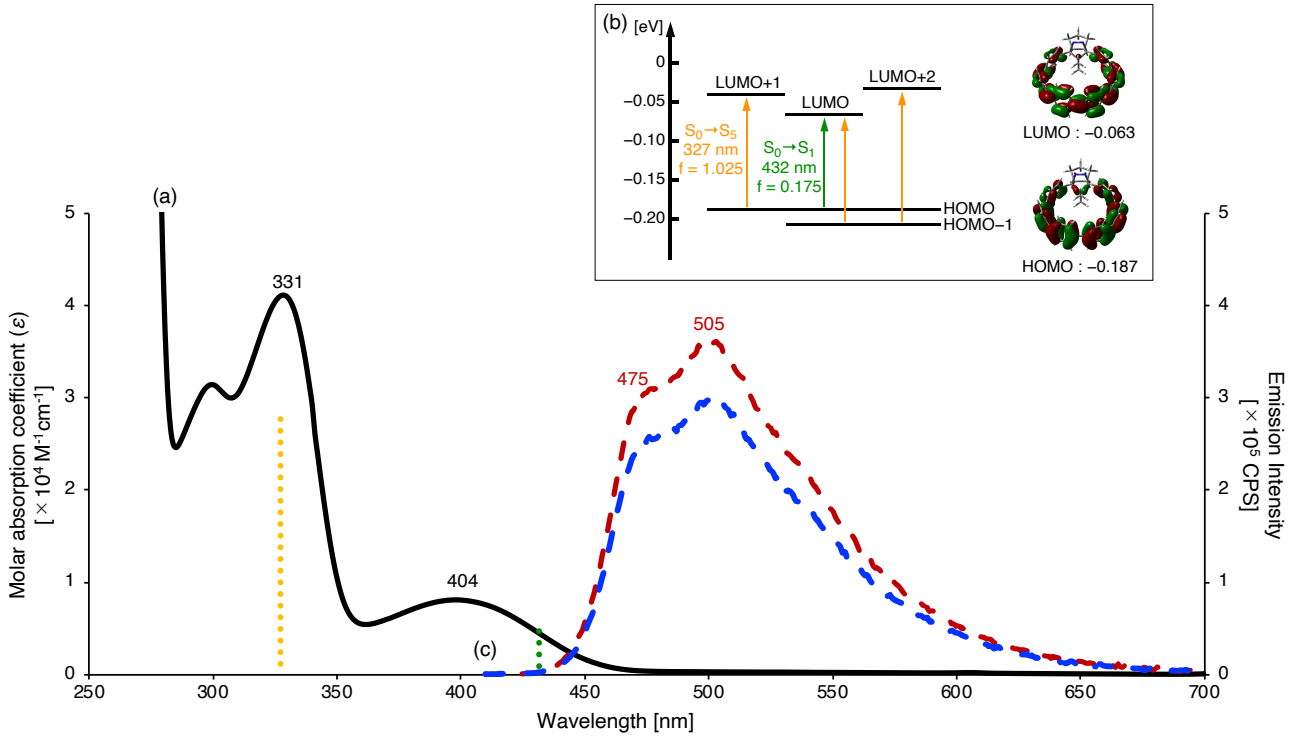

Figure 2.3: (a) UV-vis absorption spectrum and emission spectra of **AZ-6CPP** in benzene solution. (b) Energy diagram of Kohn−Sham orbitals and electronic transitions computed $S_0 \rightarrow S_1$ transition (green: λ_{calc} = 431.7 nm, f = 0.175,) and $S_0 \rightarrow S_5$ transition (yellow: λ_{calc} = 327.1 nm, f = 1.025) at the TD-B3LYP/6-31G(d) level of theory. (c) Emission spectra for 400 nm excitation (Abs_{400} = 0.1) under an N_2 (red) and air (blue) atmosphere in benzene solution.

Section 2.4: Photolysis of azo compound **AZ-6CPP**.

To confirm the photo-denitrogenation of **AZ-6CPP**, the photoreaction of **AZ-6CPP** in degassed C_6D_6 solution (20 mM) was monitored by ^{1}H NMR spectroscopy at 295 K using a 355 nm yttrium aluminum garnet (YAG) laser (approximately 5.5 mJ/pulse). During the irradiation, two new pairs of -CH_3 groups (△; 0.95 and 1.82 ppm, □; 0.58 and 1.52 ppm) derived from two photoreaction products were observed (Figure 2.4). After 45 h of irradiation, the reactant was almost completely consumed. These photoreaction products were found to be decompose gradually under air, but they were quickly isolated by flash chromatography, and analyzed by 2D-NMR and Mass measurements (p-ESI/MeOH sol) under a nitrogen atmosphere, demonstrating that the photoreaction products are the trans-configured ring-closed compound **Trans-CP** and a methyl-group-migrated alkene product **MG**.

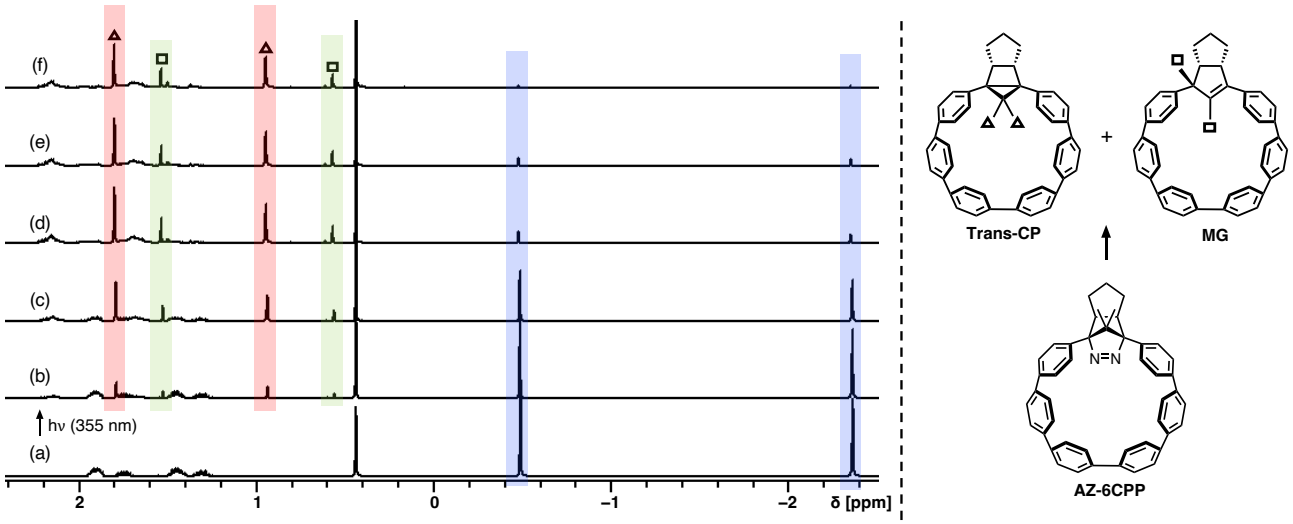

Figure 2.4: ^{1}H NMR analysis (400 MHz) of the photolysis of **AZ-6CPP** (20 mM) by 355 nm laser (5.5 mJ/pulse) in degassed C_6D_6 solution: (a) before irradiation; (b) after 1 h irradiation; (c) after 5.5 h irradiation; (d) after 24 h irradiation; (e) after 35 h irradiation; (f) after 45 h irradiation.

The photo-denitrogenation quantum yield (Φ) of **AZ-6CPP** was determined by comparing the decomposition rate with that of **AZ-2Ph**, whose photo-denitrogenation quantum yield Φ' is known to be 1.0[6]. In the degassed C_6D_6 splution and sealed NMR tube, a 355 nm YAG laser was irradiated, and the photolysis was monitored by ^{1}H NMR spectroscopy. The function $\log([10^{I0} - 1]/[10^{I} - 1])$, where I_0 is the initial concentration of **AZ-6CPP** and **AZ-2Ph** and I is the concentration after photolysis, was calculated from the ^{1}H NMR signal intensity of the CH_3 groups in **AZ-6CPP** and **AZ-2Ph** (Figure 2.5). The photodenitrogenation yield was calculated using the following equation.

$$\text{Slope of } \mathbf{AZ\text{-}6CPP}/\text{Slope of } \mathbf{AZ\text{-}2Ph} = \varepsilon_{\mathbf{AZ\text{-}6CPP}(355)} \times \Phi / \varepsilon_{\mathbf{AZ\text{-}2Ph}(355)} \times \Phi',$$

$$\varepsilon_{\mathbf{AZ\text{-}6CPP}(355)} = 7 \times 10^3 \text{ M}^{-1} \text{ cm}^{-1}$$

$$\varepsilon_{\mathbf{AZ\text{-}2Ph}(355)} = 83 \text{ M}^{-1} \text{ cm}^{-1}$$

From the analysis, the photo-denitrogenation quantum yield of **AZ-6CPP** was determined to be 0.004 (0.4%). The low quantum yield is a result of the 355 nm light being mainly absorbed by the π-conjugated system and no energy transfer from para-phenylene moiety to denitrogenation reaction of azo unit.

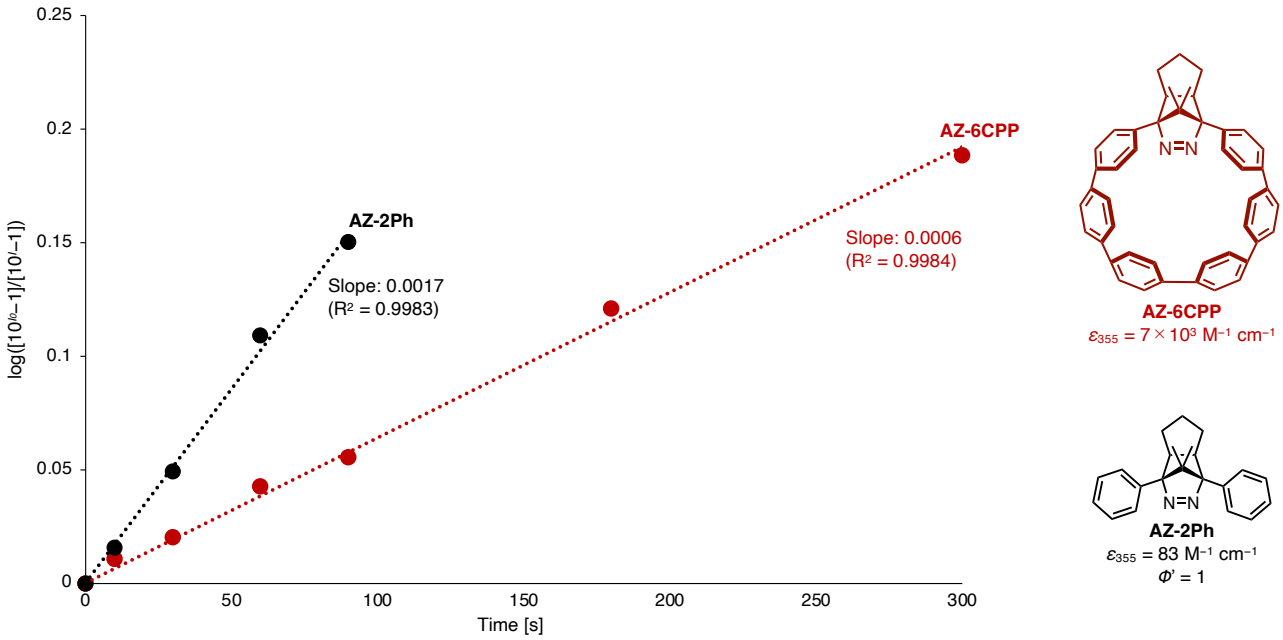

Figure 2.5: Time profiles of the photolysis of **AZ-2Ph** (black) and **AZ-6CPP** (red) as monitored by ^{1}H NMR spectroscopy using a 355 nm laser (5.5 mJ).

Section 2.5: Transient absorption measurement of macrocyclic azo compound **AZ-6CPP**.

Sub-microsecond and sub-nanosecond transient absorption measurement were conducted in benzene solution using laser flash photolysis (LFP) and randomly interleaved pulse train (RIPT) method[7], respectively. Transient species were observed with absorption peaks at approximately 540 and 660 nm in the sub-microsecond TA analysis under N_2 atmosphere (Figure 2.6a). These transient species did not originate from the photo-generated diradical but from the π-conjugated system of para-phenylene moiety, because no change was observed in the UV−vis absorption spectra of the sample before and after the TA measurements (Figure 2.6b). The short-lived species with the lifetime of τ = 5.2 ns were observed in the sub-nanosecond TA spectroscopic analysis at around 600 nm (Figure 2.6c). Also, the lifetime of the slow decay is almost matched with that obtained in the sub-microsecond TA analysis (τ = 6.8 μs). The transient species with the short lifetime of τ = 5.2 ns is assigned to the singlet excited state S_1 of para-phenylene moiety because the lifetime is consistent with that of the fluorescence lifetime. Also, another transient species is assigned to the triplet excited state T_1 because the lifetime was significantly shortened to about 167 ns in the presence of oxygen. The analysis of time profile of the triplet TA spectrum at 540 nm revealed that the fluorescence quenching is due to enhance the intersystem crossing (ISC) from the S_1 to the T_1 state in the presence of $^3O_2$[4] because the absorption originated from triplet excited state under air condition was about 15% higher than that obtained under Ar condition (Figure 2.6d).

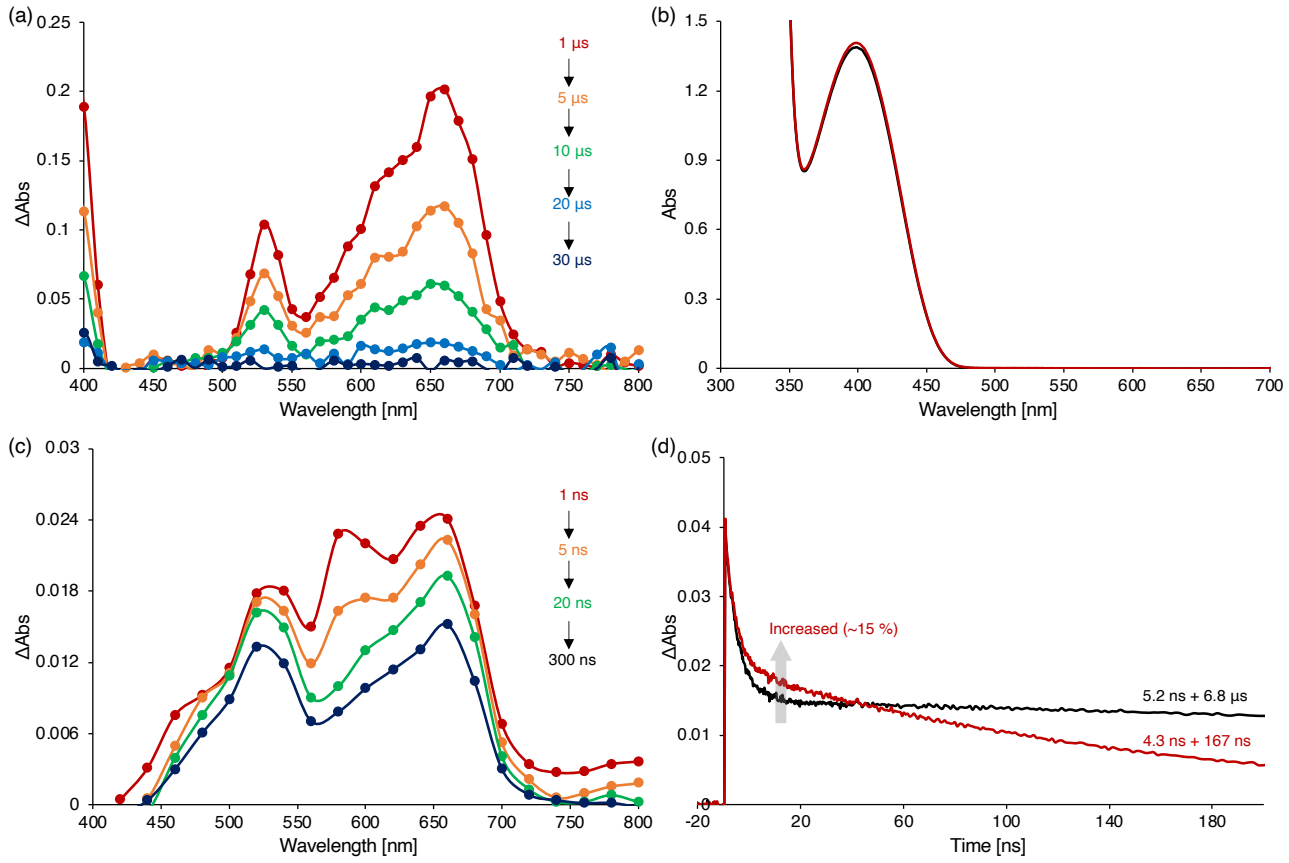

Figure 2.6: (a) Sub-microsecond time-resolved transient absorption spectra in benzene under N_2 atmosphere at 295 K. (b) UV-vis absorption spectra of the sample in benzene before (black) and after (red) measurement of sub-microsecond LFP. (c) Sub-nanosecond time-resolved transient absorption spectra in benzene under an Ar atmosphere at 295 K. (d) Time profile at 540 nm in the sub-nanosecond time-resolved spectroscopic analysis under Ar (black) and air (red) conditions.

Section 2.6: EPR measurement of **DR-6CPP**.

The quantum yield of the photo-denitrogenation of **AZ-6CPP** is quite low, but it could observe directly photo-generated diradical **DR-6CPP** using an electron paramagnetic resonance (EPR) spectroscopic analysis. Low-temperature photolysis of **AZ-6CPP** was conducted using a high-pressure Hg lamp at 4 K in degassed 2-MTHF matrix condition (11 mM). After photolysis for 4 h, a characteristic triplet signal was detected at 1650 G (half-field region) which was assigned to the forbidden transition (ΔMs = ± 2). In addition, signals originating from the allowed transitions with ΔMs = ± 1 [2977 (z_1), 3142 (xy_1), 3560(xy_2), and 3731 G (z_2)] were also observed at a resonance frequency of 9.40 GHz (Figure 2.7a). From the z_1 and z_2 signals, the zero-field splitting (zfs) parameters were determined to be $|D/hc|$ = 0.035 cm^{-1} and $|E/hc| \leq 0.001$ cm^{-1}[8], which are smaller than that of the diradical **DR-2Ph** generated by photolysis of **AZ-2Ph** ($|D/hc|$ = 0.050 cm^{-1} and $|E/hc| \leq 0$ .001 cm^{-1})[9]. The average distance between diradical was estimated to be 4.20 Å in **DR-6CPP** and 3.76 Å in **DR-2Ph** from *D* value[8], indicating that the diradical is more delocalized over the benzene rings. The spin densities of triplet diradicals **T-DR-2Ph** and **T-DR-6CPP** were computed at the UB3LYP/6-31G(d) level of theory to obtain more information about the spin distribution. The spin density at the benzylic carbon was calculated to be 0.753 for **T-DR-2Ph**, 0.706 for **T-DR$_{exo}$-6CPP**, and 0.665 for **T-DR$_{endo}$-6CPP**, respectively. To confirm the structural assignment of the triplet diradical detected by photolysis of **AZ-6CPP**, the zfs parameters $|D/hc|$ and $|E/hc|$ were computed at the (RO)BP/EPR-II//UB3LYP/6-31G(d) level of theory using ORCA 4.2.1[10]. The $|D/hc|$ and $|E/hc|$ value were computed to be 0.041 cm^{-1} and 0.002 cm^{-1} for **T-DR$_{exo}$-6CPP** and 0.034 cm^{-1} and 0.005 cm^{-1} for **T-DR$_{endo}$-6CPP**, respectively (Figure 2.7b). Therefore, **T-DR$_{endo}$-6CPP** was observed in the photolysis of **AZ-6CPP**. **AZ-6CPP** has the same configuration of endo conformer and this might be the reason why the endo configuration was detected at EPR measurement.

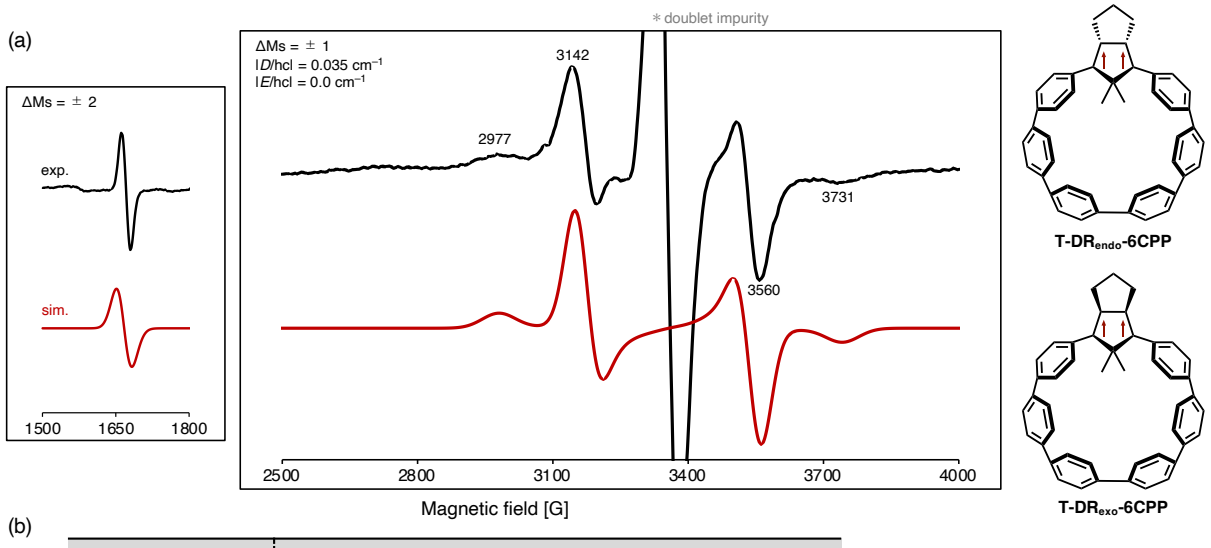

(b)

	$\|D/hc\|/\|E/hc\|$ [cm^{-1}]		
	T-DR-2Ph	**T-DR$_{exo}$-6CPP**	**T-DR$_{endo}$-6CPP**
Experimental	0.050/<0.001	-	0.035/<0.001
Computed at ROBP/EPR-II	0.050/0.002	0.041/0.002	0.034/0.005

Figure 2.7: (a) EPR spectrum of the photolysis of **AZ-6CPP** (11 mM) using a Hg lamp (>250 nm) in 2-MTHF matrix condition at 4 K (resonance frequency 9.40 GHz) and simulated EPR spectrum using the zfs parameters $|D/hc|$ = 0.035 cm^{-1} and $|E/hc|$ = 0 cm^{-1}. (b) Experimental and computed zfs parameters ($|D/hc|$ and $|E/hc|$) for triplet diradicals **T-DR-2Ph** and **T-DR-6CPP** at the (RO)BP/EPR-II//UB3LYP/6-31G(d) level of theory.

The temperature dependence of the signal intensity of the triplet diradical at around 1650 G was monitored to determine the ground spin state. At first, the dependence of the signal intensity to a microwave power was investigated at 4 K and the maximum power of the measurement is determined to 20 mW, for which saturation of the EPR signal was not observed. After the generation of **DR-6CPP** at 4 K, the temperature T was gradually increased and monitored the signal intensity I at around 1650 G (Figure 2.8a). The triplet signal suddenly weakened at 40 K and the signal intensity did not return to the original intensity at 4 K, suggested that **DR-6CPP** have the high reactivity, which different from the behavior of **T-DR-2Ph**[11]. In the signal intensity I × temperature T vs Temperature T (IT-T) plot using the value below 30 K, the IT value gradually increased with increasing temperature, indicating that the triplet state is thermally populated as an excited state. From the least-squares fit for the Bleaney−Bowers analysis[8, 12] using the values from 4 K to 30 K, singlet and triplet energy gap ΔE_{S-T} was determined to be −15.8 ± 0.5 cal mol^{-1}, demonstrating the singlet ground state of **DR$_{endo}$-6CPP**. Therefore, the ground spin state was switched by the ring structure (Figure 2.8b).

Bleaney−Bowers equation $I \times T = C[3\exp\left(\frac{2J}{RT}\right)]/[1 + 3\exp\left(\frac{2J}{RT}\right)]$

C : constant, R : gas constant (8.314 [J K^{-1} mol^{-1}]), J : exchange interaction

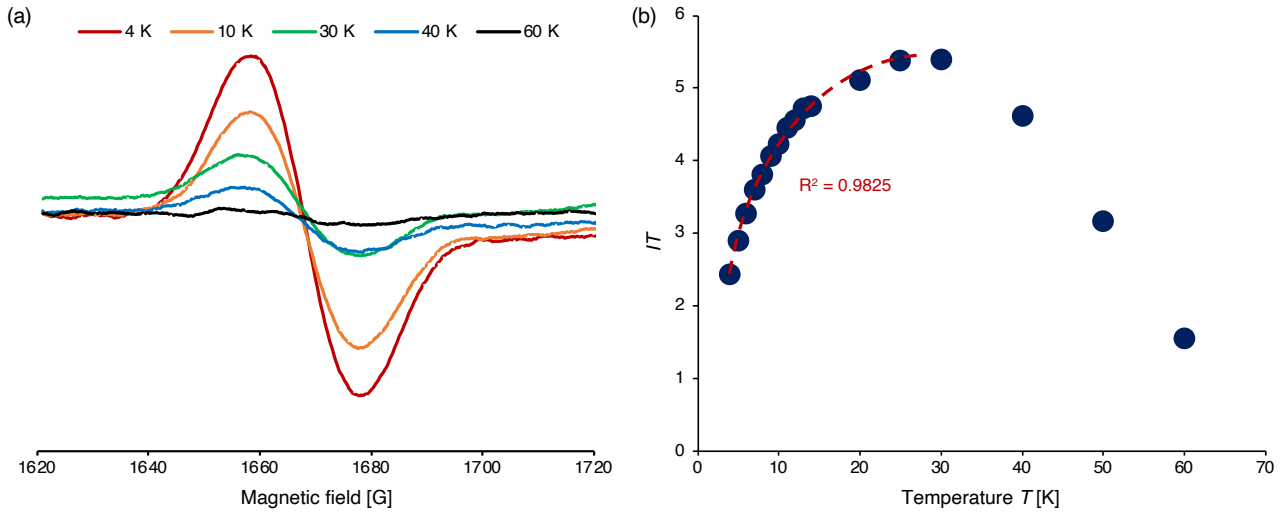

Figure 2.8: (a) Temperature dependence of the signal intensity at the half-field region. (d) Signal intensity I × Temperature T vs Temperature T (IT-T) plot and least-squares fit for the Bleaney−Bowers analysis.

Section 2.7: Theoretical calculation.

To gain more insight into the macrocyclic effect, singlet and triplet energy gap ΔE_{S-T} of **DR-2Ph**, **DR$_{endo}$-6CPP**, and **DR-2Ph′** were computed using DFT/UCAM-B3LYP/6-31G(d)[13] level of theory and complete active space self-consistent field (CASSCF) calculations[14a]. The structure of **DR-2Ph′** was obtained by replacing the middle four benzene rings with two hydrogen atoms in **DR$_{endo}$-6CPP** because the π-electrons in **DR-6CPP** are too large to allow computation of multiconfigurational method. The energy corrections were conducted using the complete active space second-order perturbation theory (CASPT2)[14b] for the CASSCF calculations. Triplet ground state was found for **DR-2Ph**, while singlet ground state was found for **DR$_{endo}$-6CPP** and **DR-2Ph′** at all method, suggesting that the ground spin state was switched by the ring structure (Figure 2.9a). To understand the electronic structures, the HOMO and LUMO occupation numbers of singlet diradical **S-DR-2Ph** and **S-DR$_{endo}$-6CPP** were determined at the CASSCF(2,2)/6-31G(d) level of theory. A parallel alignment of the p orbitals[15] was found in **S-DR-2Ph** and the occupation numbers of electrons in the HOMO (Ψ_A) and LUMO (Ψ_S) orbitals were computed to be 1.04 and 0.96, respectively, indicating a negligible bonding interaction between the two radical site and favor to take triplet ground state due to the electrons are occupied each orbit separately. (Figure 2.9b). In contrast, bonding interaction between the two radical site was found in the bending structure in **S-DR$_{endo}$-6CPP** and the energy level of Ψ_S was stabilized. The orbital of Ψ_A and Ψ_S were switched and the occupation numbers of electrons in the HOMO (Ψ_S) and LUMO (Ψ_A) orbitals were changed to be 1.47 and 0.53, respectively. As a results, the electrons are occupied in the Ψ_S orbitals, the ground spin state was changed to singlet by the ring structure.

(a)

Compound	Singlet−triplet energy gap ΔE_{S-T} [kcal mol^{-1}]		
	UCAM-b3LYP /6-31G(d)	CASSCF(14,14) /cc-pVDZ	CASPT2(14,14) /cc-pVDZ
DR-2Ph	+0.20	+0.37	+0.20
DR$_{endo}$-6CPP	−1.77	-	-
DR-2Ph'	−1.20	−3.84	−6.35

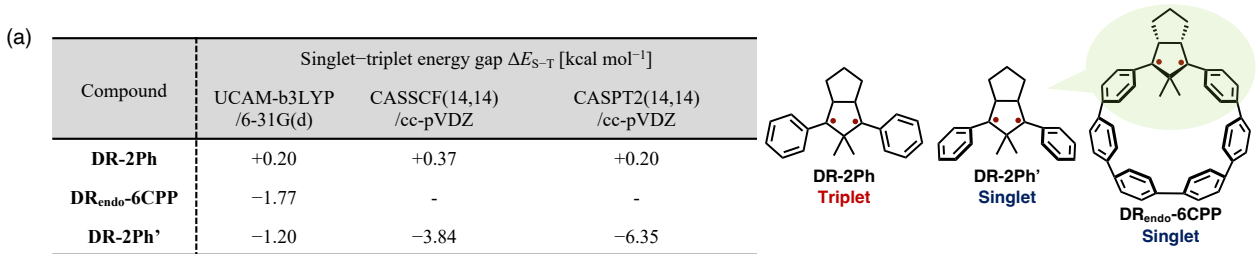

(b)

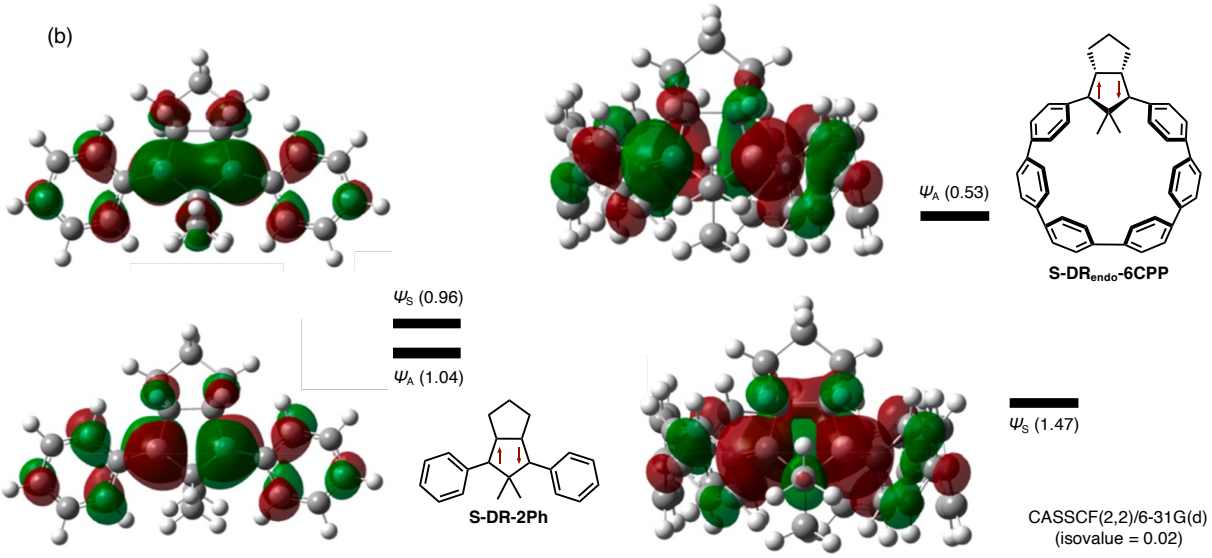

Figure 2.9: (a) Calculated singlet−triplet energy gap ΔE_{S-T}. (b) HOMO and LUMO orbitals in **S-DR-2Ph** and **S-DR$_{endo}$-6CPP** calculated at the CASSCF(2,2)/6-31G(d) level of theory.

To obtain more insights into the macrocyclic effect on the reactivity of the diradicals, the activation barriers for the photoreaction products **Trans-CP** and **MG** were computed at the BS-UCAM-B3LYP/6-31G(d) level of theory. A small energy barrier (1.87 kcal mol^{-1}) was calculated for the ring-closing reaction giving a cis-configured compound **Cis-CP** in the exo-isomer of **S-DR$_{exo}$-6CPP** (Figure 2.10a). A clear energy barrier was not found for the kinetically favored trans-configured compound **Trans-CP** in the reaction of endo-isomer **S-DR$_{endo}$-6CPP**, suggesting that the energy barrier from **S-DR$_{endo}$-6CPP** to **Trans-CP** should be very small. The observed high reactivity of **DR$_{endo}$-6CPP** in low-temperature EPR measurement is reasonable due to this very small activation energy. A relatively large energy barrier (41.9 kcal mol^{-1}) was computed for the thermodynamically favored methyl migration compound **MG**, suggesting that the formation of **MG** stems from an electronically excited state[11]. In the linear singlet diradical **S-DR-2Ph**, the activation barrier to **Trans-CP** was computed to 13.7 kcal mol^{-1} (Figure 2.10b), confirming the disappearance of the activation barrier by making the ring structure. To investigate this reason, the molecular strain energies were computed by isodesmic reaction using the CAM-B3LYP/6-31G(d) level of theory[16]. The strain energies of **AZ-6CPP** and **DR$_{exo,\ endo}$-6CPP** were determined to be about 79−85 kcal mol^{-1} (Figure 2.10c). In contrast, the strain energies of the ring-closed product **CP** were lower to be about 12−14 kcal mol^{-1} than those of the diradical intermediates, demonstrating that the ring-closing reaction releases molecular strain. Therefore, the very small energy barriers in the ring-closing process were accelerated by the release of molecular strain energy, as well as the bonding interaction in **S-DR-6CPP**.

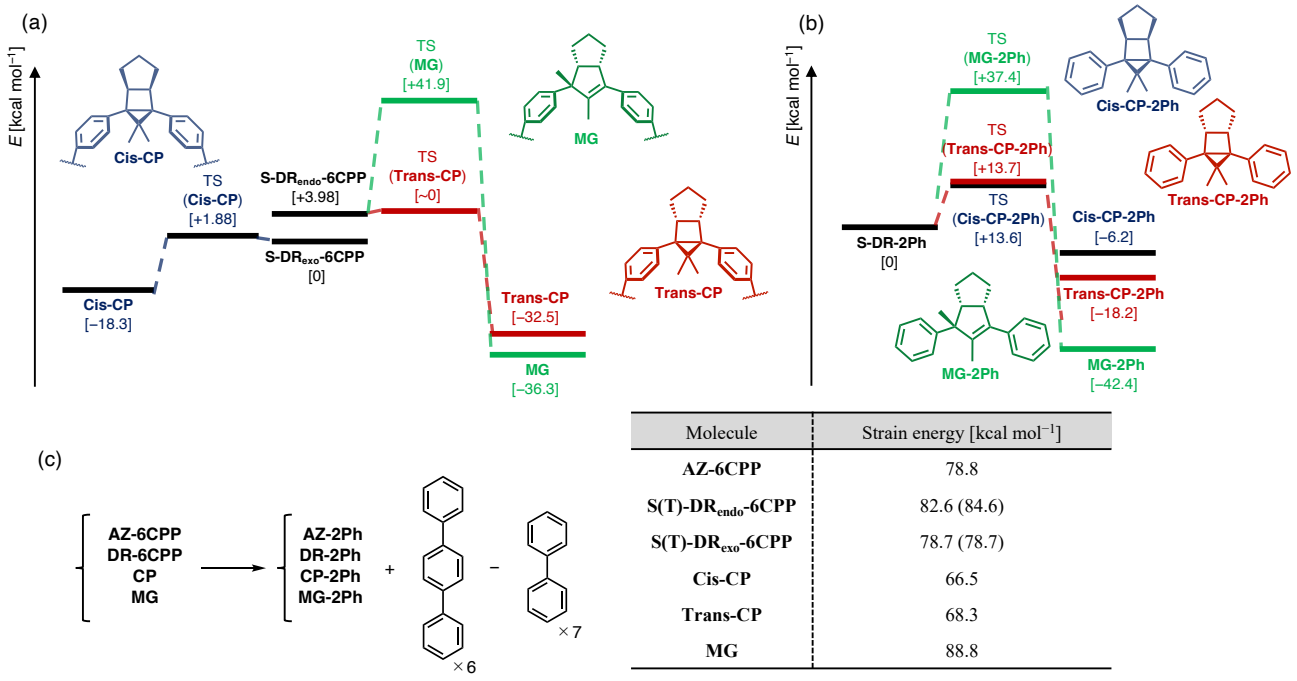

Molecule	Strain energy [kcal mol^{-1}]
AZ-6CPP	78.8
S(T)-DR$_{endo}$-6CPP	82.6 (84.6)
S(T)-DR$_{exo}$-6CPP	78.7 (78.7)
Cis-CP	66.5
Trans-CP	68.3
MG	88.8

Figure 2.10: Computations on the thermal reactivity of (a) singlet diradical **S-DR-2Ph** and (b) singlet diradical **S-DR-6CPP** at the (U)CAM-B3LYP/6-31G(d) level of theory. (c) isodesmic reaction of molecular strain energies.

The ring size effect on the singlet−triplet energy gap ΔE_{S-T} of **DR$_{endo}$-[*n*]CPP** and occupation numbers in HOMO and LUMO were computed at the (U)CAM-B3LYP/6-31G(d) and CASSCF(2,2) level of theory (Figure 2.11a). ΔE_{S-T} was found to be significantly dependent on the ring size. As the ring size increases, there is a trend for the occupation number

of LUMO increase, which affecting in diradical character, and have triplet ground state similar to **DR-2Ph**. In contrast, as the ring size decreases, the occupation number of LUMO decrease and take singlet ground state. Surprisingly, ΔE_{S-T} drastically increased for the case of **DR$_{endo}$-4CPP** and **DR$_{endo}$-3CPP**. These singlet states are regarded as closed-shell molecules with quinoidal form rather than perfect open-shell molecules because the occupation number in HOMO is very high[17]. So, in addition to the bonding interaction between the two radical site by the bending structure, contribution of the quintal form was influenced to the singlet−triplet energy gap ΔE_{S-T}. Also, the nucleus-independent chemical shift values NICS(0)zz at the center position of the ring were computed to examine the in-plane aromaticity[18]. As the ring size decreases, the NICS values become negative due to increase in the contribution of the quinoidal form. The NICS value of **S-DR$_{endo}$-4CPP** was highly negative, indicating that there is the in-plane aromaticity generated by the quinoidal form and the homoconjugation[19] of two radical sites. Also, the in-plane aromaticity of **S-DR$_{endo}$-4CPP** was visualized using 2D-NICS(0)zz plot (Figure 2.11b) and anisotropy of the induced current density (ACID) plot (Figure 2.11c)[20]. The smaller NICS(0)zz value of **DR$_{endo}$-3CPP** than that of **S-DR$_{endo}$-4CPP** was found because of the large bond alternation of the quinoidal structures of, which is reflected by the low degree of π-conjugation.

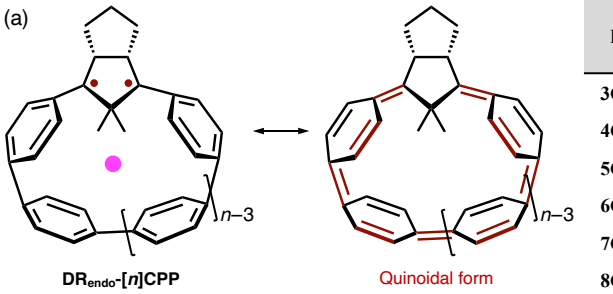

DR	Occupation number		ΔE_{S-T} [kcal mol^{-1}]	Strain energy [kcal mol^{-1}]	NICS(0)$_{zz}$ [ppm] Singlet (Triplet)
	HOMO	LUMO			
3CPP	1.91	0.09	−21.29	101.0	−3.6 (+11.9)
4CPP	1.64	0.36	−4.50	103.0	−19.2 (+10.4)
5CPP	1.54	0.46	−1.90	92.3	−2.9 (+5.2)
6CPP	1.47	0.53	−1.77	82.6	+0.1 (+3.6)
7CPP	1.16	0.84	+0.13	78.2	+2.4 (+2.9)
8CPP	1.12	0.88	+0.19	70.9	+2.1 (+2.3)

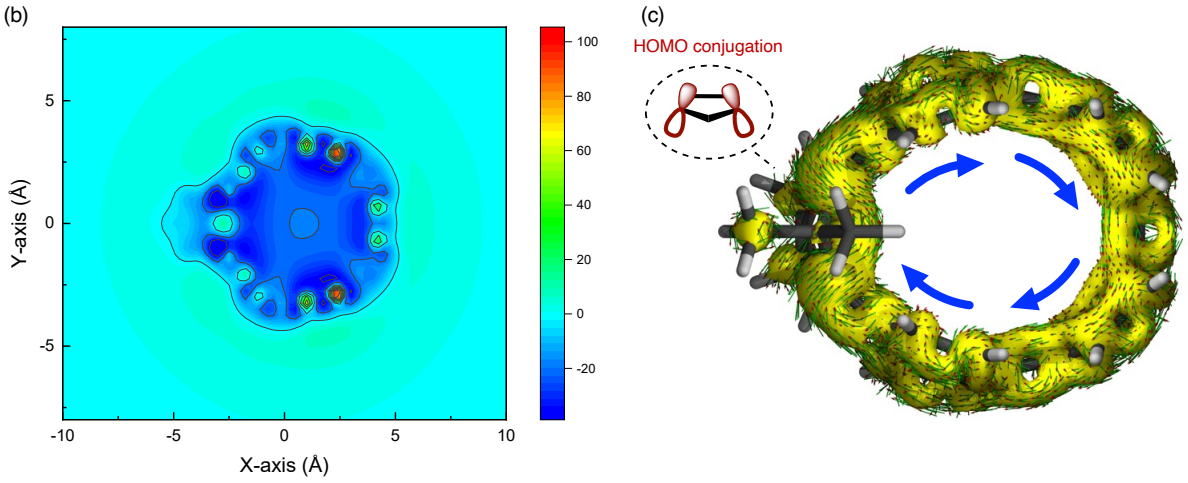

Figure 2.11: (a) Effect of the ring size on the ΔE_{S-T} in **DR$_{endo}$-[*n*]CPP** (*n* = 3−8). Occupation numbers in the HOMO and LUMO were determined at the CASSCF(2,2)//BS-UCAM-B3LYP/6-31G(d) level of theory. NICS(0)$_{zz}$ values at the ring centers were computed at the UB3LYP/6-31+G(d) level of theory (pink: dummy atom). (b) 2D-NICS(0)$_{zz}$ plot of **S-DR$_{endo}$-4CPP** computed at the UB3LYP/6-31+G(d) level of theory. (c) Top view of the ACID plot of the ring current in **S-DR$_{endo}$-4CPP**.

Section 2.8: Summary of this chapter.

In this chapter, focusing on the behavior of diradical embedded in the CPP structure and synthesize the precursor **AZ-6CPP**. In contrast to the smaller ring-size CPP such as 6CPP, **AZ-6CPP** exhibits higher fluorescence properties because of the introduction of the azo skeleton breaks the symmetry of the para-phenylene moiety and allows for the HOMO−LUMO transition. Also, lower photo-denitrogenation yields than linear azoalkane **AZ-2Ph** was revealed. The photo-generated diradical **DR$_{endo}$-6CPP** was directly detected using EPR spectroscopic analysis under low-temperature matrix conditions. A singlet ground state was found by various temperature EPR experiment and revealed the diradical is more delocalized by the curved structure. Also, high reactivity than **DR-2Ph** was found. Quantum chemical calculations revealed that the ground spin state is controlled by the ring size. As the ring size decreases, the unique in-plane aromaticity generated by the quinoidal form and the homoconjugation was revealed.

Section 2.9: Experimental section.

Section 2.9.1: General Information.

Reagents and solvents

All commercially available reagents were purchased from TCI, Wako, Oakwood Chemical and BLD Pharmatech and were used without further purification. Dry toluene for synthesis was obtained by distillation over CaH_2. Dry-DMF was purchased from Wako. 2-methyl tetrahydrofuran for EPR measurement was obtained by distillation over CaH_2 and Na. Dry solvents for spectroscopy analysis were purchased from commercial suppliers.

Procedure

All workup and purification procedures were performed with reagent-grade solvents in the air. Thin-layer chromatography (TLC) analyses were performed using commercial aluminum sheets of Merck silica gel 60 F_{254} and visualized with an ultraviolet lamp (λ = 254 nm). Column chromatography was performed with silica gel 60N (spherical, neutral, 63-210 μm, Kanto). Recycling chromatographic separation in GPC were performed by LC-9210, Japan Analytical Industry Co., Ltd. with chloroform as mobile phase.

Measurements

NMR spectra were recorded on a Bruker Ascend 400 (^{1}H NMR : 400 MHz, ^{13}C NMR : 100 MHz) spectrometer and referenced to residual solvent peak. Coupling constants (*J*) are denoted in Hz and chemical shifts (δ) in ppm. The abbreviations s, d, t, dd, dt, td and m stand for the resonance multiplicities singlet, doublet, triplet, doublet of doublets, doublet of triplets, triplet of doublets and multiplet, respectively. IR spectrum was recorded on a JASCO MCT-6000M. The date of High-resolution Mass spectrometry (HRMS) was measured with Thermo Fisher Scientific LTQ Orbitrap XL using electrospray ionization (ESI) or atmospheric-pressure chemical ionization (APCI) method. The X-ray diffraction data of the single crystals were collected on a Bruker APEX-II Ultra CCD diffractometer. The structures were solved using direct methods and refined by full-matrix least-squares techniques using the SHELX program package. Single crystal X-ray structure was visualized by Mercury (CCDC). UV-vis spectra were recorded on a SHIMADZU UV-3600 Plus spectrometer. The spectra were collected at room temperature using a slit width of 1 nm with middle scan rate. Steady-state fluorescence spectra were recorded with a FluoroMax 4 spectroflurometer Horiba Yobin Yvon using a slit width of 1 nm. Fluorescence lifetime was measured by using FluoroHub-B, TemPro 01, TBX, and 373 nm NanoLED light (HORIBA). The excitation source for sub-microsecond laser flash photolysis (LFP) was a tunable Nd:YAG minilite laser at 355 nm. The monitoring system consisted of a 150 W Xenon arc lamp as light source, a Unisoku MD200 monochromator detection and a photomultiplier. Sub-nanosecond transient absorption measurements were conducted with Unisoku PicoTAS system in 2 mm cuvette. The excitation source was a passive Q-SWITCH microchip laser at 355 nm. Cw-EPR spectra were recorded on Bruker BioSpin ELEXSYS E500 spectrometer.

Section 2.9.2: Synthesis and spectral data.

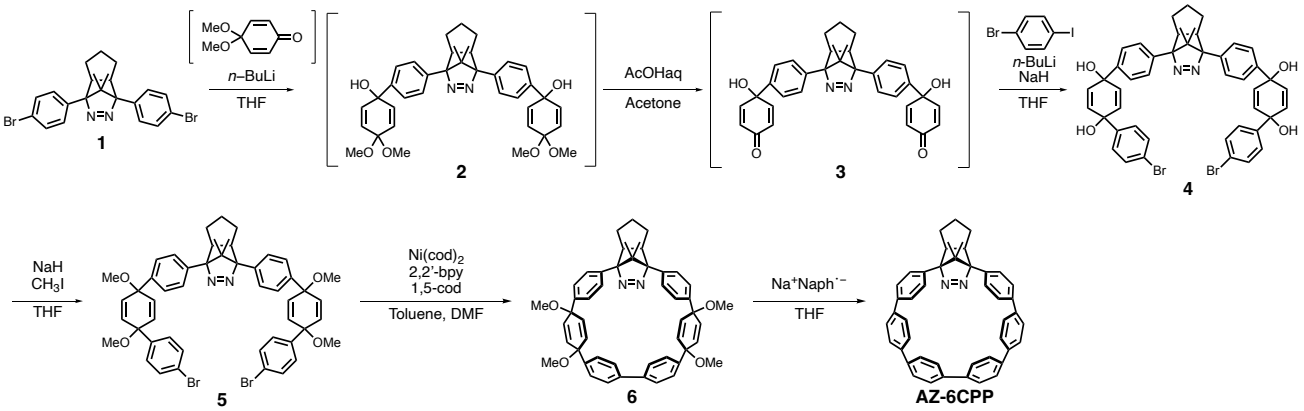

Synthesis of compound **2**.

Under nitrogen atmosphere, 4-methoxyphenol (3.16 g, 25.5 mmol) was dissolved in degassed-methanol (250 mL) and cooled to 0°C. Iodobenzene diacetate (8.21 g, 25.5 mmol) was added, and nitrogen replacement was conducted again. Afterwards, the mixture was stirred at 0°C to room temperature for 13 h (overnight). The reaction was quenched by the addition of $NaHCO_3$aq. The organic layer was extracted with CH_2Cl_2 two times, washed with brine, dried over $MgSO_4$. After filtration, the solvent was removed under reduced pressure to give mono-ketal compound, which was used in the next step without further purification.

Under nitrogen atmosphere, **1** (2.38 g, 5.02 mmol) was dissolved in dry-THF (80 mL) and cooled to –78°C. A cyclohexane solution of *n*-BuLi (2.3 M, 8.5 mL, 20 mmol) was added to the solution at –78°C and the mixture was stirred at same temperature for 1 h. The crude product of mono-ketal compound was added dropwise, and the resulting mixture was stirred at –78°C for 6 h and at –78°C to 0°C for 30 min. The reaction was quenched by the addition of $Na_2S_2O_3$aq. The organic layer was extracted with EtOAc two times, washed with brine, dried over $MgSO_4$. After filtration, the solvent was removed under reduced pressure to give the crude including **2**, which was used in the next step without further purification. **HRMS** (p-ESI, MeOH sol) m/z: Calcd for $C_{38}H_{44}O_6N_2Na$ $[M + Na]^+$, 647.30916, found 647.30927.

Synthesis of compound **3**.

Under nitrogen atmosphere, the crude product of **2** was dissolved in degassed acetone (280 mL). The mixture of H_2O (130 mL) and AcOH (15 mL) was added and stirred at room temperature for 10.5 h (overnight). The reaction was quenched by the addition of $NaHCO_3$aq. The organic layer was extracted with EtOAc two times, washed with brine and dried over $MgSO_4$. After filtration, the solvent was removed under reduced pressure to give the crude including **3**, which was used in the next step without further purification. **HRMS** (p-ESI, MeOH sol) m/z: Calcd for $C_{34}H_{33}O_4N_2$ $[M + H]^+$, 533.24348, found 533.24310.

Synthesis of compound **4**.

Under nitrogen atmosphere, 1-bromo-4-iodobenzene (17.2 g, 60.9 mmol) was dissolved in dry-THF (200 mL) and cooled to –78°C. A cyclohexane solution of *n*-BuLi (2.3 M, 27.5 mL, 63 mmol) was added to the solution at –78°C and the mixture was stirred at same temperature for 1 h.

On the other hand, a solution of crude product of **3** in dry-THF (70 mL) was added to a solution of 60% sodium hydride

(0.99 g, 24.8 mmol) in dry-THF (45 mL) under nitrogen atmosphere at –78°C and stirred for 40 min at same temperature. The mixture containing 1-bromophenyllithium was slowly added to another solution of crude of **3** for 40 min by transfer tube. The reaction mixture was stirred at –78°C for 4 h and at –78°C to 0°C for 20 min. The reaction was quenched by the addition of $Na_2S_2O_3$aq. The organic layer was extracted with EtOAc two times, washed with brine, dried over Na_2SO_4. After filtration, the solvent was removed under reduced pressure. The crude mixture was quickly purified by silica gel column chromatography to give **4** (634 mg), which is used for next reaction immediately.

HRMS (p-ESI, MeOH sol) m/z: Calcd for $C_{46}H_{43}O_4N_2Br_2$ $[M + H]^+$, 845.15841, found 845.15826.

Synthesis of compound **5**.

Under nitrogen atmosphere, a solution of **4** (634 mg) in dry-THF (7 mL) was added to a solution of 60% sodium hydride (167 mg, 4.2 mmol) in dry-THF (4 mL) at 0°C and stirred for 45 min at same temperature. The mixture was charged with CH_3I (0.40 mL, 6.5 mmol) and stirred at 0°C to room temperature for 11.5 h (overnight). The reaction was quenched by the addition of $Na_2S_2O_3$aq. The organic layer was extracted with EtOAc two times, washed with brine, dried over Na_2SO_4. After filtration, the solvent was removed under reduced pressure. The crude mixture was purified by silica gel column chromatography to give **5** (597 mg, 0.66 mmol) in 13 % yield of 4 steps. **^{1}H NMR** ($CDCl_3$, 400 MHz) δ 0.12 (s, 3H), 0.92 (s, 3H), 1.39-1.55 (m, overlap with water), 3.44-3.46 (s, 12H), 3.49 (m, 2H), 6.08-6.20 (d, J = 10.2 Hz and J = 10.3 Hz, 8H), 7.29-7.31 (d, J = 8.68 Hz, 4H), 7.43-7.49 (d, J = 8.68 and J = 8.52 Hz, 8H), 7.67-7.69 (d, J = 8.52 Hz, 4H). **^{13}C NMR** ($CDCl_3$, 100 MHz) δ 17.16, 17.94, 25.67, 28.75, 49.00, 52.18, 52.23, 66.50, 74.70, 74.82, 98.38, 121.76, 126.05, 127.77, 128.00, 131.61, 133.19, 133.29, 133.87, 133.96, 135.82, 142.73, 142.74. **HRMS** (p-ESI, MeOH sol) m/z: Calcd for $C_{50}H_{51}O_4N_2Br_2$ $[M + H]^+$, 901.22101, found 901.22131.

Synthesis of compound **6**.

Under nitrogen atmosphere, 1,5-cyclooctadiene (0.22 mL, 1.8 mmol) and 2,2'-bipyridyl (279 mg, 1.8 mmol) were dissolved in dry-toluene (7 mL) and dry-DMF (7 mL). The reaction flask was replaced with argon atmosphere after freeze pump thaw cycling (four times). $Ni(cod)_2$ (513 mg, 1.9 mmol) was added, and replacement of argon atmosphere was conduct again. The mixture was stirred at 70°C for 30 min.

On the other hand, under nitrogen atmosphere, **5** (406 mg, 0.45 mmol) was dissolved in dry-toluene (26 mL). The reaction flask was replaced with argon atmosphere after freeze pump thaw cycling (four times). The solution of **5** was added to the Ni-catalyst solution for 50 min at 70°C. The mixture was stirred for 2.5 h, then cooled down to room temperature. The reaction mixture was added to 1 M HClaq and stirred for 1 h at room temperature. The organic layer was extracted with EtOAc two times, washed with brine, dried over Na_2SO_4. After filtration, the solvent was removed under reduced pressure. The crude mixture was purified by silica gel column chromatography to give **6** (308 mg, 0.41 mmol) in 91 % yield. **^{1}H NMR** ($CDCl_3$, 400 MHz) δ –1.18 (s, 3H), 0.35 (s, 3H), 1.46–1.51 (m, 1H), 1.59–1.69 (m, 5H), 3.36–3.41 (s, 12H), 3.46–3.47 (m, 2H), 6.17–6.20 (dd, J = 10.3 Hz, J = 2.48 Hz, 2H), 6.37–6.40 (dd, J = 10.3 Hz, J = 2.48 Hz, 2H), 6.60–6.63 (dd, J = 10.3 Hz, J = 2.44 Hz, 2H), 6.70–6.73 (dd, J = 10.4 Hz, J = 2.48 Hz, 2H), 7.02–7.08 (m, J = 8.76 Hz, 8H), 7.44 (s, 8H). **^{13}C NMR** ($CDCl_3$, 100 MHz) δ 17.34, 17.48, 25.42, 29.18, 47.68, 52.09, 52.37, 66.44, 74.07, 75.26, 97.87, 126.25, 126.88, 133.10, 133.34, 134.42, 134.58, 135.37, 138.58, 141.49, 142.37. **HRMS** (p-ESI, MeOH sol) m/z: Calcd for $C_{50}H_{51}O_4N_2$ $[M + H]^+$, 743.38433, found 743.38446.

Synthesis of compound **AZ-6CPP**.

Under nitrogen atmosphere, naphthalene (1.02 g, 7.96 mmol) was added to a solution of sodium (0.33 g, 14.4 mmol) in dry-THF (12 mL) at 0℃ and replacement of nitrogen atmosphere was conducted again. The mixture was stirred at 0℃ to room temperature for 7.5 h.

On the other hand, **6** (211 mg, 0.28 mmol) was dissolved in dry-THF (50 mL) under nitrogen atmosphere and cooled to –78℃. The solution of sodium naphthalenide (12 mL) was added to the solution of 6 and stirred for 2 h at same temperature. The solution of I_2 in THF (I_2 : 2.56 g, 10.1 mmol / THF : 10 mL) was added to the reaction mixture and the reaction was quenched by the addition of $Na_2S_2O_3$aq. After warming to room temperature, the organic layer was extracted with CH_2Cl_2 two times, washed with brine, dried over Na_2SO_4. After filtration, the solvent was removed under reduced pressure. The crude mixture was purified by silica gel column chromatography and preparative gel permeation chromatography using chloroform as the eluent to give **AZ-6CPP** (115 mg, 0.19 mmol) as green solid in 66 % yield. **^{1}H NMR** (C_6D_6, 400 MHz) δ –2.36 (s, 3H), –0.49 (s, 3H), 1.27–1.35 (m, 1H), 1.40–1.49 (m, 2H), 1.71–1.79 (m, 1H), 1.87–1.94 (m, 2H), 2.93–2.99 (m, 2H), 6.86–6.89 (dd J = 8.52 Hz, J = 2.00 Hz, 2H), 7.14–7.52 (m, 20H), 8.02–8.05 (dd J = 8.56 Hz, J = 2.00 Hz, 2H). **^{13}C NMR** (C_6D_6, 100 MHz) δ 17.00, 17.82, 25.45, 29.71, 47.61, 70.14, 97.25, 124.29, 125.50, 130.09, 136.42, 137.03, 137.10, 137.17, 137.91, 138.83. **HRMS** (p-ESI, MeOH sol) m/z: Calcd for $C_{46}H_{39}N_2$ $[M + H]^+$, 619.31078, found 619.31061. **IR** (KBr plate [cm^{-1}]) 725, 820, 1242, 1258, 1373, 1387, 1477, 1579, 2858, 2873, 2950, 3023, 3067, 3086.

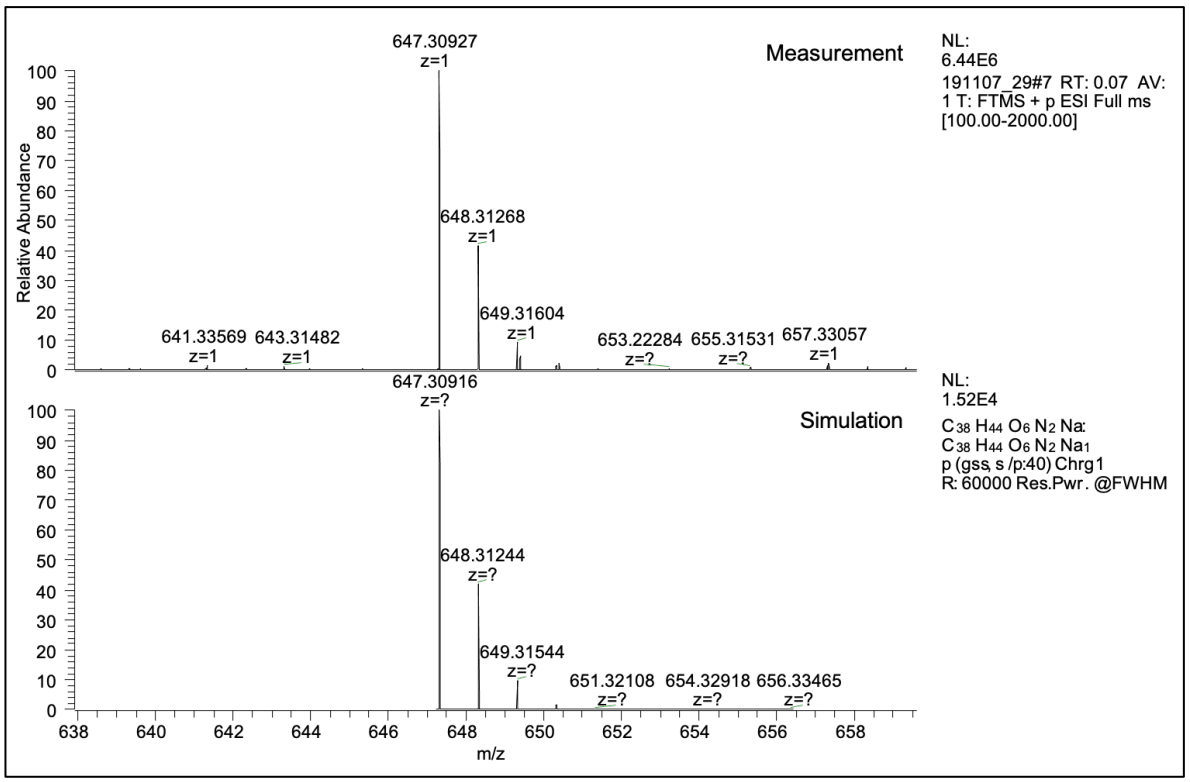

Figure S2.1: Mass spectrum and simulation of compound **2**.

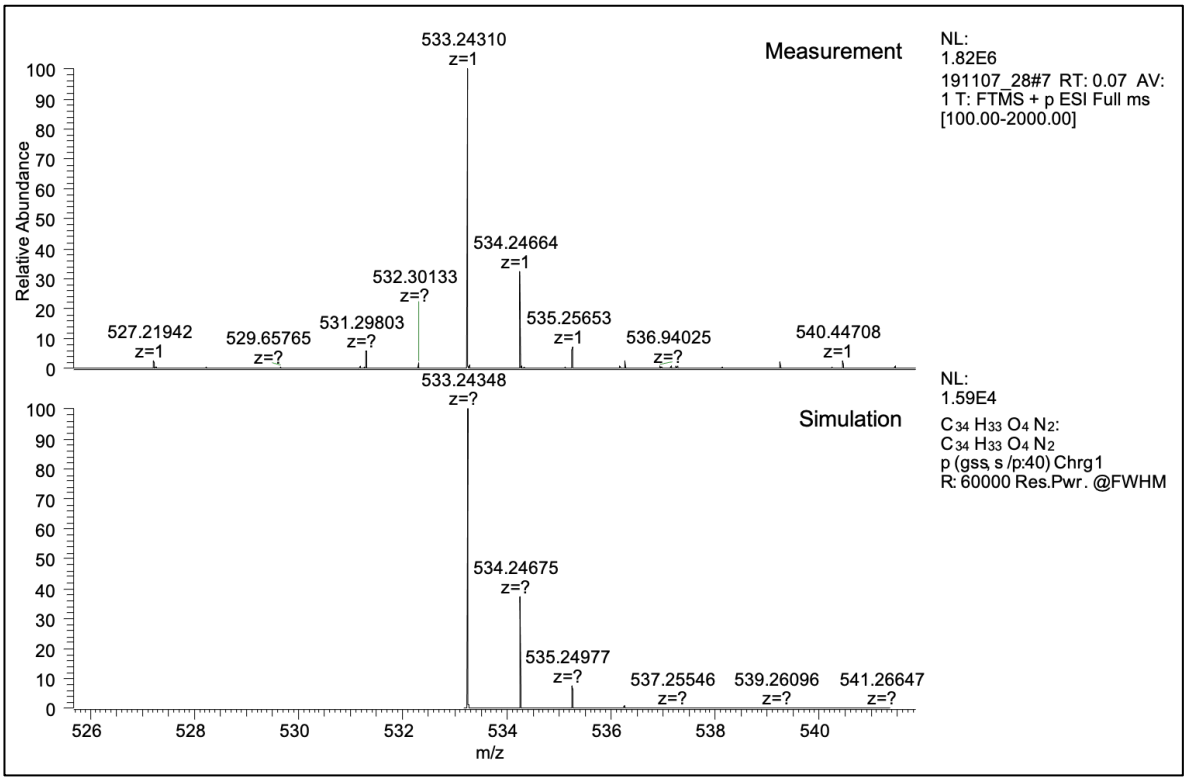

Figure S2.2: Mass spectrum and simulation of compound **3**.

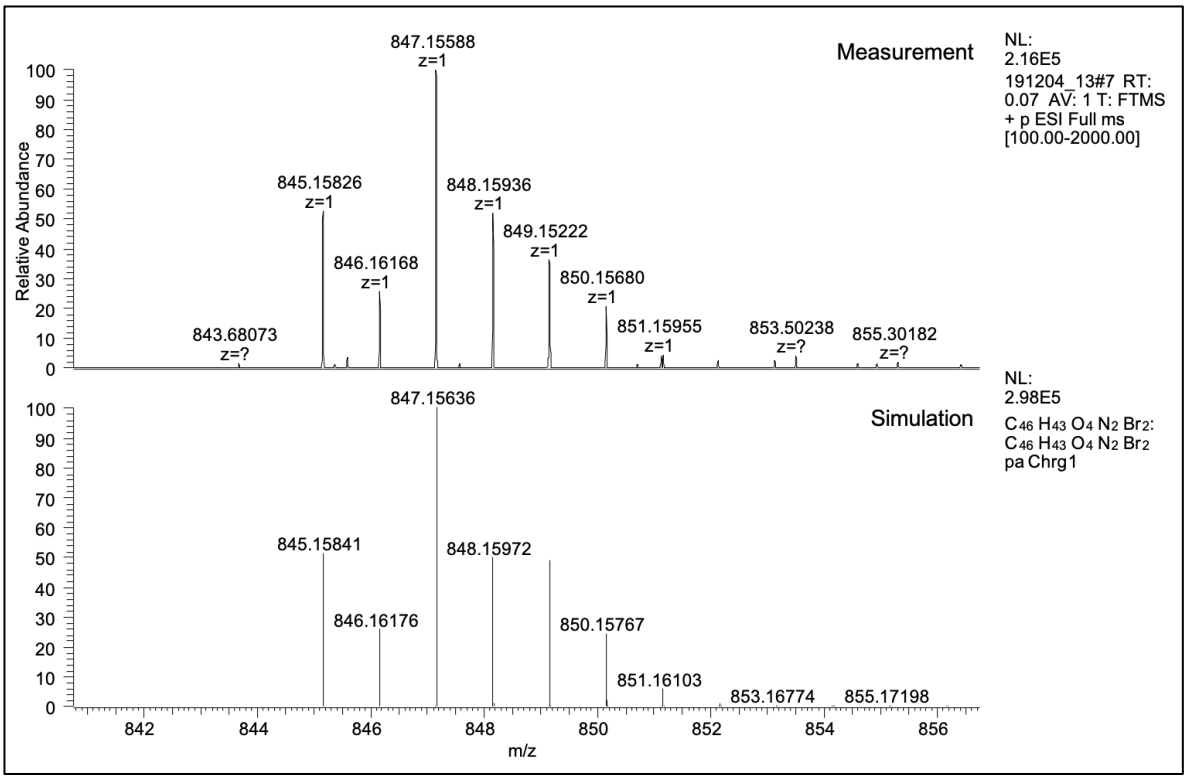

Figure S2.3: Mass spectrum and simulation of compound **4**.

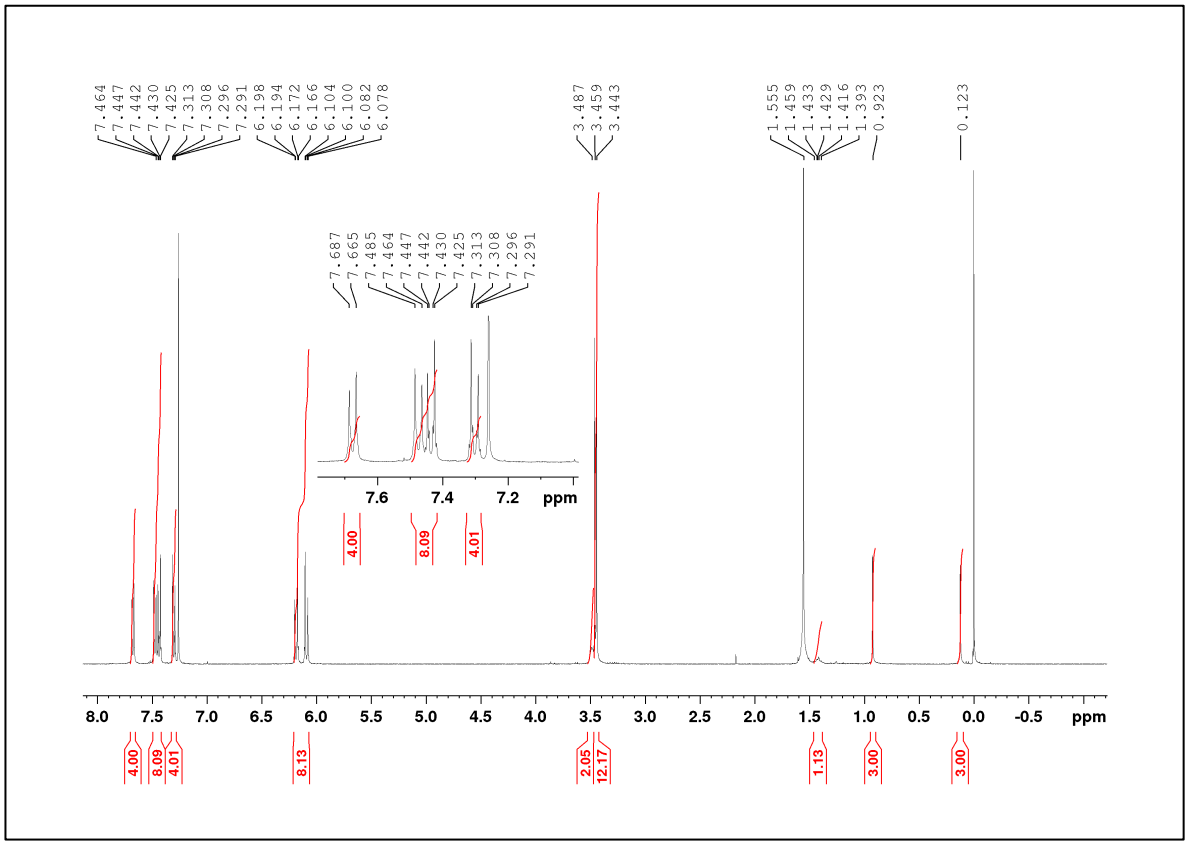

Figure S2.4: ^{1}H NMR spectrum of compound **5**.

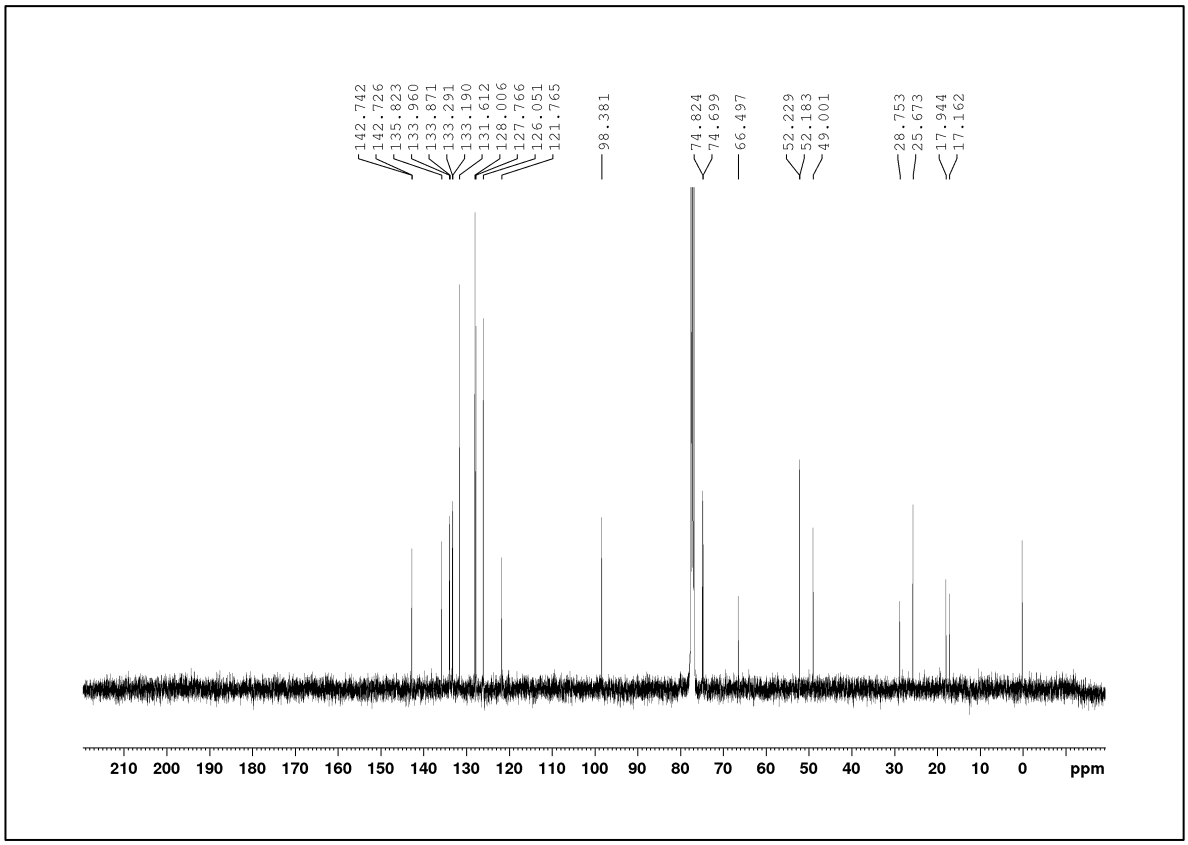

Figure S2.5: ^{13}C NMR spectrum of compound **5**.

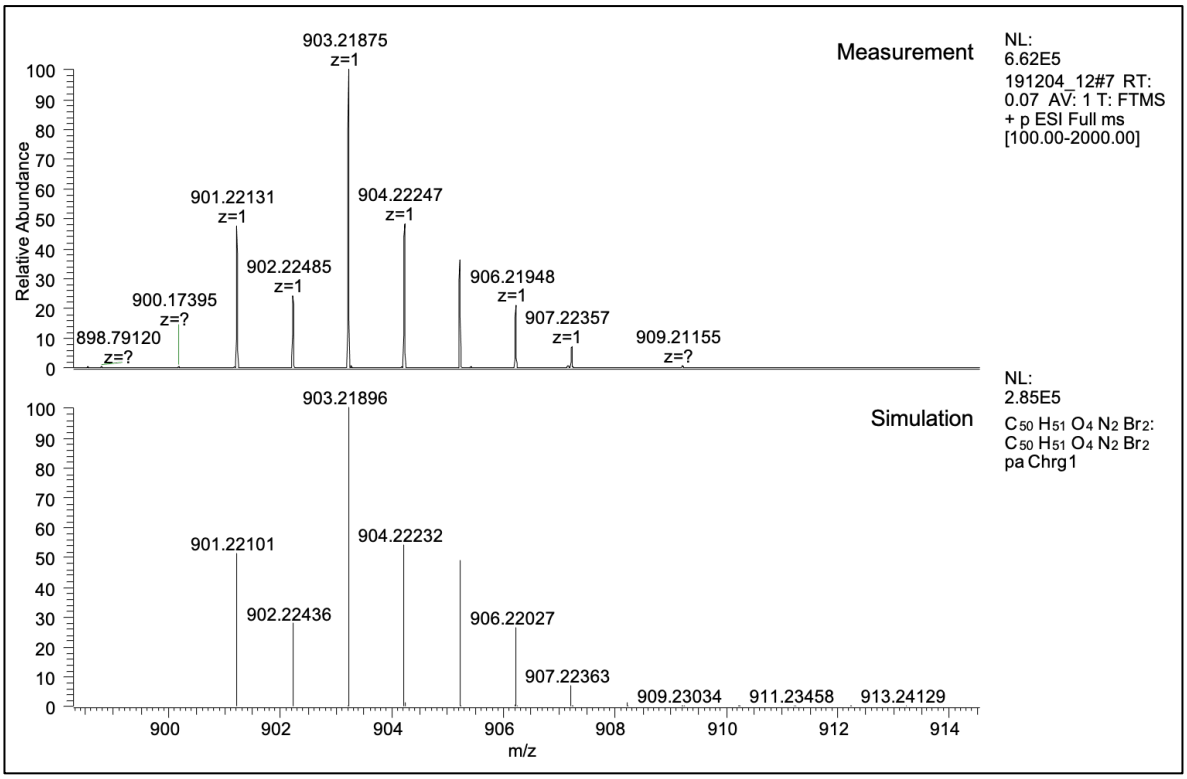

Figure S2.6: Mass spectrum and simulation of compound **5**.

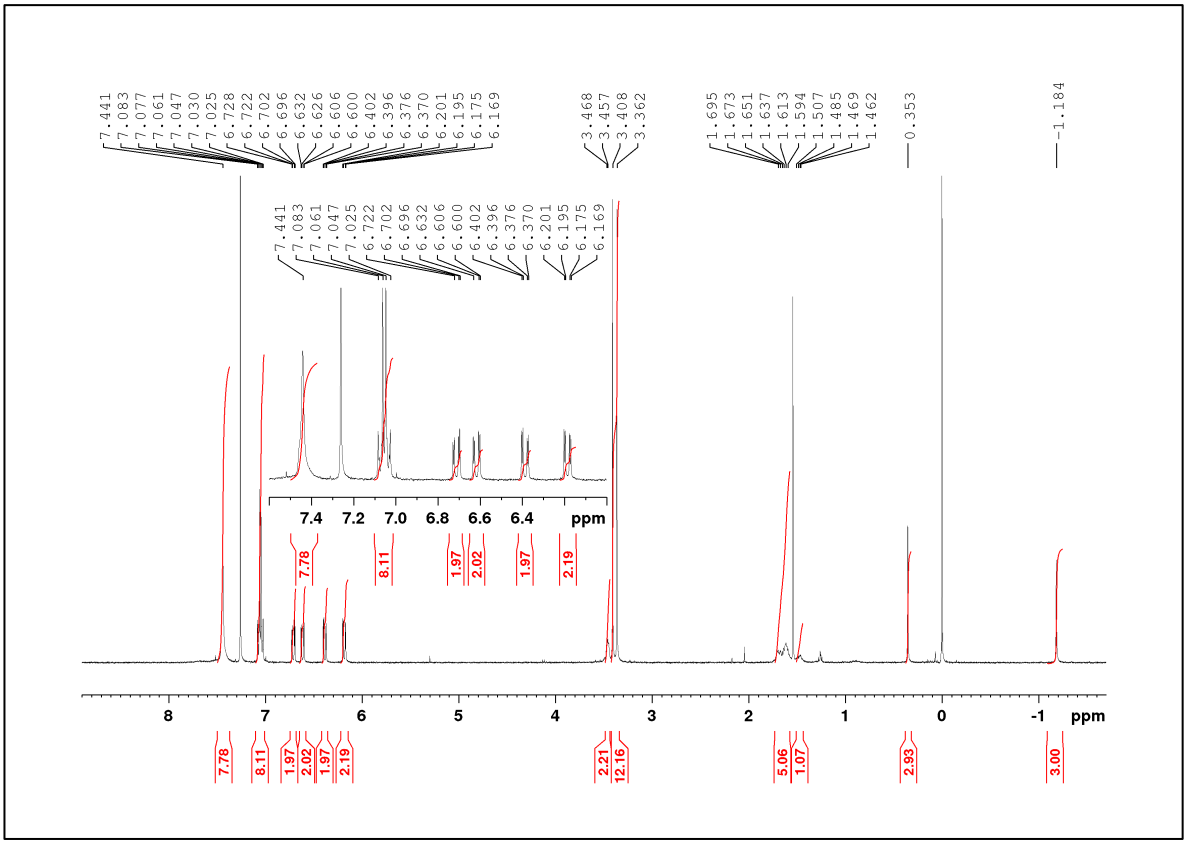

Figure S2.7: ^{1}H NMR spectrum of compound **6**.

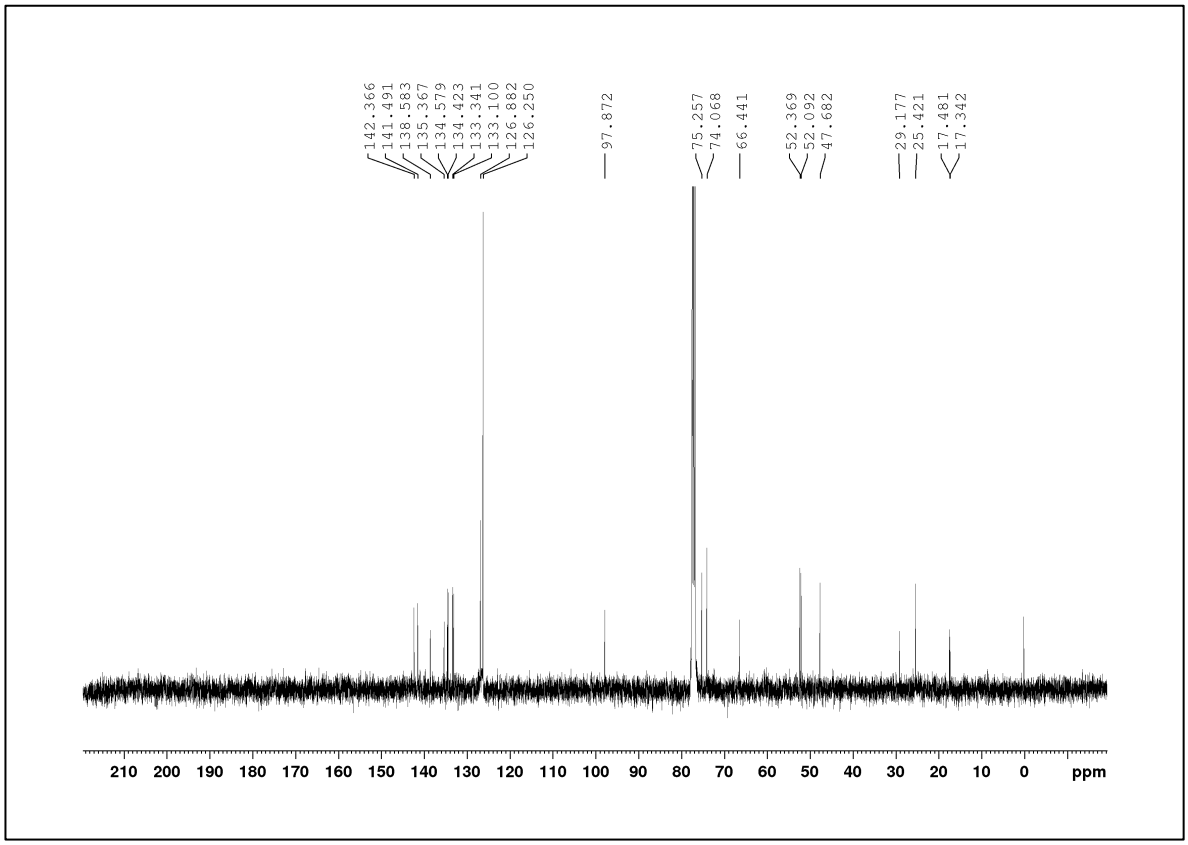

Figure S2.8: ^{13}C NMR spectrum of compound **6**.

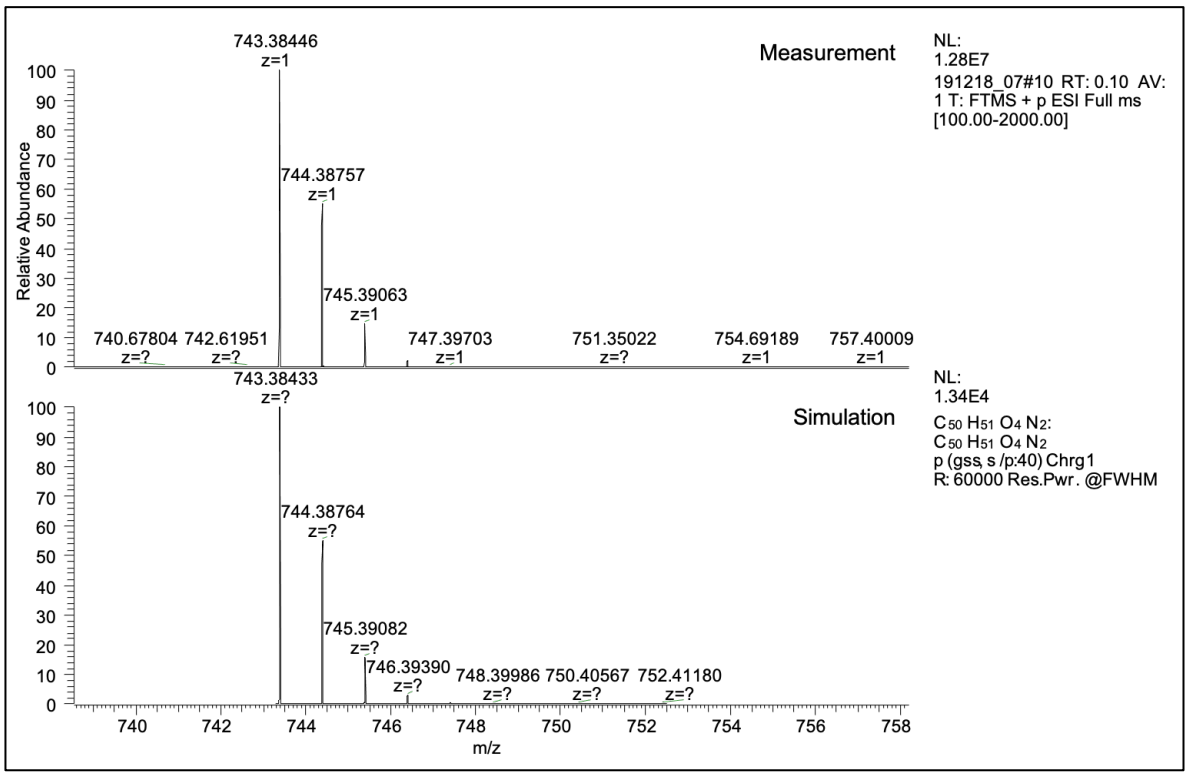

Figure S2.9: Mass spectrum and simulation of compound **6**.

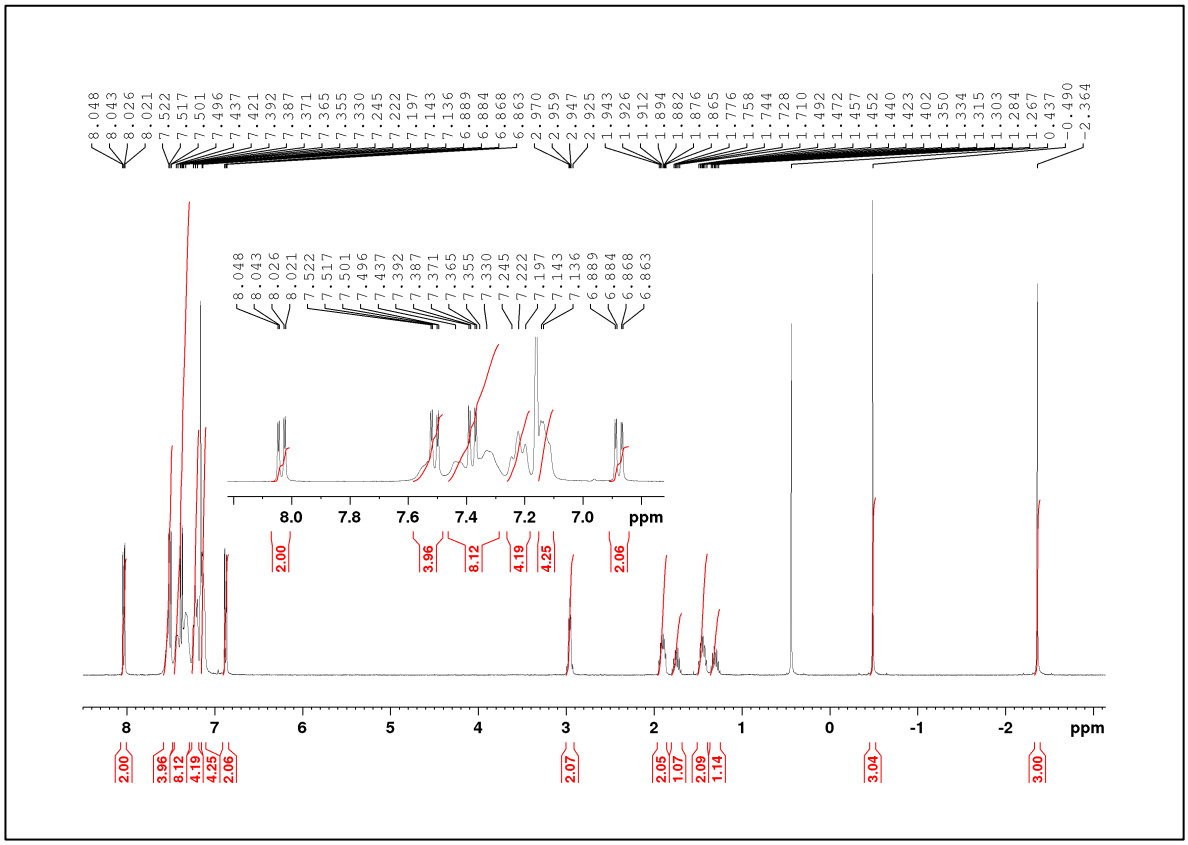

Figure S2.10: ^{1}H NMR spectrum of **AZ-6CPP**.

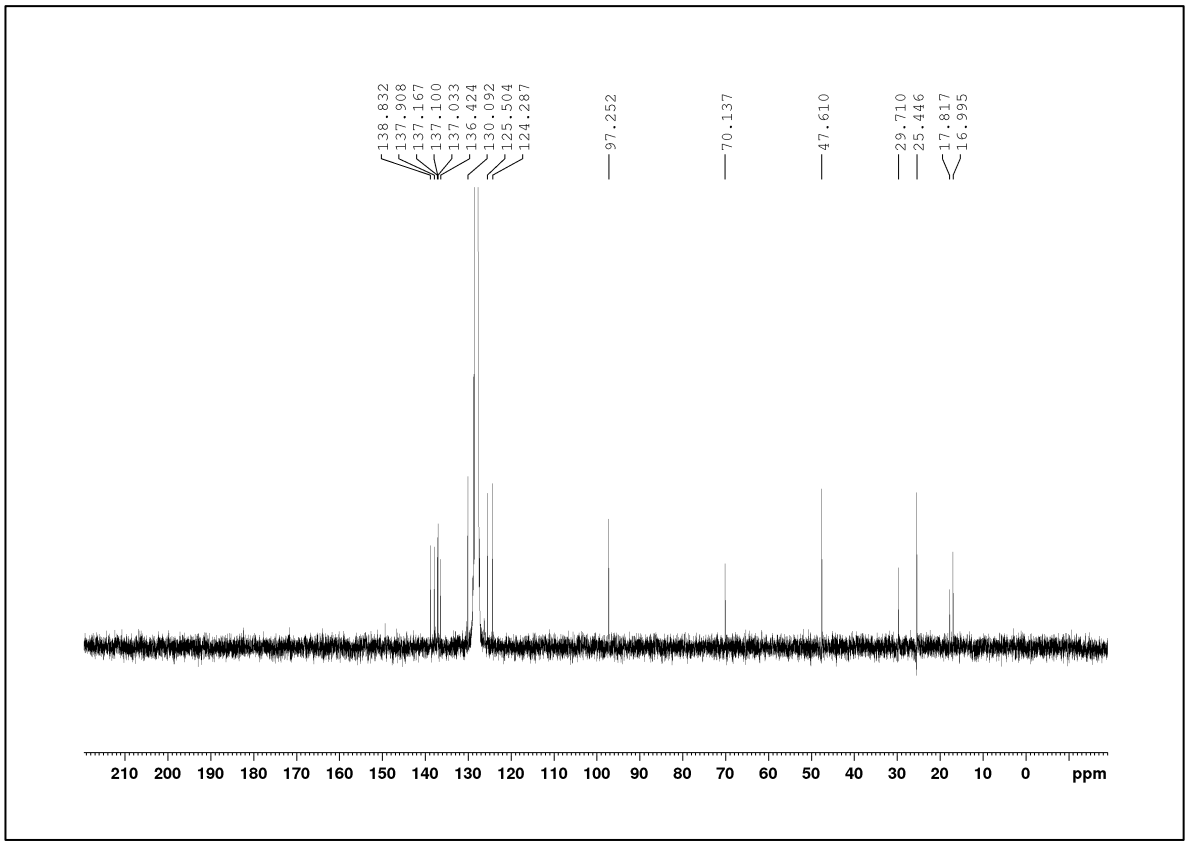

Figure S2.11: ^{13}C NMR spectrum of **AZ-6CPP**.

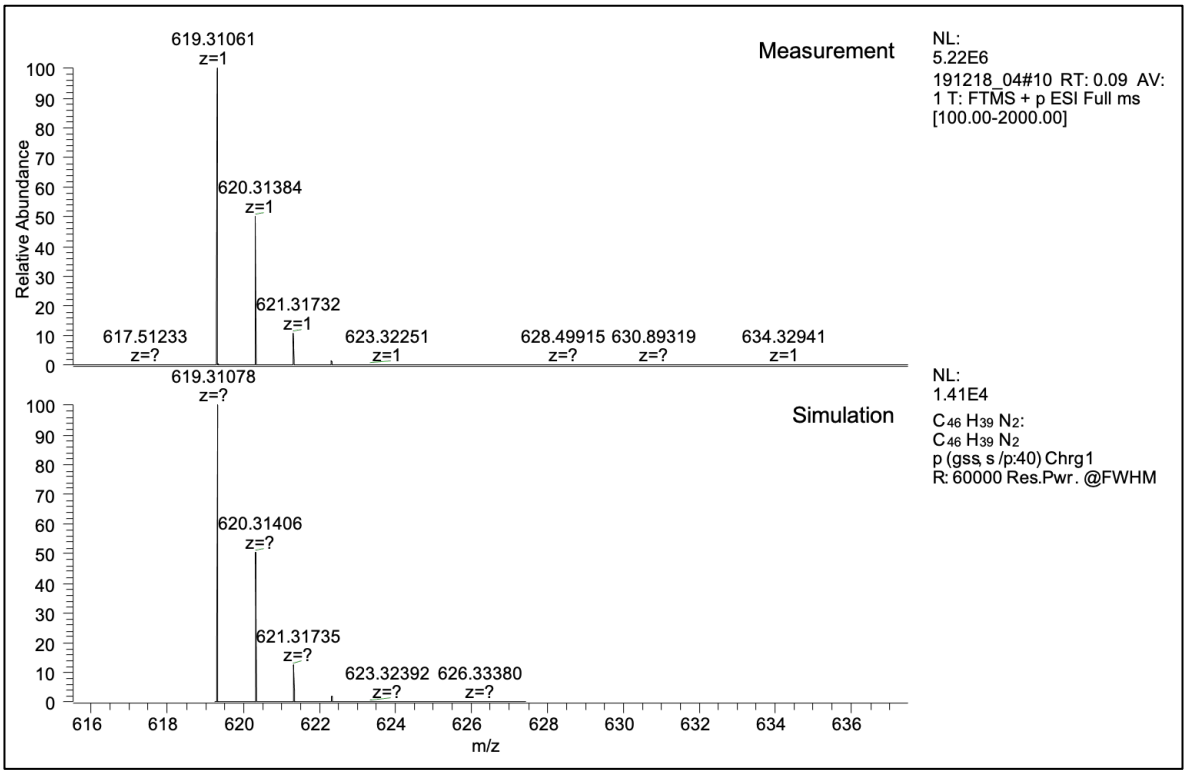

Figure S2.12: Mass spectrum and simulation of **AZ-6CPP**.

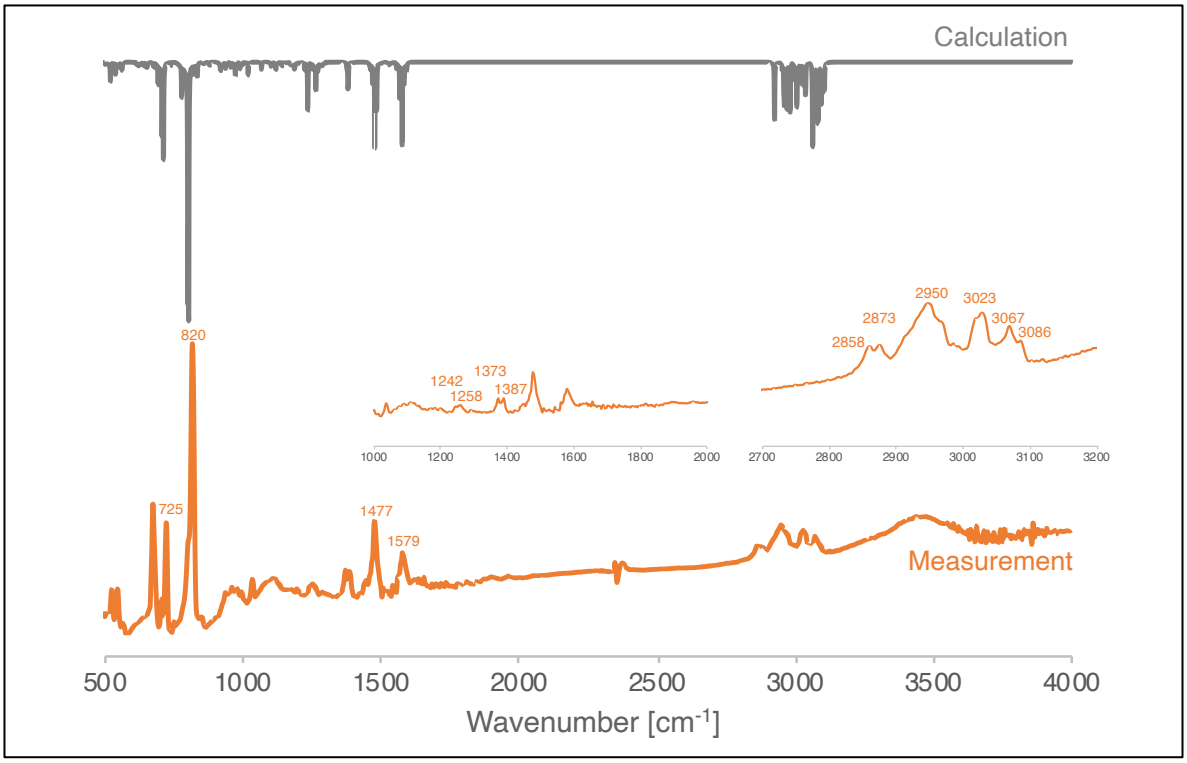

Figure S2.13: Experimental and computed IR spectra of **AZ-6CPP**.

Table S2.1: Crystal data and structure refinement for **AZ-6CPP** ith thermal ellipsoids at 50% probability (gray : C, blue : N, green : Cl, white : H).

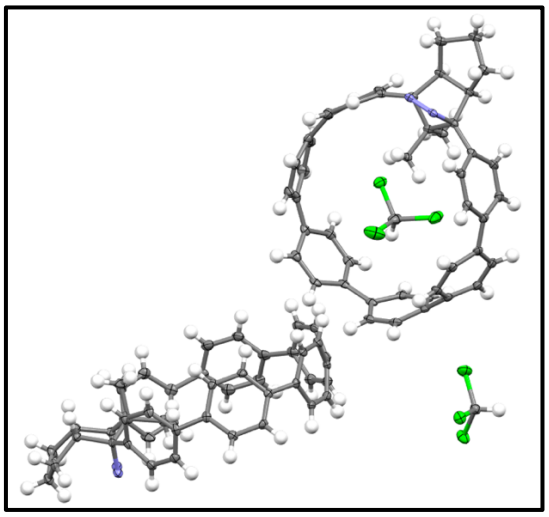

Type of the radiation	MoKα
Formula	$C_{47}H_{39}Cl_3N_2$
Weight	738.15
Temperature *T* (K)	100
Wavelength λ (Å)	0.71073
Crystal system	Monoclinic
Space group	$P12_1/c1$
Unit cell	a (Å) = 24.407(3) α (deg) = 90 b (Å) = 17.4140(18) β (deg) = 112.392(1) c (Å) = 18.814(2) γ (deg) = 90
Volume	7393.5.(13)
z	8
Density (calculation)	1.326
μ (mm^{-1})	0.285
F(000)	3088.0
Crystal shape	block
Color	colorless
Cryst size (mm^3)	0.20×0.10×0.05
Theta range for data collection (deg)	2.3391 to 26.5798
Index ranges	−17<=h<=30, −22<=k<=21, −23<=l<=23
Number of Reflns	15734
Params	941
Goodness-of-fit on F^2	1.020
*R*1, *wR*2 [*I*>2σ (*I*)]	0.0478, 0.1007
*R*1, *wR*2 (all data)	0.0813, 0.1144

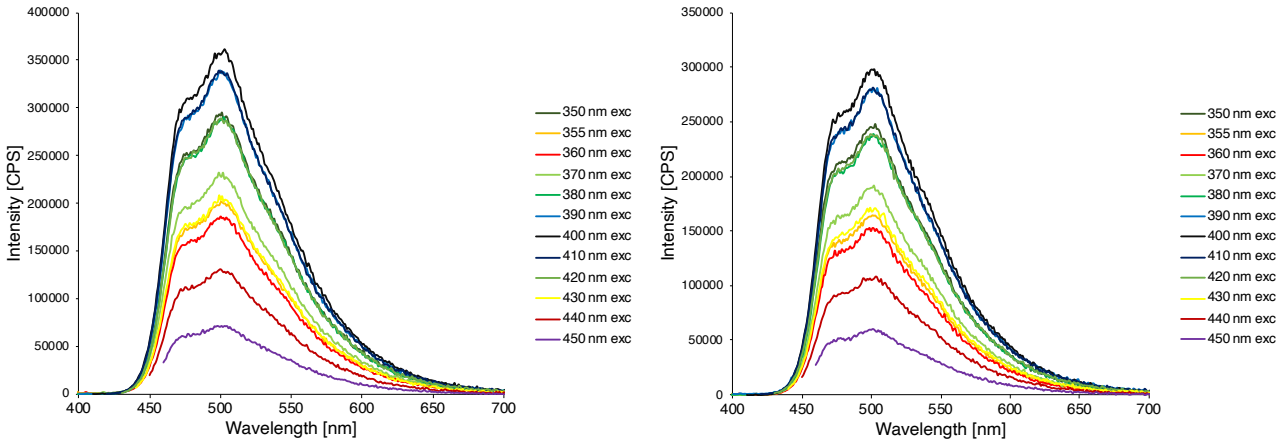

Figure S2.14. Emission spectra of **AZ-6CPP** (benzene solution : 11 μM, under N2 (left) and air (right) condition).

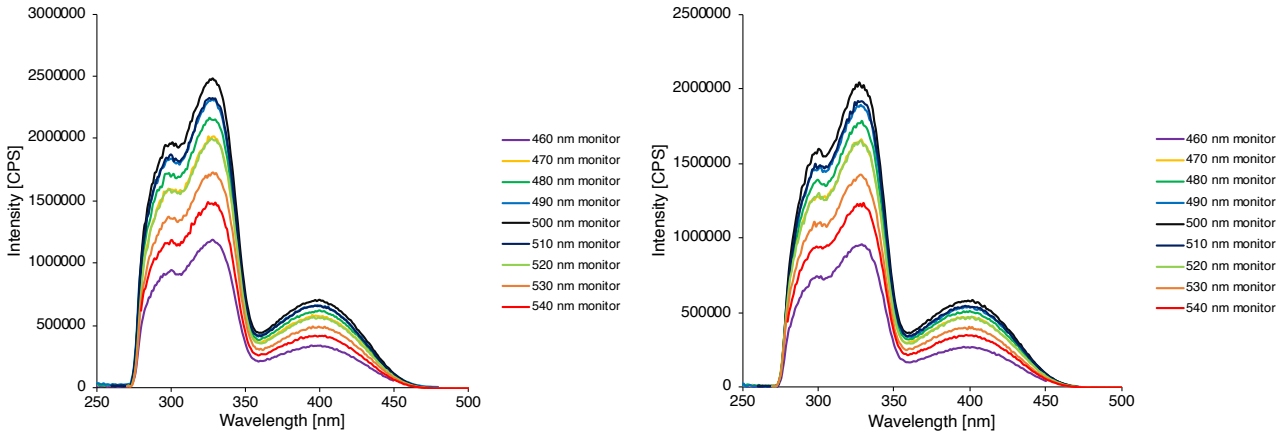

Figure S2.15: Excitation spectra of **AZ-6CPP** (benzene solution : 11 μM, under N_2 (left) and air (right) condition).

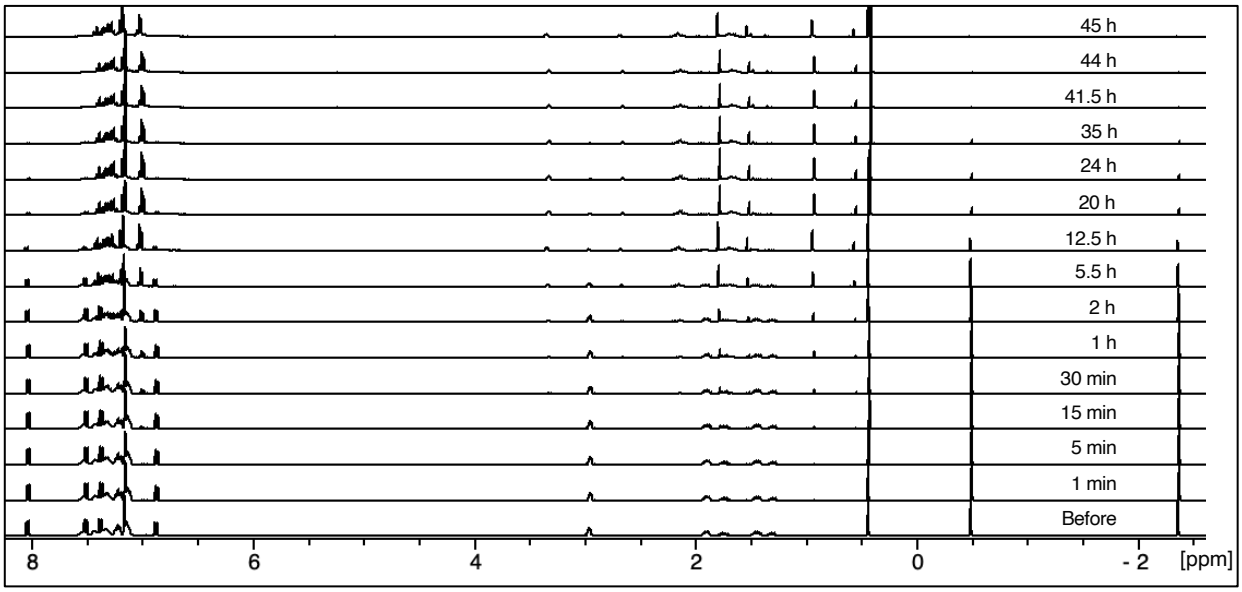

Figure S2.16: In-situ ^{1}H NMR analysis of photolysis of **AZ-6CPP** in degassed C_6D_6 with 355 nm laser.

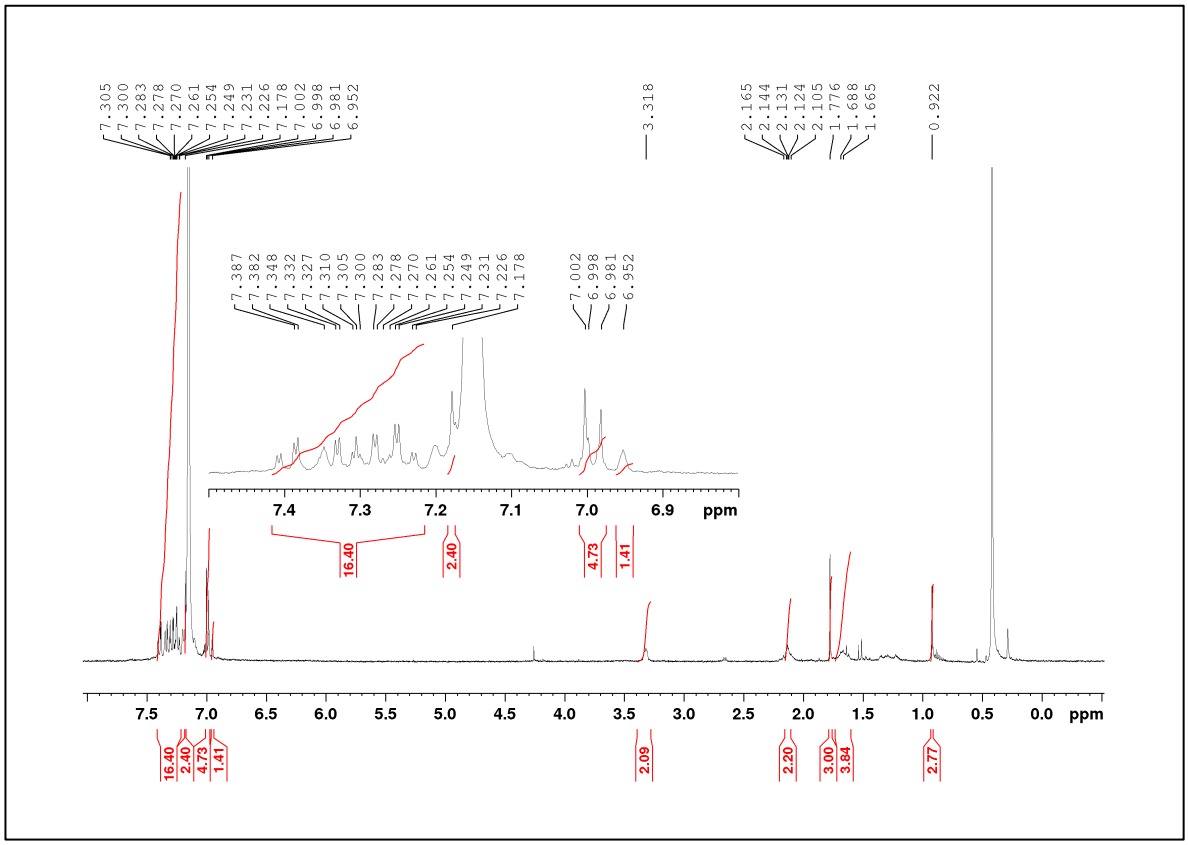

Figure S2.17: [1]H NMR spectrum of photoreaction product (**Trans-CP**).

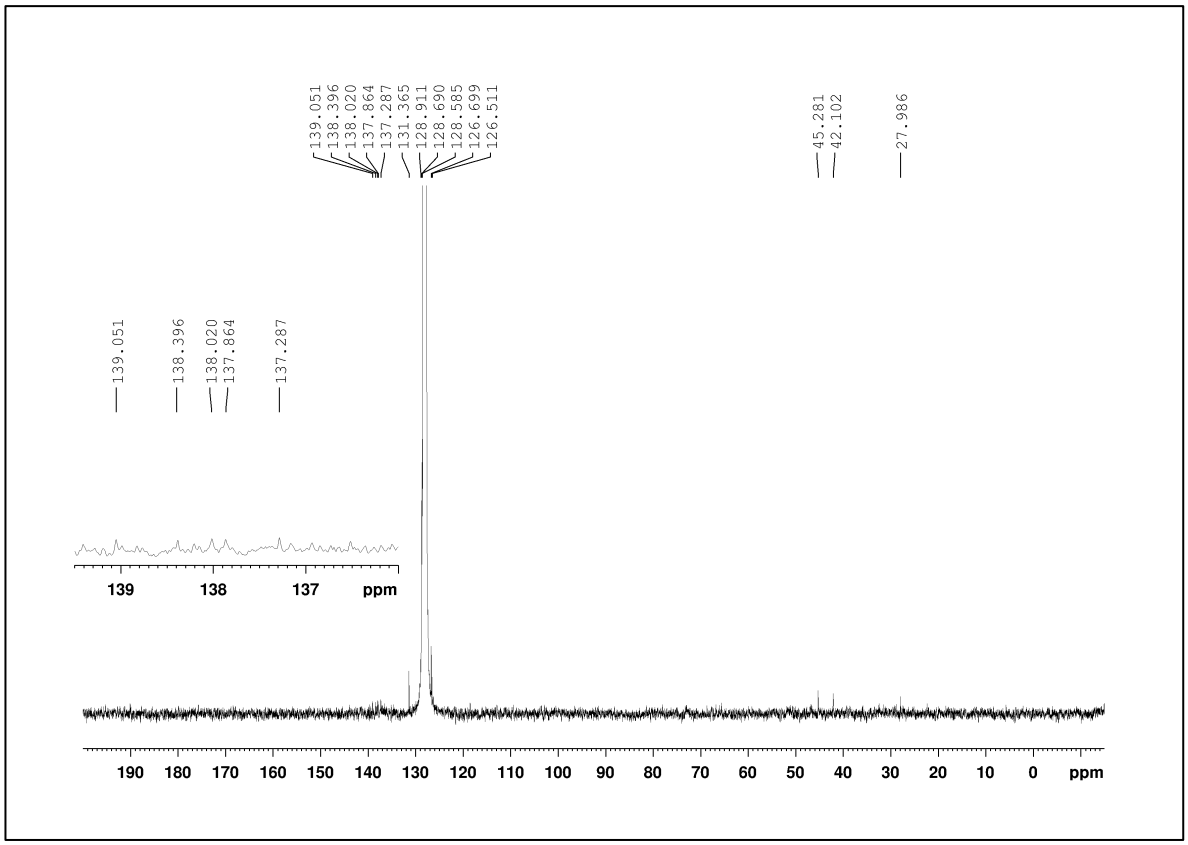

Figure S2.18: [13]C NMR spectrum of photoreaction product (**Trans-CP**).

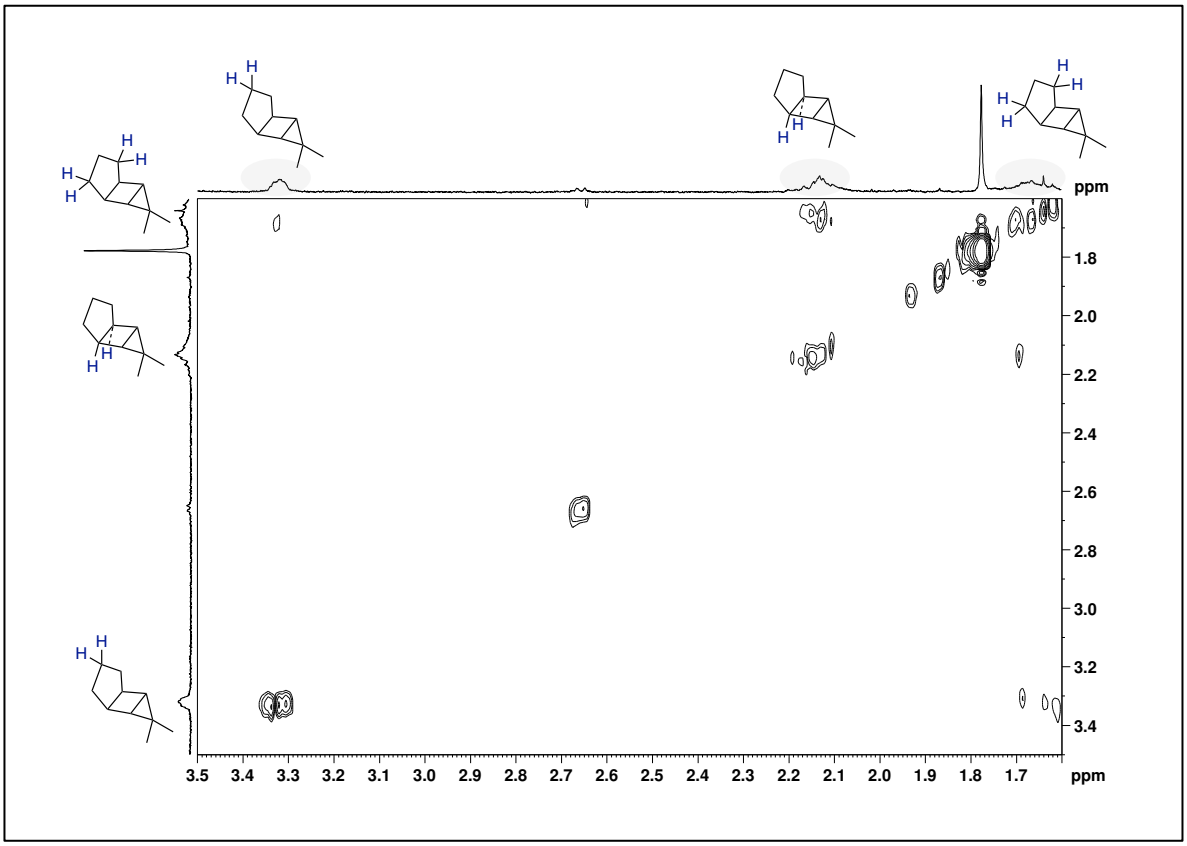

Figure S2.19: COSY spectrum of photoreaction product (**Trans-CP**).

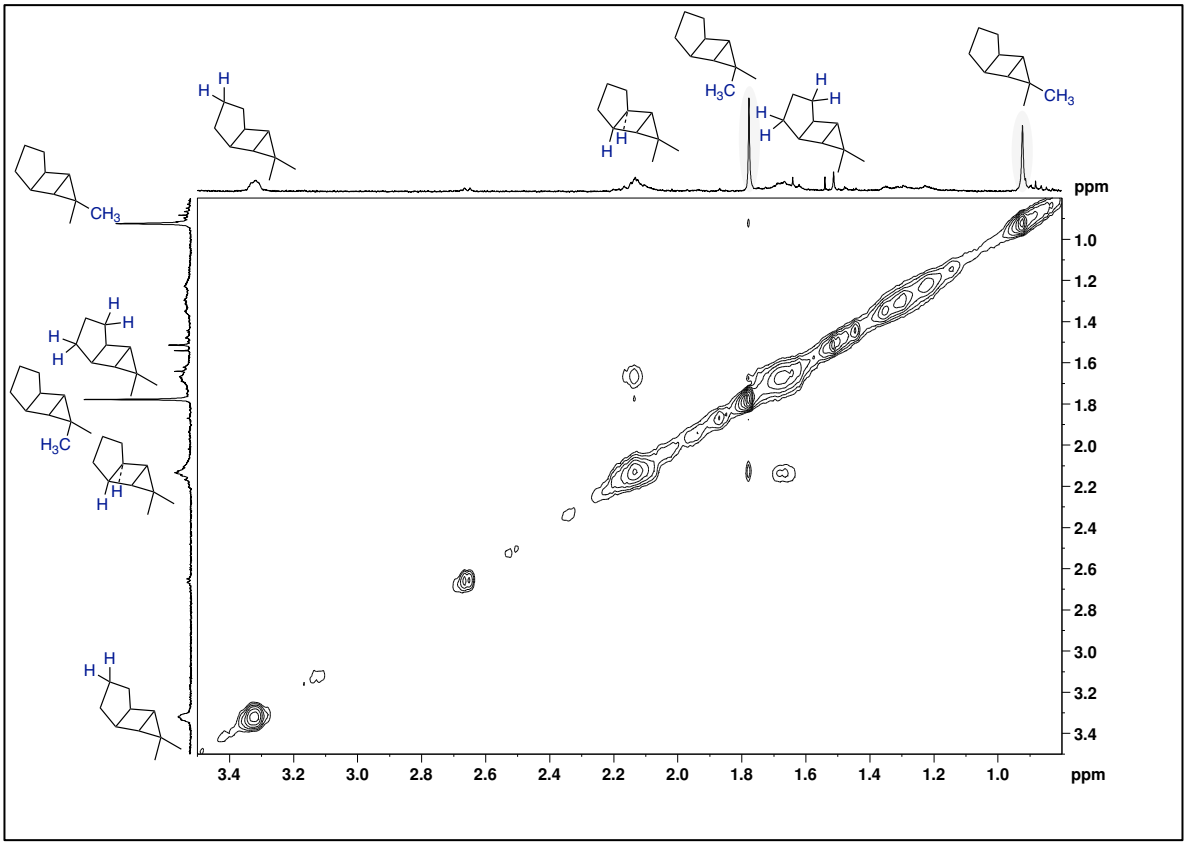

Figure S2.20. NOESY spectrum of photoreaction product (Alkyl region, **Trans-CP**).

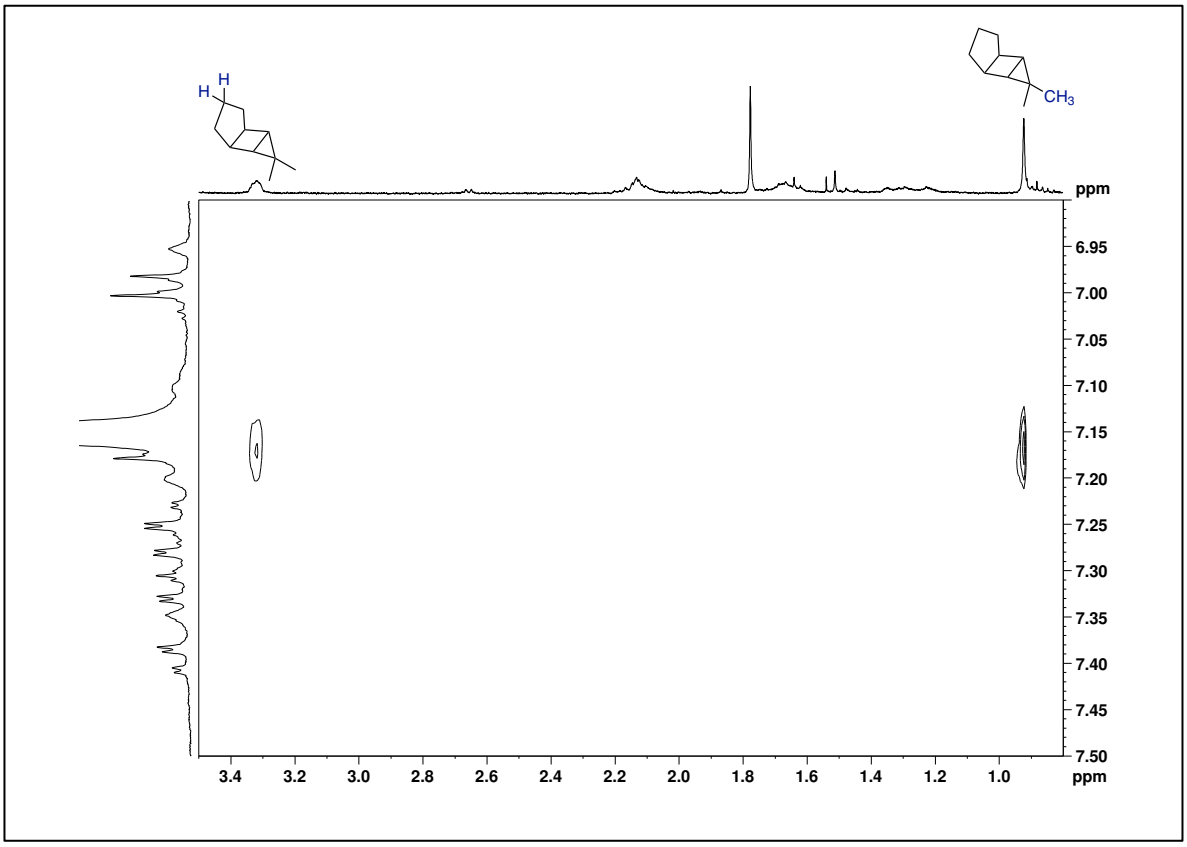

Figure S2.21: NOESY spectrum of photoreaction product (Aromatic region, **Trans-CP**).

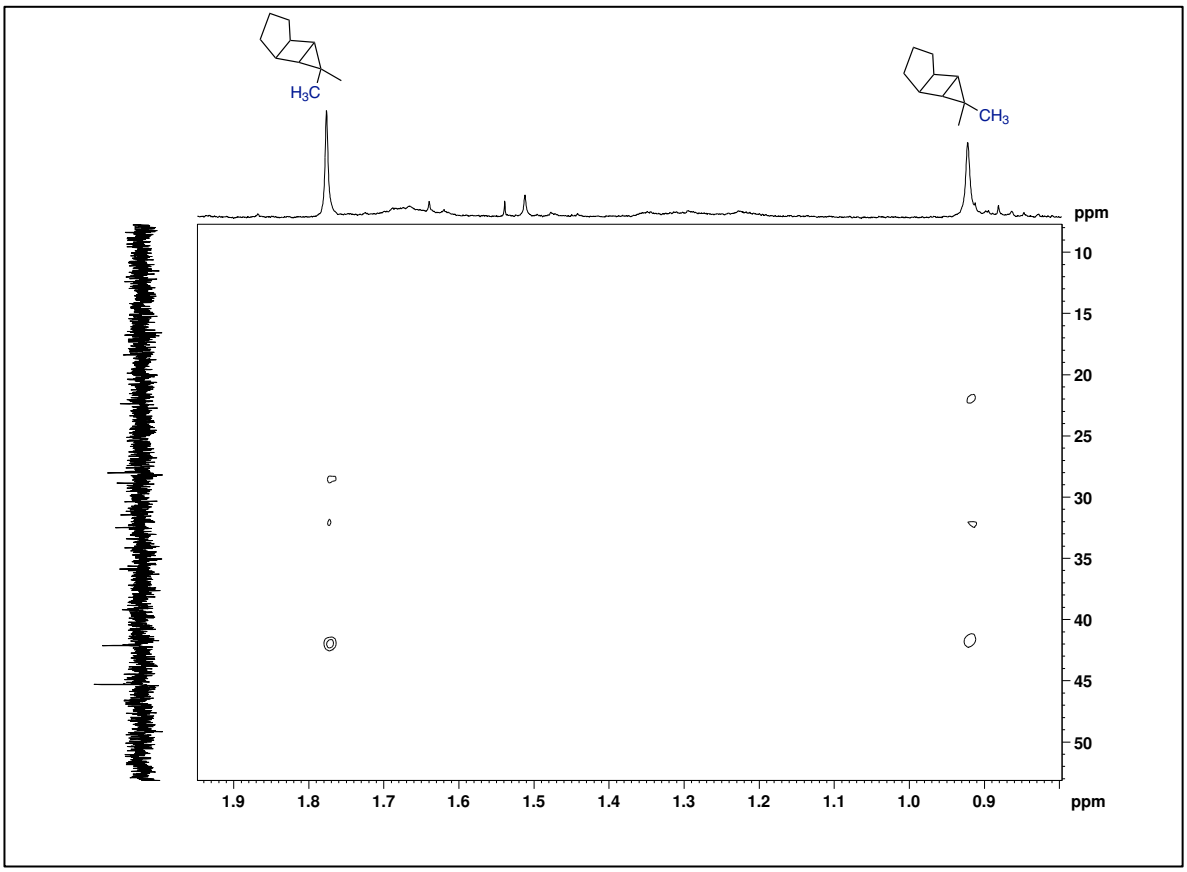

Figure S2.22: HMBC spectrum of photoreaction product (Alkyl region, **Trans-CP**).

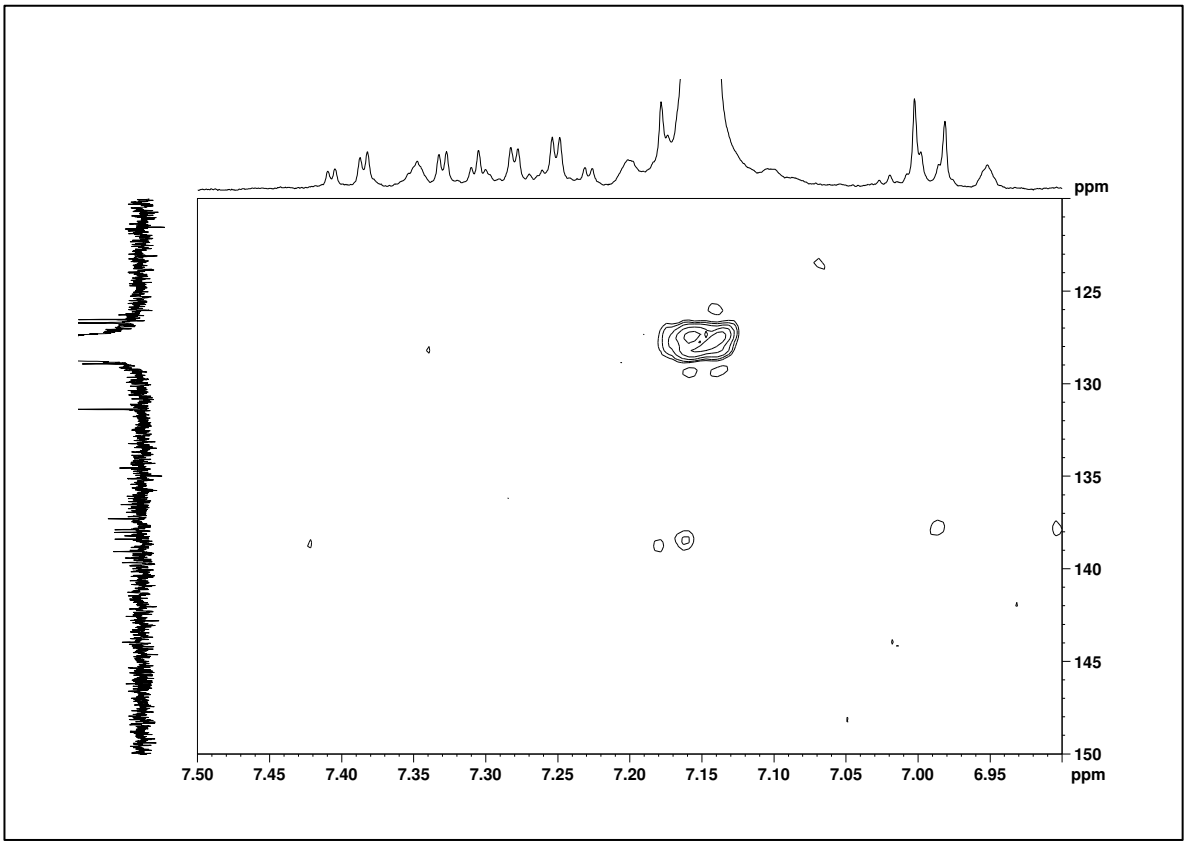

Figure S2.23: HMBC spectrum of photoreaction product (Aromatic region, **Trans-CP**).

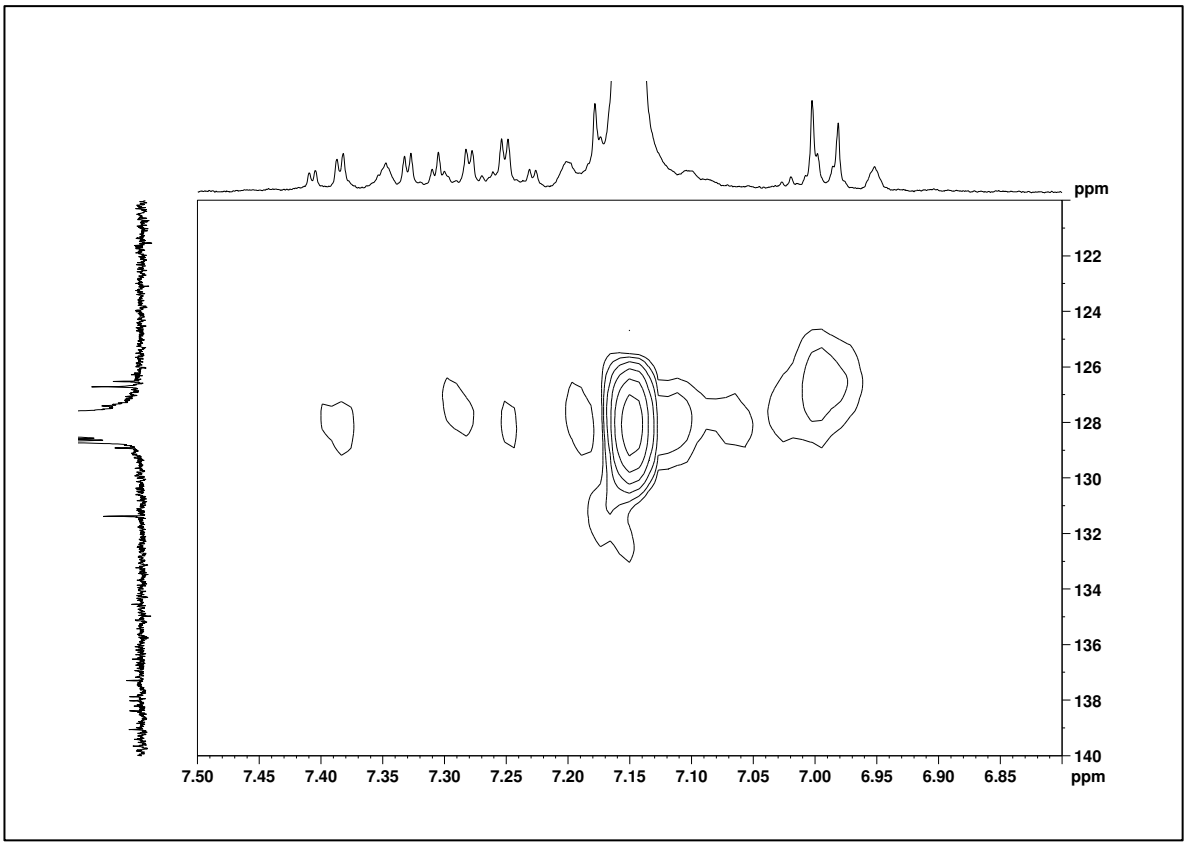

Figure S2.24: HSQC spectrum of photoreaction product (Aromatic region, **Trans-CP**).

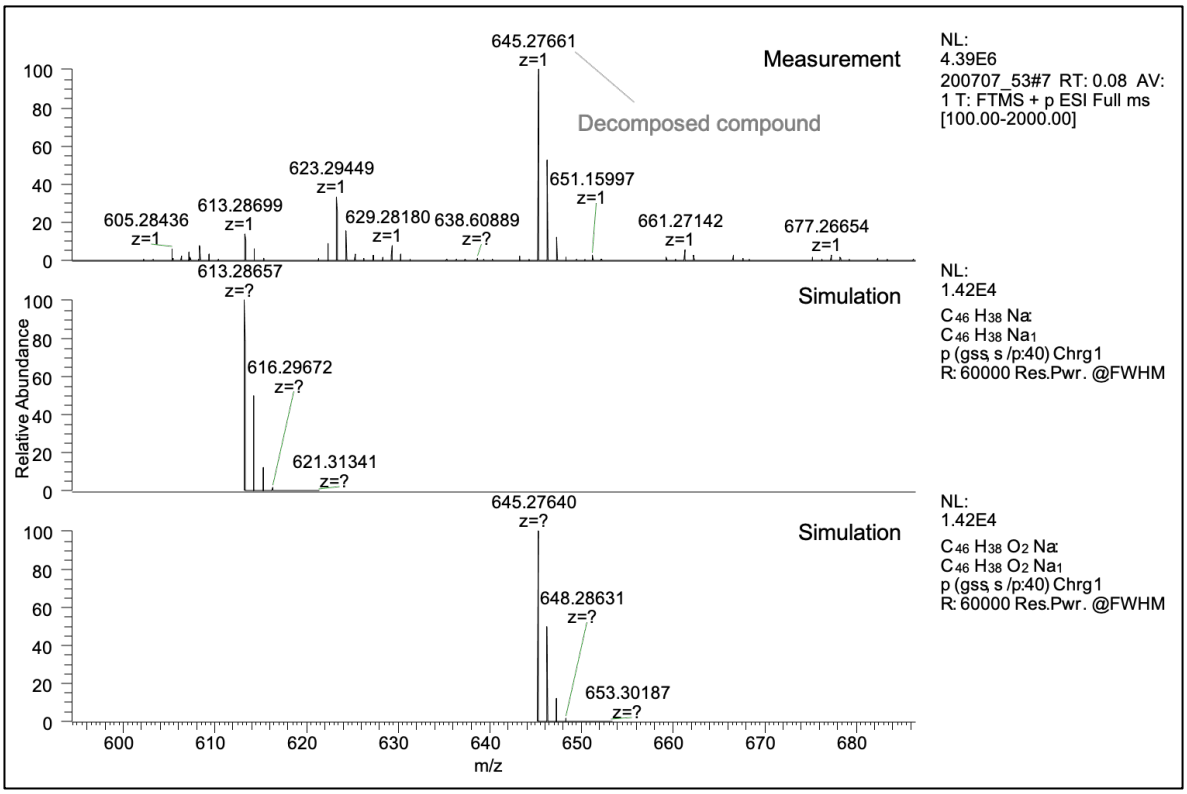

Figure S2.25: Mass spectrum and simulation of photoreaction product (**Trans-CP**).

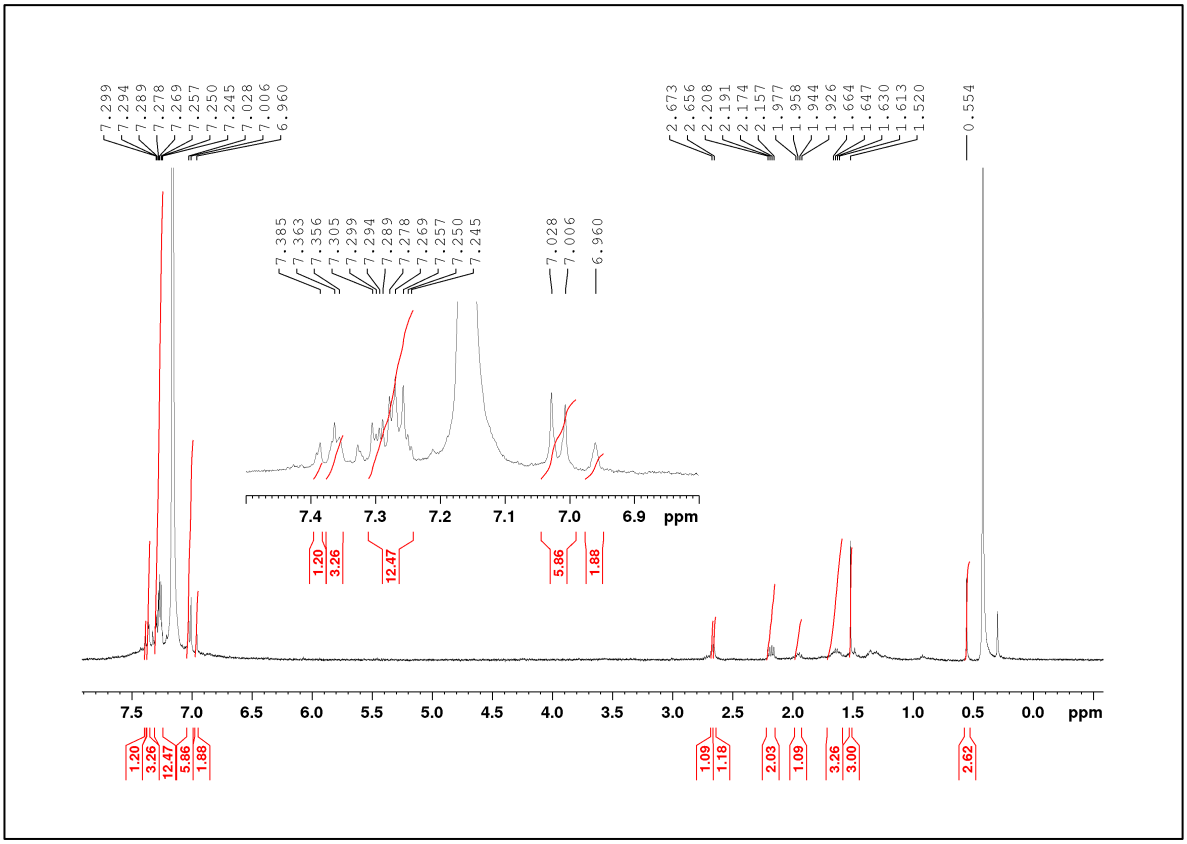

Figure S2.26: ^{1}H NMR spectrum of photoreaction product (**MG**).

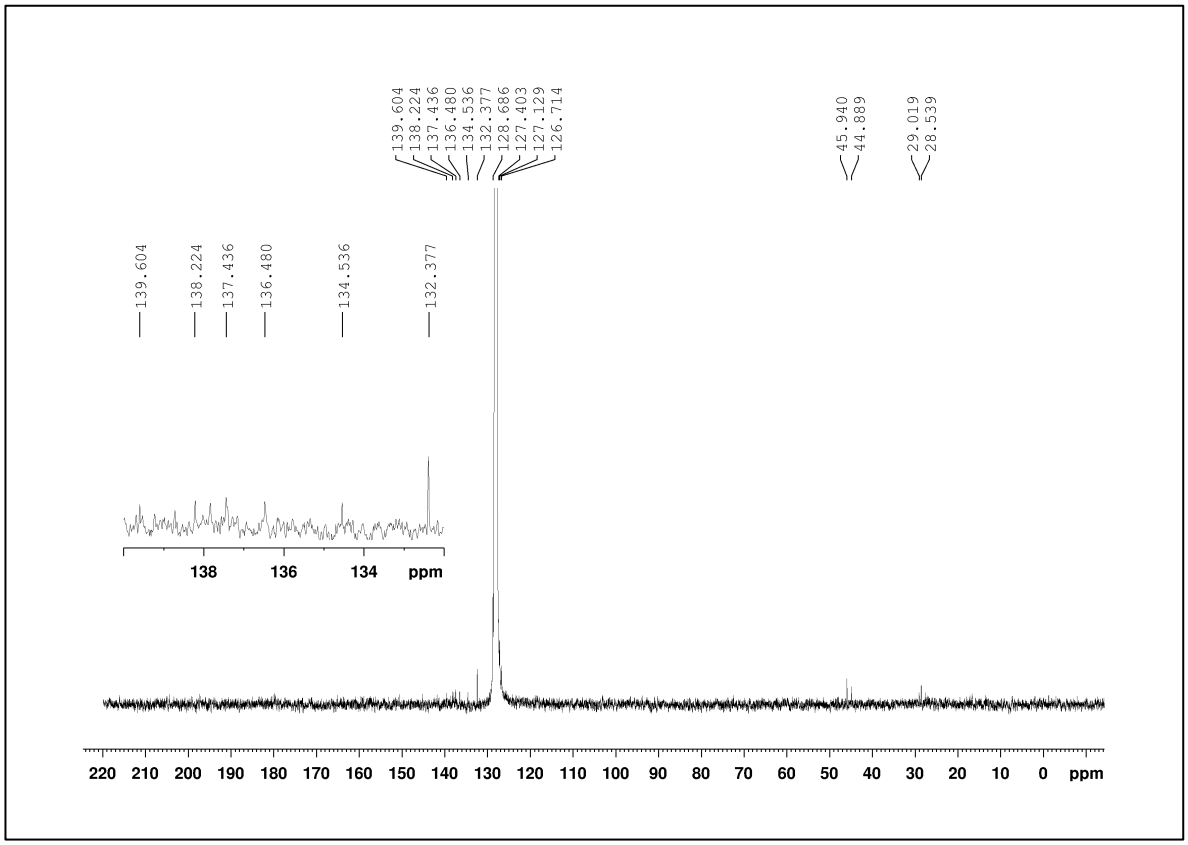

Figure S2.27: ^{13}C NMR spectrum of photoreaction product (**MG**).

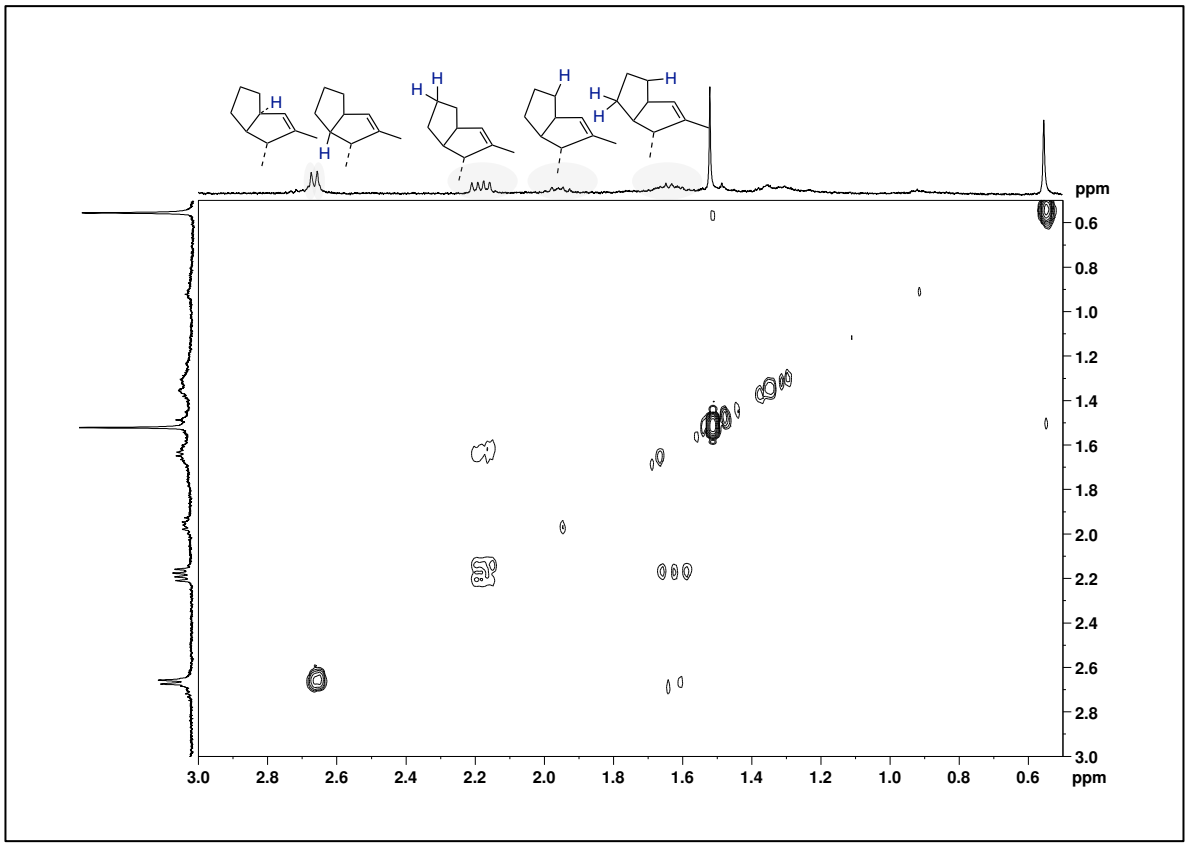

Figure S2.28: COSY spectrum of photoreaction product (**MG**).

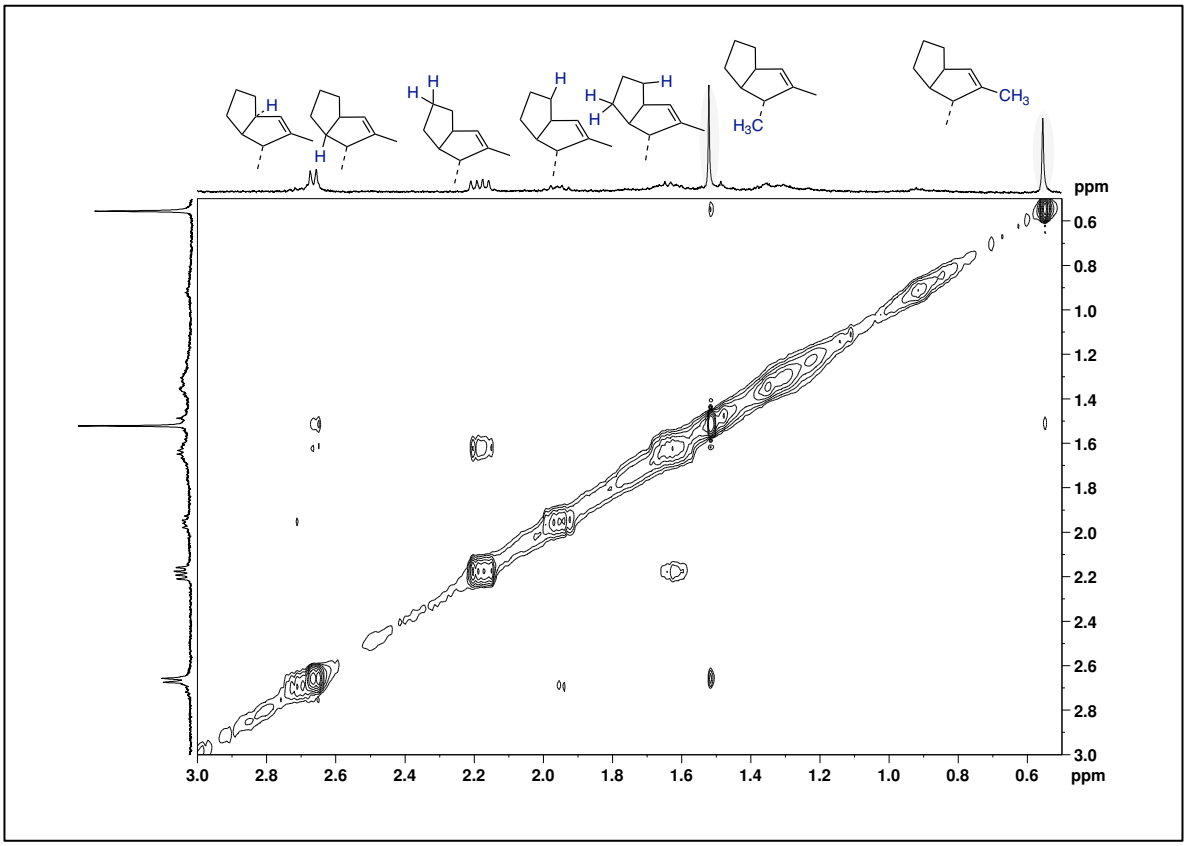

Figure S2.29: NOESY spectrum of photoreaction product (Alkyl region, **MG**).

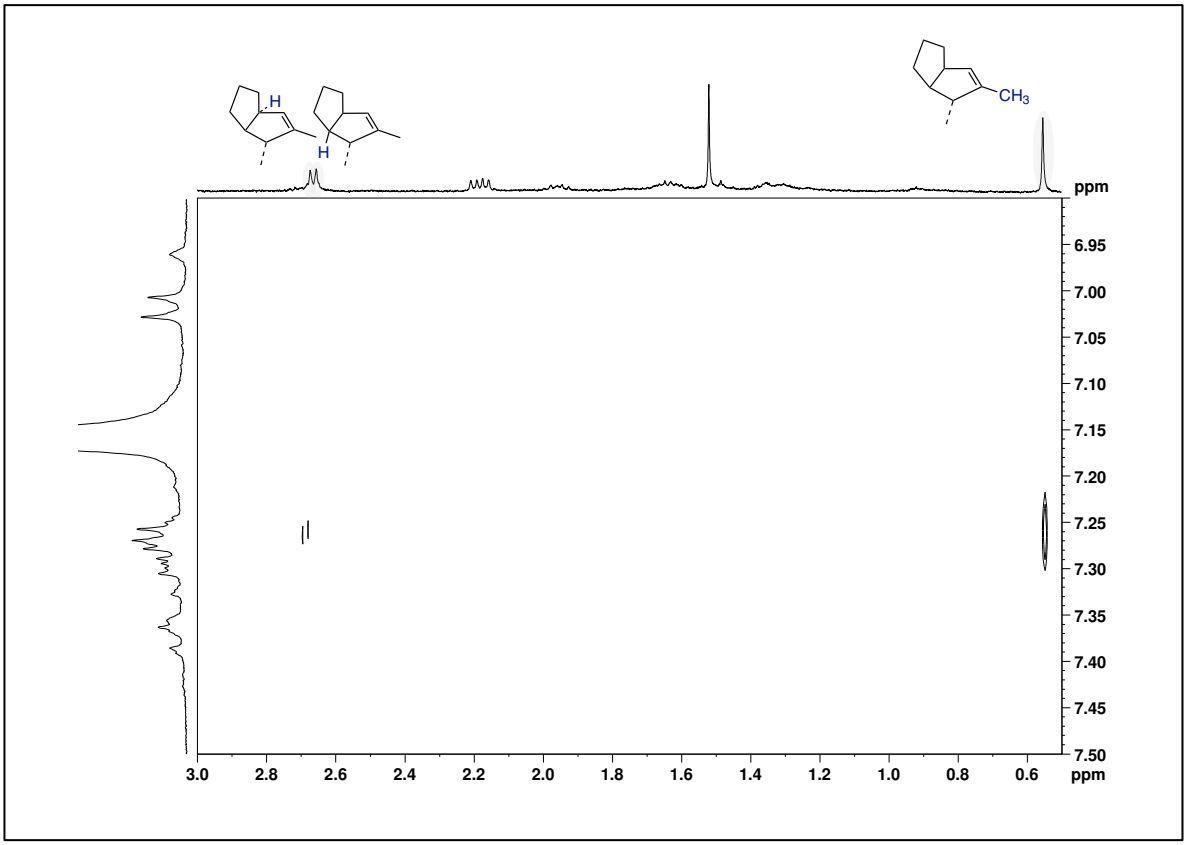

Figure S2.30: NOESY spectrum of photoreaction product (Aromatic region, **MG**).

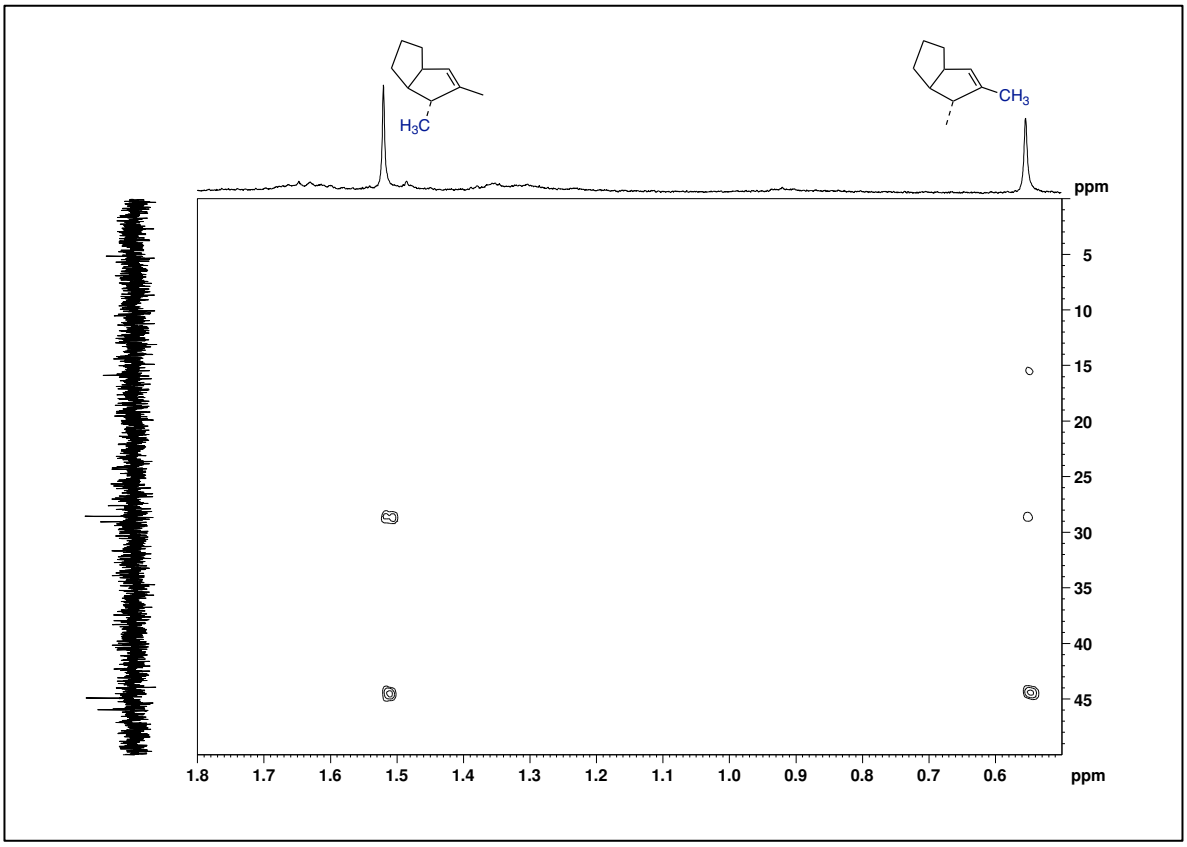

Figure S2.31: HMBC spectrum of photoreaction product (Alkyl region, **MG**).

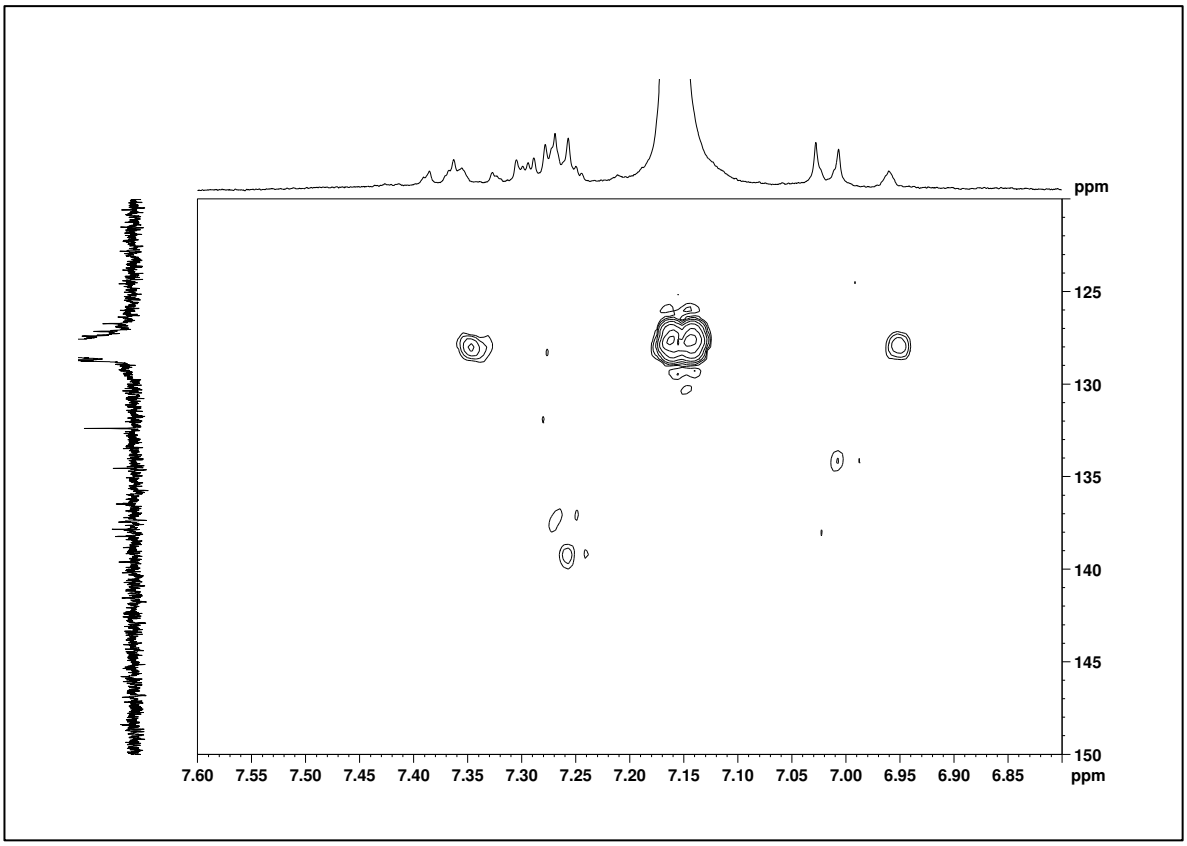

Figure S2.32: HMBC spectrum of photoreaction product (Aromatic region, **MG**).

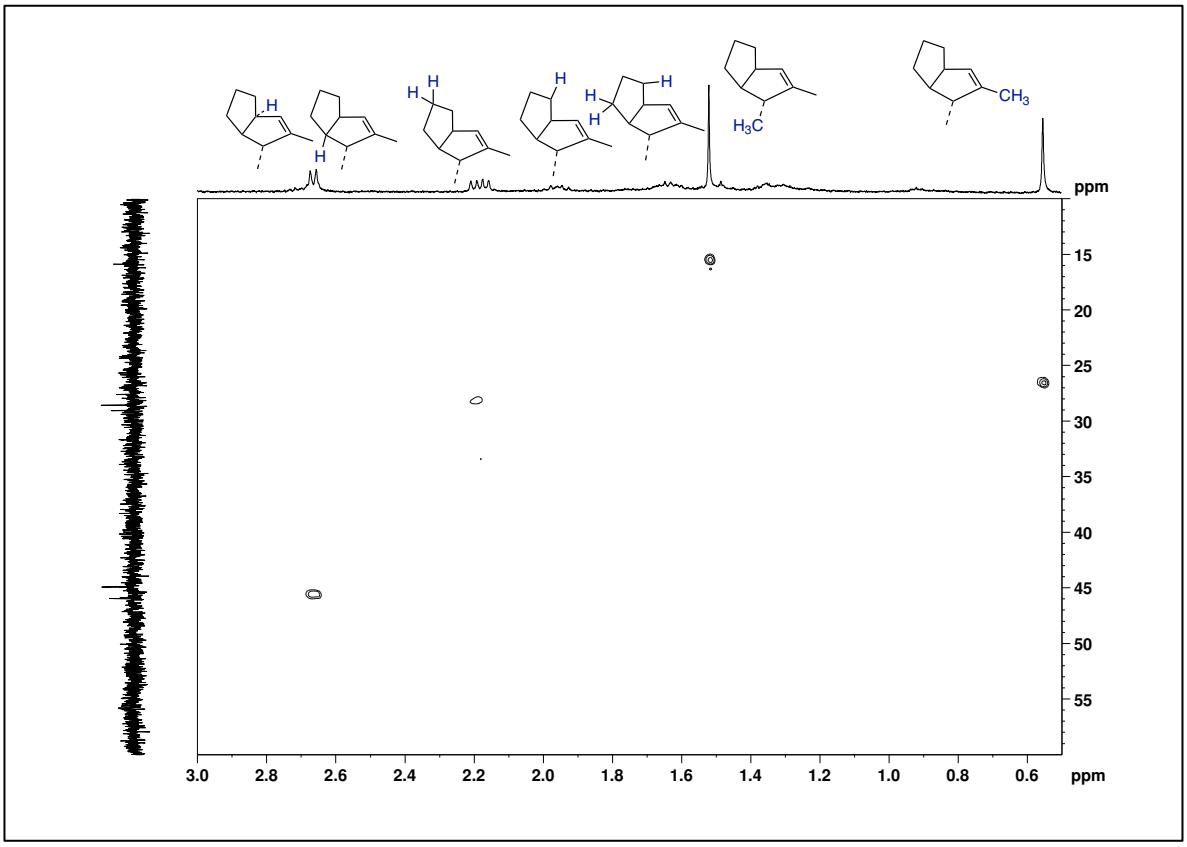

Figure S2.33: HSQC spectrum of photoreaction product (Alkyl region, **MG**).

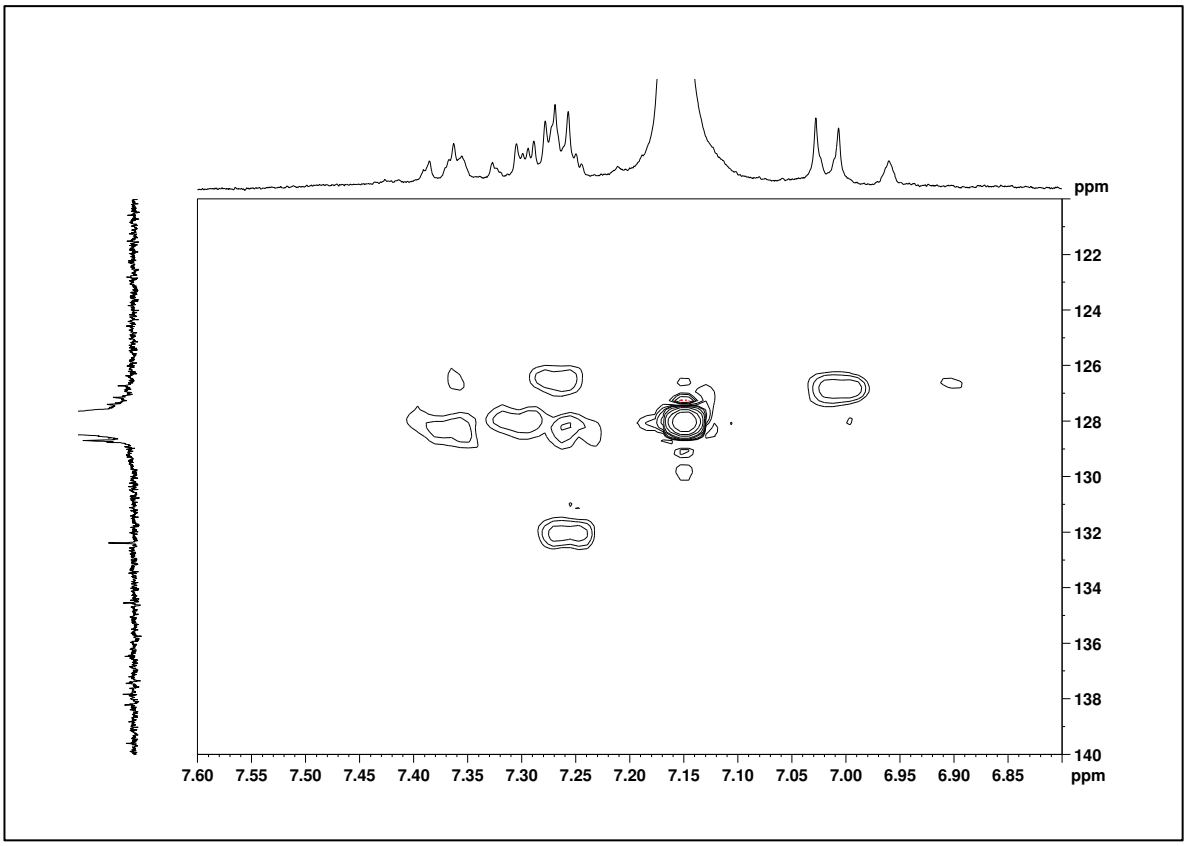

Figure S2.34: HSQC spectrum of photoreaction product (Aromatic region, **MG**).

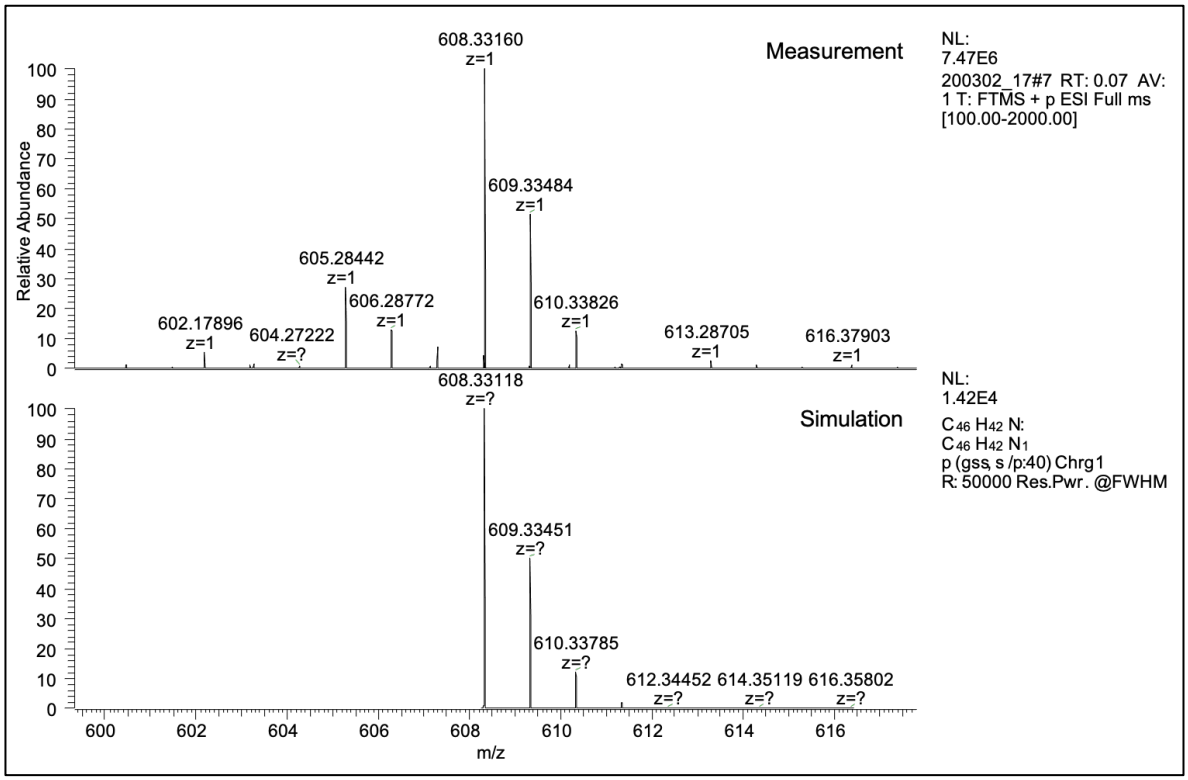

Figure S2.35: Mass spectrum and simulation of photoreaction product (**MG**).

Photoreaction product (**Trans-CP**)

^{1}H NMR (C_6D_6, 400 MHz) δ 0.92 (s, 3H), 1.66–1.69 (m, 4H), 1.77 (s, 3H), 2.10–2.17 (m, 2H), 3.32 (m, 2H), 6.95–6.98 (d J = 11.8 Hz, 2H), 6.98–7.00 (d J = 8.48 Hz, 4H), 7.18–7.41(m and d, J = 1.96 Hz, J = 2.04 Hz, J = 1.96 Hz, J = 2.08 Hz, J = 2.00 Hz, J = 2.00 Hz, 18H). **^{13}C NMR** (C_6D_6, 100 MHz) δ 27.99, 42.10, 45.28, 126.51, 126.70, 128.59, 128.69, 128.91, 131.36, 137.29, 137.86, 138.02, 138.40, 139.05.

HRMS (p-ESI, MeOH sol) m/z: Calcd for $C_{46}H_{38}Na$ $[M + Na]^+$, 613.28657, found 613.28699. Air sensitive.

Photoreaction product (**MG**)

^{1}H NMR (C_6D_6, 400 MHz) δ 0.55 (s, 3H), 1.52 (s, 3H), 1.61–1.66 (m, 3H), 1.92–1.98 (m, 1H), 2.16–2.21 (m, 2H), 2.66 (s, 1H), 2.67 (s, 1H), 6.96 (s, 2H), 7.01–7.03 (d J = 8.52 Hz, 6H), 7.24–7.39(m, 16H). **^{13}C NMR** (C_6D_6, 100 MHz) δ 28.54, 29.02, 44.89, 45.94, 126.71, 127.13, 127.40, 128.69, 132.38, 134.54, 136.48, 137.44, 138.22, 139.60.

HRMS (p-ESI, MeOH sol) m/z: Calcd for $C_{46}H_{42}N$ $[M + NH_4]^+$, 608.33118, found 608.33160. Air sensitive.

Section 2.9.3: Experimental data.

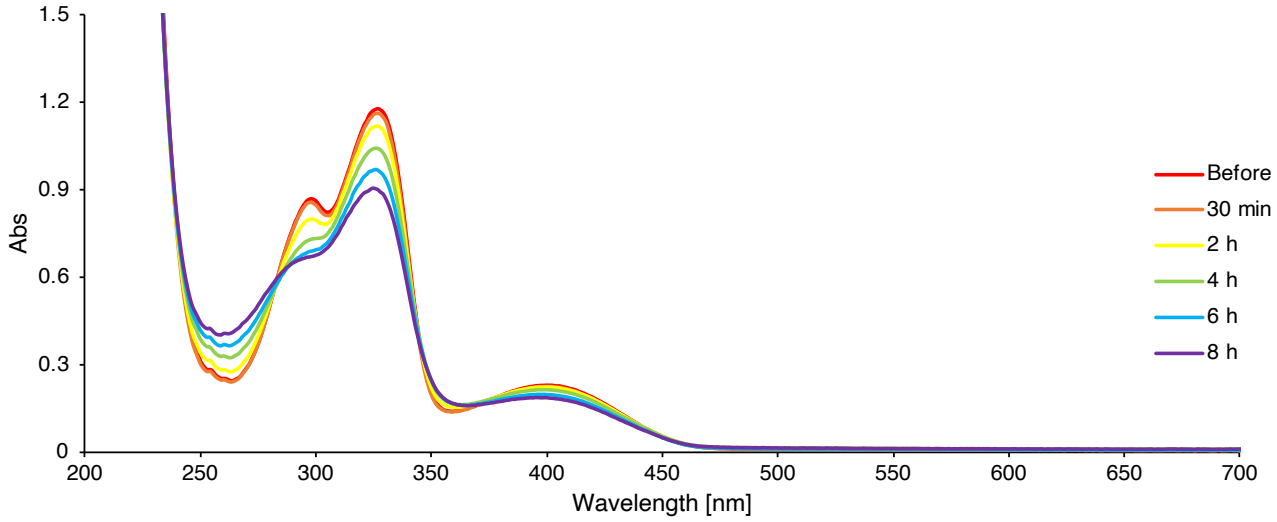

Figure S2.36: Photoreaction of **AZ-6CPP** with 355 nm laser (1.5 mJ) monitored by UV-vis absorption spectroscopy in degassed 2-MTHF solution.

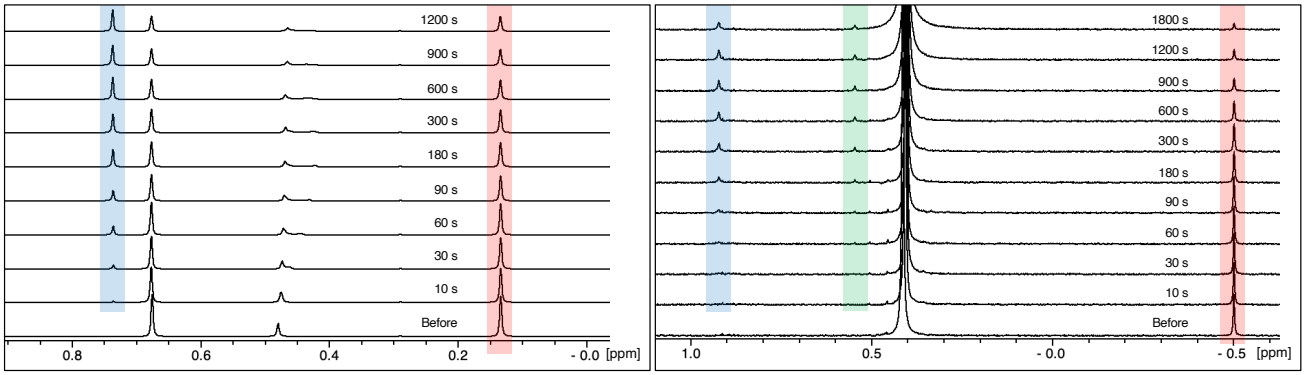

Figure S2.37: In-situ ^{1}H NMR analysis of determination of denitrogenation quantum yield of **AZ-2Ph** (left) and **AZ-6CPP** (right) in degassed C_6D_6 with 355 nm laser.

Table S2.2: Determination parameter of denitrogenation quantum yield of **AZ-2Ph**.

	Integral ratio		**AZ-2Ph**		
Time [s]	0.12 – 0.14 [ppm]	0.73 – 0.75 [ppm]	Ratio [×100 %]	Con : I [mM]	Log[(10^{I_0} – 1) /(10^{I} – 1)]
0	1	0	1	24.2	0
10	1	0.0359	0.9653	23.4	0.016
30	1	0.117	0.8953	21.7	0.049
60	1	0.2777	0.7827	18.9	0.109
90	1	0.4018	0.7134	17.3	0.150
180	1	0.6025	0.6240	15.1	0.209
300	1	0.7239	0.5801	14.0	0.242
600	1	0.9809	0.5048	12.2	0.303
900	1	1.1431	0.4666	11.3	0.338
1200	1	1.2638	0.4417	10.7	0.362

Table S2.3: Determination parameter of denitrogenation quantum yield of **AZ-6CPP**.

	Integral ratio			**AZ-6CPP**		
Time [s]	–0.51 to –0.49 [ppm]	0.915 – 0.935 [ppm]	0.535 – 0.555 [ppm]	Ratio [×100 %]	Con : I [μM]	Log[$(10^{I_0} - 1)$ /$(10^{I} - 1)$]
0	1	0	0	1	30.4	0
10	1	0.0175	0.0075	0.9756	29.6	0.011
30	1	0.043	0.0048	0.9544	29.0	0.020
60	1	0.09	0.0129	0.9067	27.6	0.043
90	1	0.1112	0.0247	0.8804	26.8	0.055
180	1	0.2404	0.0809	0.7568	23.0	0.121
300	1	0.3887	0.1544	0.6480	19.7	0.188
600	1	0.6039	0.2059	0.5525	16.8	0.258
900	1	1.1263	0.4259	0.3918	11.9	0.407
1200	1	1.3163	0.5741	0.3460	10.5	0.461
1800	1	1.6754	0.9881	0.2729	8.3	0.564

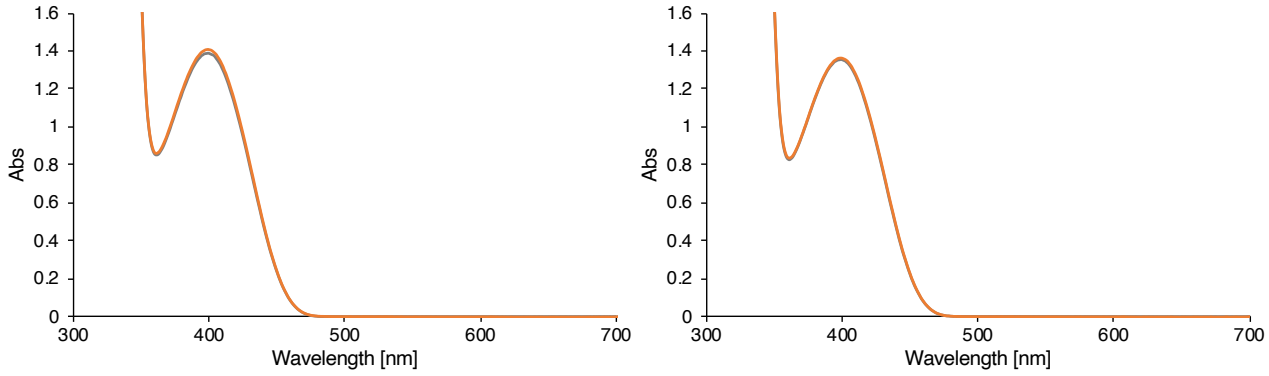

Figure S2.38: UV-vis absorption spectra of sub-microsecond LFP measurement under nitrogen (left) and air (right) atmosphere (gray : before, orange : after, benzene solution : 0.14 mM).

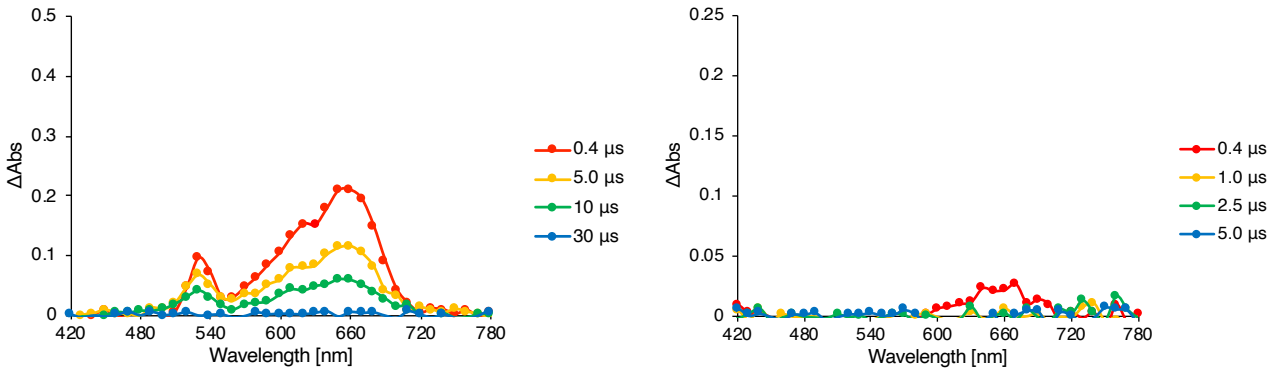

Figure S2.39: Transient absorption spectra of sub-microsecond LFP measurement under nitrogen (left) and air (right) atmosphere with 355 nm laser (5 mJ) in benzene.

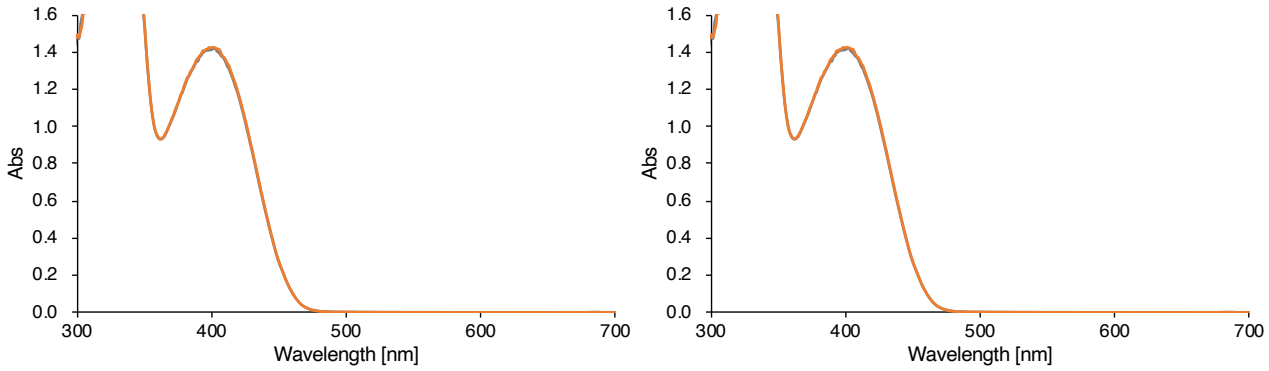

Figure S2.40: UV-vis absorption spectra of sub-nanosecond LFP measurement under argon (left) and right (right) atmosphere (gray : before, orange : after, benzene solution : 0.77 mM).

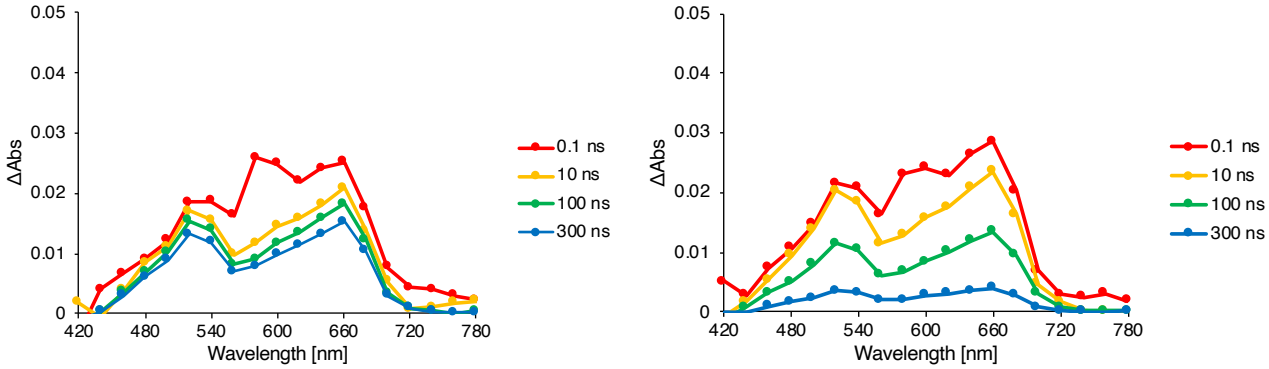

Figure S2.41: Transient absorption spectra of sub-nanosecond LFP measurement under argon (left) and air (right) atmosphere with 355 nm laser in benzene.

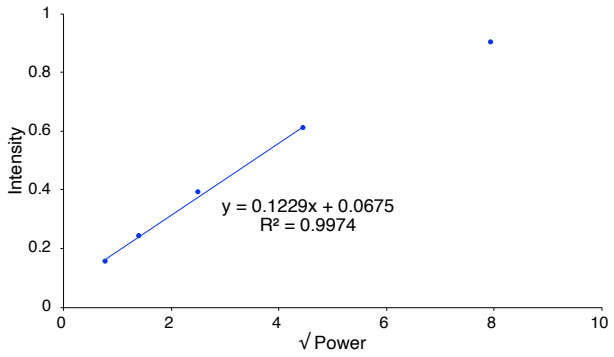

Power P [mW]	$\sqrt{P}$	Signal Intensity I
0.6325	0.7953	0.15635
2	1.4142	0.24353
6.325	2.5150	0.39016
20	4.4721	0.6107
63.25	7.9530	0.90314

Figure S2.42: Signal intensity I vs square microwave power $\sqrt{P}$ plot of EPR measurement.

Section 2.9.4: Computational details.

Quantum chemical computations in gas phase have been performed with the Gaussian 16 (Revision B.01) suite of programs. Charge, spin multiplicity, number of imaginary frequencies, energy (in Hartree) and Cartesian coordinates (in Å) of computed geometries at (R,U)B3LYP/6-31G(d) or (R,U)CAM-B3LYP/6-31G(d) level of theory. The energy minimum structures and transition state structures were confirmed by vibrational frequency analysis. The transition states were further confirmed by intrinsic reaction coordinate (IRC) calculation with the alternative local quadratic approximation (LQA) approach. Zero-field splitting (zfs) parameters (*D* tensor and *E*/*D* ratio) calculation were performed with ORCA 4.2.1 program at restricted open-shell (RO) BP/EPR-II and B3LYP/EPR-II level of theory. The calculated geometries were optimized at (U)B3LYP/6-31G(d) level of theory with Gaussian 16 (Revision B.01) before zfs parameters calculations. The automatic auxiliary basis sets (AutoAux) were used in zfs calculations. The *D* tensor calculation included the spin-spin components (SS). The DSS part is an expectation value that involves the spin density of the calculated system directly used the canonical orbitals from the spin density. 2D-NICS(0)$_{zz}$ plots calculation were conducted at (U)B3LYP/6-31G+(d) level of theory. The software (py.Aroma 3) was used for visualization of 2D-NICS calculations. Anisotropy of the induced current density (ACID) analyses were performed with AICD 3.0.4 software package. The NMR with CSGT method were calculated at UB3LYP/6-31G(d) level of theory. POV-Ray 3.7 on Windows was used for visualization of ACID maps.

The complete active space second order perturbation theory (CASPT2) calculations were performed in conjunction with cc-pVDZ basis set for the model molecules DR-2Ph and DR-2Ph' (endo and exo forms) at DFT optimized geometries. Singlet ground state (S_0) and triplet state (T_1) were considered in state specific approach with no symmetry restrictions. In these calculations 14 active electrons and 14 active orbitals were used in the complete active space (CAS). Thus, all π electrons and all π orbitals were included. The corresponding active space in **DR-6CPP** molecule would encompass 38 active electrons distributed within 38 orbitals what is unavailable at the moment. Therefore, the CASPT2 energies for **DR-6CPP** molecule were not determined. All CASPT2 calculations were performed with Open Molcas program package version py2.14. Molden program was used for molecular plots with space value: 0.03.

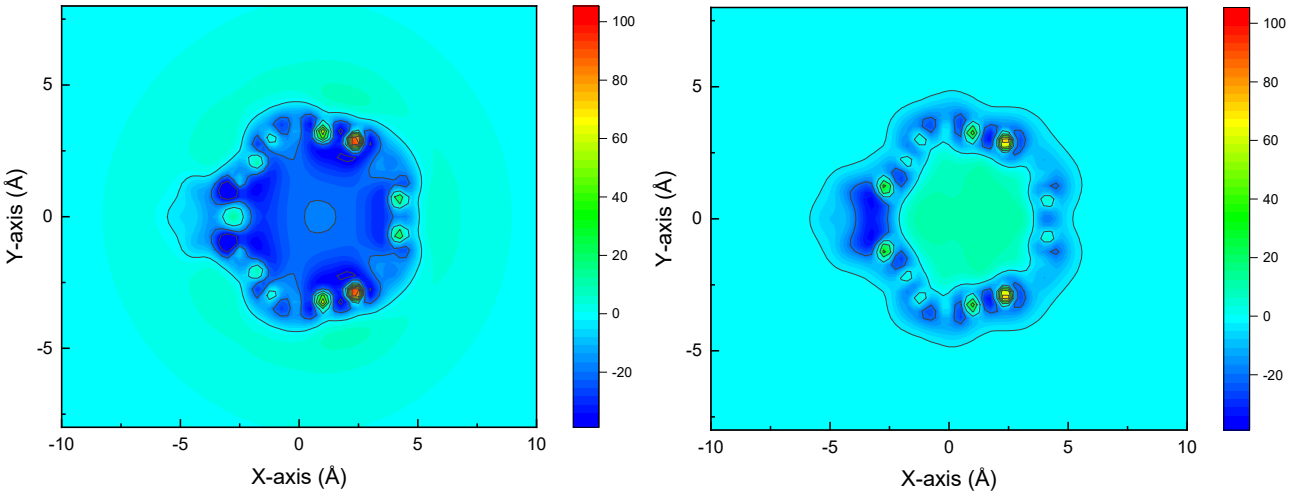

Figure S2.43: A grid plot of the NICS(0)$_{zz}$ value in the XY plane of **S-DR$_{endo}$-4CPP** (left) and **T-DR$_{endo}$-4CPP** (right).

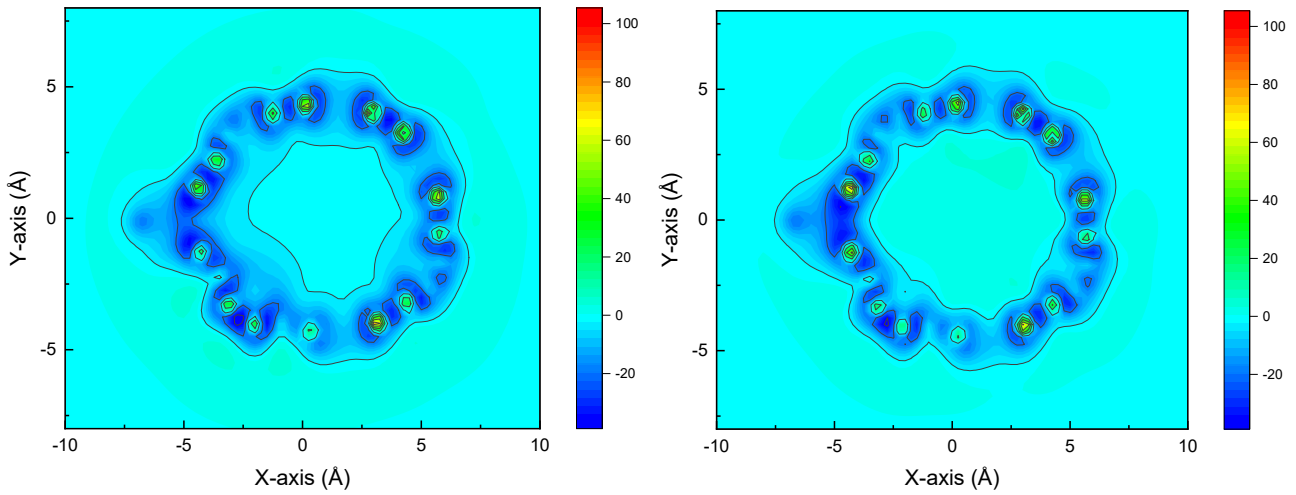

Figure S2.44: A grid plot of the NICS(0)$_{zz}$ value in the XY plane of **S-DR$_{endo}$-6CPP** (left) and **T-DR$_{endo}$-6CPP** (right).

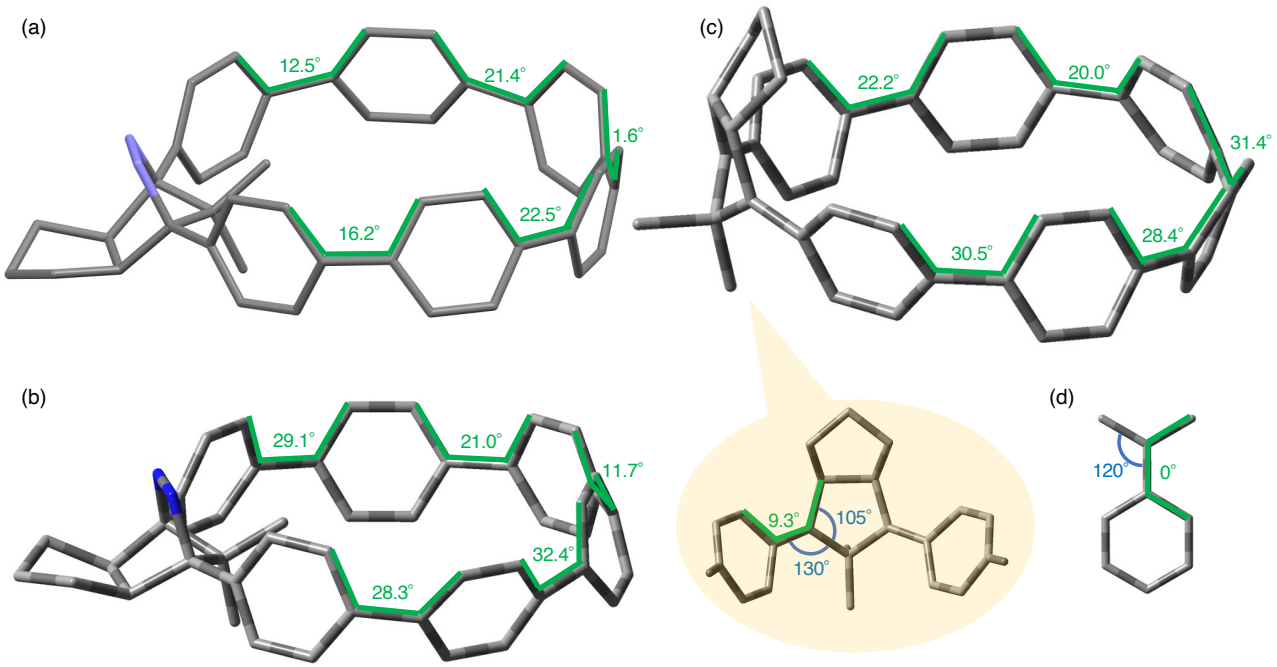

Figure S2.45: Dihedral angle of the **AZ-6CPP** of (a) X-ray structure (b) computed structure at RCAM-B3LYP/6-31G(d) level of theory. (c) Dihedral angle of the triplet diradical **DR-6CPP** computed structure at UCAM-B3LYP/6-31G(d) level of theory. (d) Dihedral angle of α-dimethyl benzyl radical computed structure at UCAM-B3LYP/6-31G(d) level of theory. Hydrogen atoms are omitted for clarity.

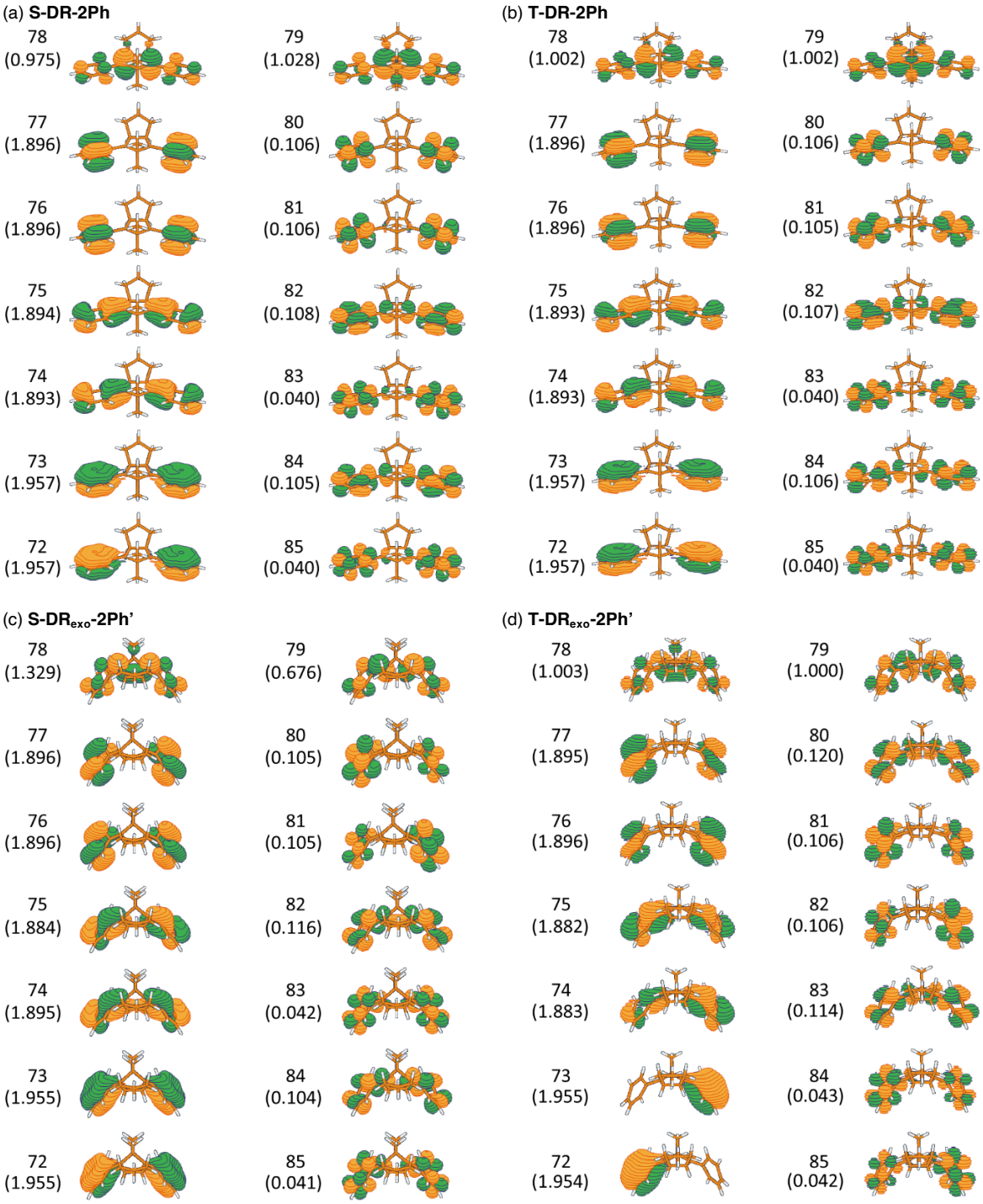
(a) S-DR-2Ph
78 (0.975)
79 (1.028)
77 (1.896)
80 (0.106)
76 (1.896)
81 (0.106)
75 (1.894)
82 (0.108)
74 (1.893)
83 (0.040)
73 (1.957)
84 (0.105)
72 (1.957)
85 (0.040)
(b) T-DR-2Ph
78 (1.002)
79 (1.002)
77 (1.896)
80 (0.106)
76 (1.896)
81 (0.105)
75 (1.893)
82 (0.107)
74 (1.893)
83 (0.040)
73 (1.957)
84 (0.106)
72 (1.957)
85 (0.040)
(c) S-DR$_{exo}$-2Ph'
78 (1.329)
79 (0.676)
77 (1.896)
80 (0.105)
76 (1.896)
81 (0.105)
75 (1.884)
82 (0.116)
74 (1.895)
83 (0.042)
73 (1.955)
84 (0.104)
72 (1.955)
85 (0.041)
(d) T-DR$_{exo}$-2Ph'
78 (1.003)
79 (1.000)
77 (1.895)
80 (0.120)
76 (1.896)
81 (0.106)
75 (1.882)
82 (0.106)
74 (1.883)
83 (0.114)
73 (1.955)
84 (0.043)
72 (1.954)
85 (0.042)

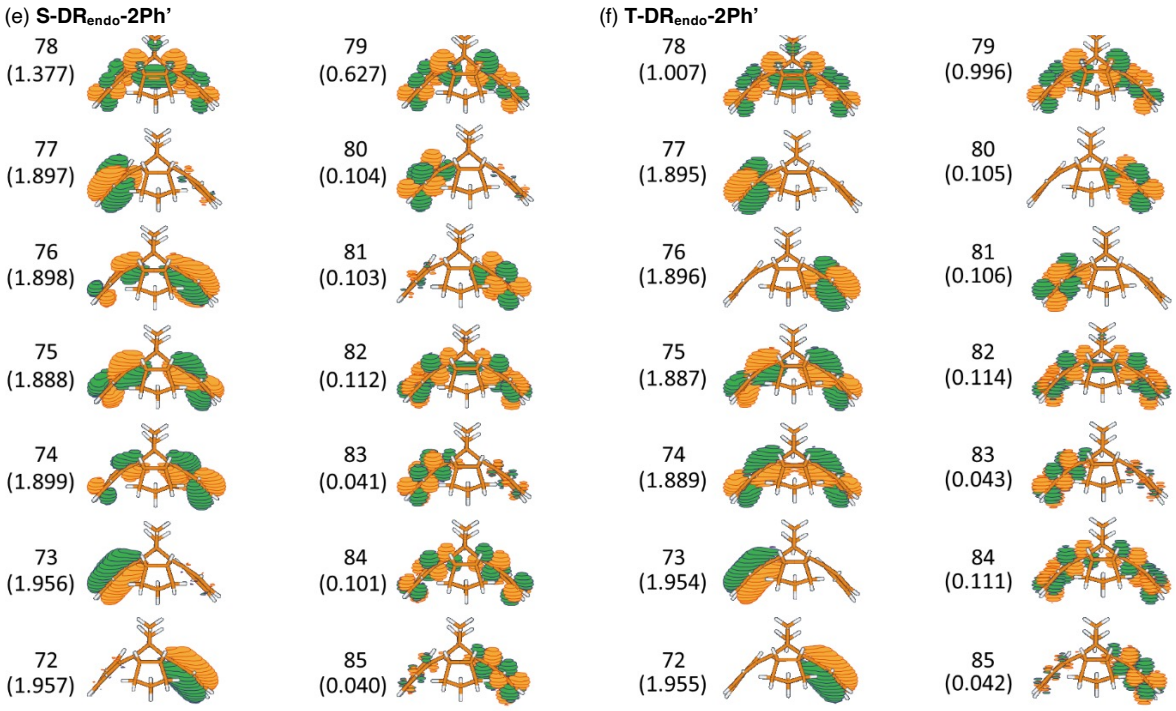

Figure S2.46: Active CASSCF orbitals and their occupation numbers (in parentheses) for **DR-2Ph** (a) singlet and (b) triplet state as well for **DR$_{exo}$-2Ph'** (c) singlet, (d) triplet state, for **DR$_{endo}$-2Ph'** (e) singlet, and (f) triplet state.

Table S2.4: The S_0 and the T_1 total electronic energies ($E_{tot.}$ [a.u.]) and S−T energy gap for **DR-2Ph** and **DR-2Ph'** and weights of leading configurations (for singlet state Φ_1 = 22222220000000, Φ_2 = 22222202000000; for triplet state Φ_3 = 22222211000000).

DR-2Ph	Singlet (Ground state, S_0)	Triplet (T_1)	ΔE_{S-T} gap (kcal / mol)
CASSCF(14,14)/cc-pVDZ	-847.22339	-847.22398	0.4
CASPT2(14,14)/cc-pVDZ	-850.00294	-850.00326	0.2
weight (Φ_1 or Φ_3) / %	37.09	72.08	
weight (Φ_2) / %	34.87		

DR$_{exo}$-2Ph'	Singlet (Ground state, S_0)	Triplet (T_1)	ΔE_{S-T} gap (kcal / mol)
CASSCF(14,14)/cc-pVDZ	-847.18908	-847.18788	-0.8
CASPT2(14,14)/cc-pVDZ	-849.97587	-849.9726	-2.1
weight (Φ_1 or Φ_3) / %	49.26	70.64	
weight (Φ_2) / %	21.81		

DR$_{endo}$-2Ph'	Singlet (Ground state, S_0)	Triplet (T_1)	ΔE_{S-T} gap (kcal / mol)
CASSCF(14,14)/cc-pVDZ	-847.18122	-847.17510	-3.8
CASPT2(14,14)/cc-pVDZ	-849.97201	-849.96189	-6.4
weight (Φ_1 or Φ_3) / %	51.65	70.04	
weight (Φ_2) / %	21.18		

Reference.

1. (a) Sun, Z.; Ye, Q.; Chi, C.; Wu, J. *Chem*. *Soc*. *Rev*. **2012**, *41*, 7857–7889. (b) Hwang, H.; Khim, D.; Yun, J. M.; Jung, E.; Jang, S. Y.; Jang, Y. H.; Noh, Y. Y.; Kim, D. Y. *Adv*. *Funct*. *Mater*. **2015**, *25*, 1146–1156.
2. (a) Adam, W.; Harrer, H. M.; Nau, W. M.; Peters, K. *J. Org. Chem*. **1994**, *59*, 3786–3797. (b) Li, P.; Sisto, T. J.; Darzi, E. R.; Jasti, R. *Org*. *Lett*. **2014**, *16*, 182−185. (c) Jasti, R.; Bhattacharjee, J.; Neaton, J. B.; Bertozzi, C. R. *J. Am*. *Chem*. *Soc*. **2008**, *130*, 17646−17647.
3. (a) Stratmann, R. E.; Scuseria, G. E.; Frisch, M. J. *J. Chem*. *Phys*. **1998**, *109*, 8218−8224. (b) Becke, A. D. *J. Chem*. *Phys*. **1993**, *98*, 5648−5652. (c) Lee, C.; Yang, W.; Parr, R. G. *Phys*. *Rev*. *B*: *Condens*. *Matter Mater*. *Phys*. **1988**, *37*, 785−789.
4. (a) Suenobu, T.; Arahori, I.; Nakayama, K. I.; Suzuki, T.; Katoh, R.; Nakagawa, T. *J. Phys*. *Chem*. *A* **2020**, *124*, 46−55. (b) Tanaka, F.; Tsumura, K.; Furuta, T.; Iwamoto, K.; Okamoto, M. *Photochem*. *Photobiol*. *Sci*. **2008**, *7*, 56−62.
5. (a) Evans, P. J.; Darzi, E. R.; Jasti, R. *Nat*. *Chem*. **2014**, *6*, 404−408. (b) Kayahara, E.; Patel, V. K.; Yamago, S. *J. Am*. *Chem*. *Soc*. **2014**, *136*, 2284−2287. (c) Xia, J.; Jasti, R. *Angew*. *Chem*. *Int*. *Ed*. **2012**, *51*, 2474−2476.
6. Adam, W.; Nau, W. M.; Fragale, G.; Wirz, J.; Klapstein, D. *J. Am*. *Chem*. *Soc*. **1995**, *117*, 12578−12592.
7. Nakagawa, T.; Okamoto, K.; Hanada, H.; Katoh, R. *Opt*. *Lett*. **2016**, *41*, 1498−1501.
8. Abe, M. *Chem*. *Rev*. **2013**, *113*, 7011−7088.
9. (a) Adam, W.; Kita, F.; Harrer, H. M.; Nau, W. M.; Zipf, R. *J. Org. Chem*. **1996**, *61*, 7056−7065. (b) Adam, W.; Van. Barneveld, C.; Emmert, O. *J. Chem*. *Soc*. *Perkin Trans*. *2* **2000**, No. 4, 637−641.
10. (a) Neese, F. *Wiley Interdiscip*. *Rev*.: *Comput*. *Mol*. *Sci*. **2012**, *2*, 73−78. (b) Neese, F. *Wiley Interdiscip*. *Rev*.: *Comput*. *Mol*. *Sci*. **2018**, *8*, 4−9.
11. Adam, W.; Maas, W.; Nau, W. M. *J. Org. Chem*. **2000**, *65*, 8790−8796.
12. Bleaney, B.; Bowers, K.D. *Proc*. *R*. *Soc*. *A* **1952**, *43*, 372−374.
13. (a) Yanai, T.; Tew, D. P.; Handy, N. C. *Chem*. *Phys*. *Lett*. **2004**, *393*, 51−57. (b) Yamaguchi, K.; Jensen, F.; Dorigo, A.; Houk, K. N. *Chem*. *Phys*. *Lett*. **1988**, *149*, 537−542.
14. (a) Hegarty, D.; Robb, M. A. *Mol*. *Phys*. **1979**, *38*, 1795−1812. (b) Andersson, K. *Theor*. *Chim*. *Acta* **1995**, *91*, 31−46.
15. (a) Abe, M.; Ye, J.; Mishima, M. *Chem*. *Soc*. *Rev*. **2012**, *41*, 3808−3820. (b) Abe, M.; Kawanami, S.; Ishihara, C.; Nojima, M. *J. Org*. *Chem*. **2004**, *69*, 5622−5626. (c) Hoffmann, R. *Acc*. *Chem*. *Res*. **1971**, *4*, 1−9. (d) Hoffmann, R. *J. Am*. *Chem*. *Soc*. **1968**, *90*, 1475−1485. (e) Abe, M.; Ishihara, C.; Nojima, M. *J. Org*. *Chem*. **2003**, *68*, 1618−1621. (f) Abe, M.; Ishihara, C.; Tagegami, A. *J. Org*. *Chem*. **2004**, *69*, 7250−7255. (g) Borden, W. T. *Chem*. *Commun*. **1998**, No. 18, 1919−1925.
16. Segawa, Y.; Omachi, H.; Itami, K. *Org*. *Lett*. **2010**, *12*, 2262−2265.
17. (a) Rickhaus, M.; Jirasek, M.; Tejerina, L.; Gotfredsen, H.; Peeks, M. D.; Haver, R.; Jiang, H. W.; Claridge, T. D. W.; Anderson, H. L. *Nat*. *Chem*. **2020**, *12*, 236−241. (b) Peeks, M. D.; Gong, J. Q.; McLoughlin, K.; Kobatake, T.; Haver, R.; Herz, L. M.; Anderson, H. L. *J. Phys*. *Chem*. *Lett*. **2019**, *10*, 2017−2022. (c) Schleyer, P. v. R.; Jiao, H.; Hommes, N. J. R. v. E.; Malkin, V. G.; Malkina, O. L. *J. Am*. *Chem*. *Soc*. **1997**, *119*, 12669−12670. (d) Burley, G. A. *Angew*. *Chem*., *Int*. *Ed*. **2005**, 3176−3178. (e) Toriumi, N.; Muranaka, A.; Kayahara, E.; Yamago, S.; Uchiyama, M. *J. Am*. *Chem*. *Soc*. **2015**, *137*, 82−85.
18. (a) Schleyer, P. v. R.; Maerker, C.; Dransfeld, A.; Jiao, H.; van Eikema Hommes, N. J. R. *J. Am*. *Chem*. *Soc*. **1996**, *118*,

6317−6318. (b) Steiner, E.; Fowler, P. W.; Jenneskens, L. W. *Angew*. *Chem*. *Int*. *Ed*. **2001**, *40*, 362−366. (c) Fallah-Bagher-Shaidaei, H.; Wannere, C. S.; Corminboeuf, C.; Puchta, R.; Schleyer, P. V. R. *Org*. *Lett*. **2006**, *8*, 863−866.

19. (a) Williams, R. V. *Chem*. *Rev*. **2001**, *101*, 1185−1204. (b) Winstein, S.; Sonnenberg, J.; Devries, L. *J*. *Am*. *Chem*. *Soc*. **1959**, *81*, 6524−6525.

20. Geuenich, D.; Hess, K.; Köhler, F.; Herges, R. *Chem*. *Rev*. **2005**, *105*, 3758−3772.

Acknowledgement of this chapter.

Mass spectrometry measurements were performed at the Natural Science Center for Basic Research and Development (N-BARD) of Hiroshima University. This work was supported by JSPS KAKENHI Grant Numbers 17H03022 (Manabu Abe), 20K21197 (Manabu Abe), and 16H06352 (Shigeru.Yamago), JST-CREST (Grant Number JPMJCR18R4), and was also supported by the International Collaborative Research Program of Institute for Chemical Research, Kyoto University (grant 2020-43). We thank UNISOKU Co., Ltd., for the use of the picosecond laser system (picoTAS).

Chapter 3. Generation and Characterization of a Tetraradical Embedded in a Curved Cyclic Paraphenylene Unit

Section 3.1: Introduction to this paper.

In the previous section, the existence of unique in-plane aromaticity due to quinoid structure and homoconjugation was suggested in diradical with small ring size (Figure 3.1a). In particular, the quinoid properties at four benzene rings are of interest because they cannot be constructed in linear systems. But the synthesis of smaller ring-size macrocyclic azo compounds was very difficult and could not be achieved yet. So, extending to tetradiradical, we designed **2DR-8CPP**, in which the two diradical units are bridged by four benzene rings each (Figure 3.1b). As with the previous macrocyclic molecules, we expected the generation of the quinoidal properties at the four benzene rings by the bonding interaction between diradical and diradicality induced by the ring structure. Also, the number of π-electrons in the entire ring of **2DR-8CPP** is 36, resulting in an anti-aromatic property in the 4nπ system. Therefore, it will be interesting to find out if quinoid properties occur in the entire ring even though it is anti-aromatic or only in one side. In order to investigate what kind of properties and spin states they exhibit, we initiated the synthesis of macrocyclic azo molecules **2AZ-8CPP** as tetraradical **2DR-8CPP** precursors.

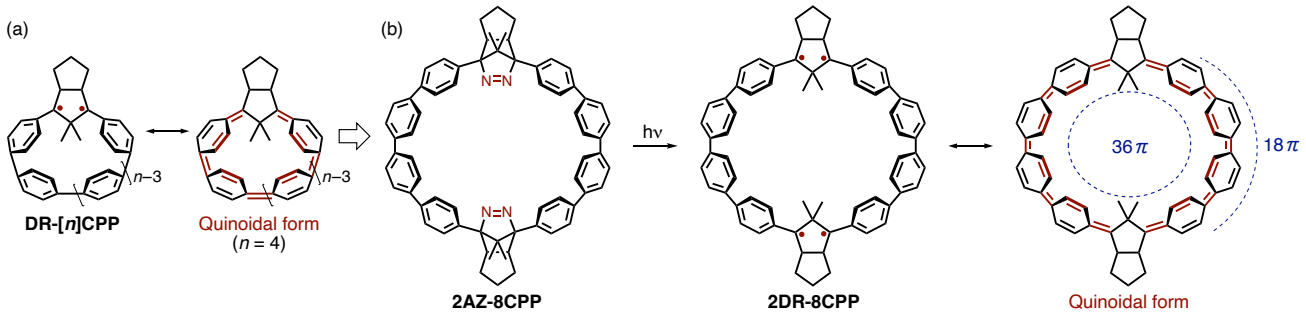

Figure 3.1: (a) The formation of quinoidal structure with expanded π-conjugated system by bonding interaction and macrocyclic effect. (b) The expectation of the formation of quinoidal structure of tetraradical **2DR-8CPP**.

Section 3.2: synthesis of macrocyclic azo compound **2AZ-8CPP**.

After some attempts, the compound **8** was synthesized by Suzuki-miyaura coupling reaction using compound **5** and mono-Bpin compound **7**, followed by Ni-catalyzed intramolecular cyclization of this precursor and reductive aromatization[(1)] afforded macrocyclic azo compound **2AZ-8CPP** with two azo units connected by four benzene rings at each side, in a total of 12 steps and an overall yield of 0.03% (Scheme 3.1).

Scheme 3.1: Synthesis of macrocyclic azo compound **2AZ-8CPP**. (a) 65°C: 16.5 h, 38 % yield. (b) 70°C: 1h + 3 h, 19 % yield. (c) r.t→65°C and 65°C for 13 h, 23 % yield.

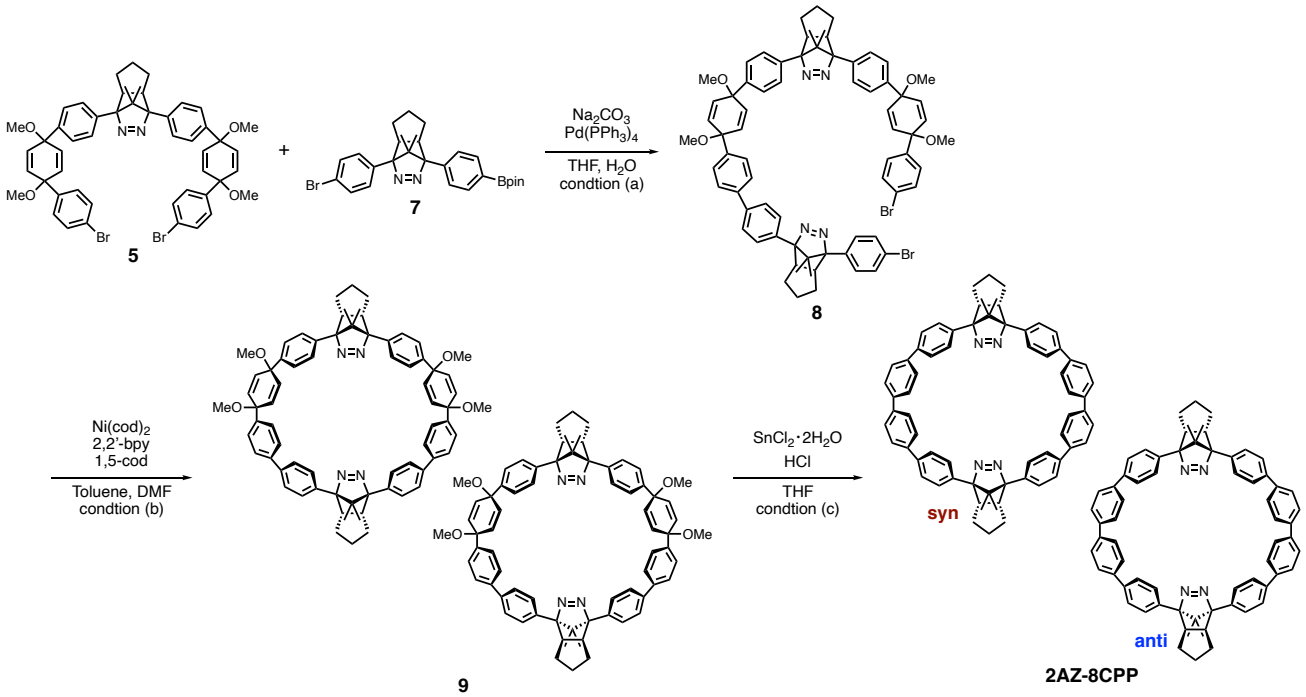

Section 3.3: The character of macrocyclic azo compound **2AZ-8CPP**.

There are two isomers present (syn and anti) depending on the direction of the cyclopentane ring, but it has been difficult to isolate them. But methyl signals in the azo units were observed separately in the ^{1}H NMR (700 MHz) and ^{13}C NMR (176 MHz) spectra, confirming the presence of two isomers (Figure 3.2a,b). Predicted the ^{13}C NMR chemical shifts of the four methyl carbons computed at DFT/RB3LYP/6-311+G(2d,p)//RB3LYP/6-31G(d) level of theory(2) is in good agreement with the experimentally observed values (Figure 3.2c). Methyl groups in the syn-conformer is appeared in the high magnetic region than those in the anti-conformer, which was also matched in the computations. Based on the integral ratio of the ^{1}H NMR signals of methyl groups, the ratio of the existence of the syn- and anti-conformer was estimated to be about 2 : 1. Single crystals were coincidentally prepared from the precipitate during the gradual evaporation at room temperature using a mixture solution of THF, and a small amount of 1,4-dioxane and cyclohexane and single crystal X-ray structure analysis was conducted (Figure 3.2d). Although the solvent molecule was disordered, the strained structure of the anti-conformer was confirmed with an average dihedral angle of 23.1° and a bend angle of the benzene rings of 17.7°.

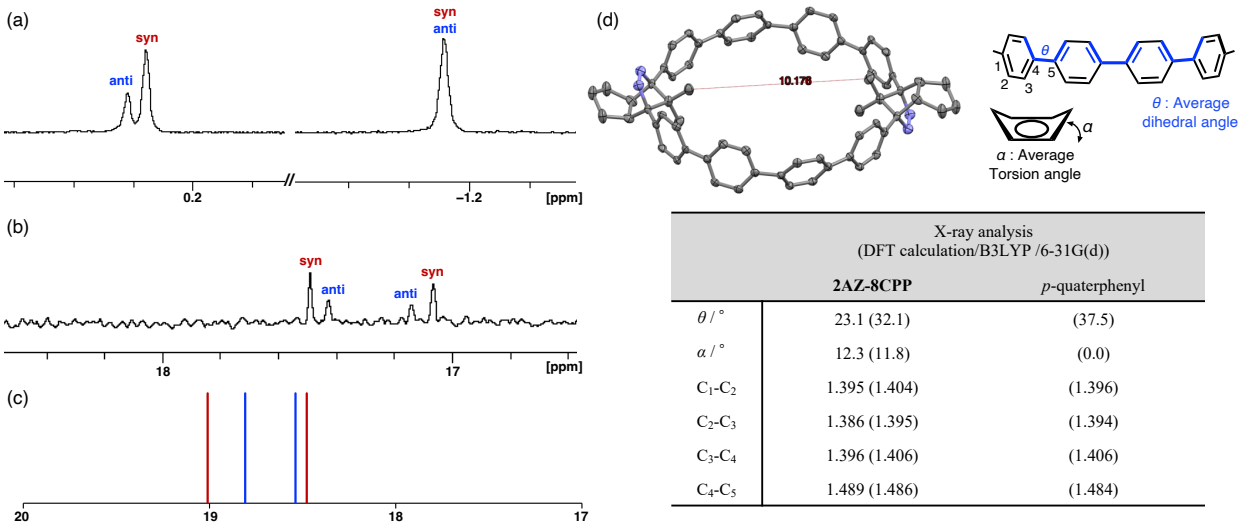

	X-ray analysis (DFT calculation/B3LYP /6-31G(d))	
	2AZ-8CPP	*p*-quaterphenyl
θ / °	23.1 (32.1)	(37.5)
α / °	12.3 (11.8)	(0.0)
C_1-C_2	1.395 (1.404)	(1.396)
C_2-C_3	1.386 (1.395)	(1.394)
C_3-C_4	1.396 (1.406)	(1.406)
C_4-C_5	1.489 (1.486)	(1.484)

Figure 3.2: (a) ^{1}H NMR spectrum (700 MHz) (upper, methyl groups at azo units: syn, −1.19 and 0.21 ppm; anti, −1.19 and 0.22 ppm). (b) ^{13}C NMR spectrum (176 MHz) (middle, methyl groups at azo units: syn, 17.06 and 17.48 ppm; anti, 17.14 and 17.42 ppm) in $CDCl_3$. (c) Chemical shifts of methyl carbons calculated at the B3LYP/6-311+G(2d,p) level (lower, C chemical shift of methyl groups: syn (red), 18.48 and 19.01 ppm; anti (blue), 18.54 and 18.81 ppm). (d) X-ray structure of anti-**2AZ-8CPP** with thermal ellipsoids at 50% probability (gray, carbon; blue, nitrogen). Hydrogen atoms and solvent molecules are omitted for clarity.

UV-visible absorption and emission measurements of **2AZ-8CPP** in benzene solution and TD-DFT calculations(3) at the RB3LYP/6-311G+(2d,p) level of theory have been conducted. A broad absorption at approximately 327 nm that corresponding to the HOMO−1−LUMO and HOMO−LUMO+1 transitions were found (Figure 3.3a,b). The HOMO−LUMO transition was forbidden because of the conserved symmetry of **2AZ-8CPP**. Also, the weak absorption of the n-π* transition originating from the azo chromophore could not be confirmed because it was hidden behind the strong

absorption band from the π-conjugated system. A structured fluorescence emission was observed for 330 nm excitation with peak wavelengths at 410 nm and the S_1 state energy was estimated to be about 76 kcal mol^{-1} (Figure 3.3c). The fluorescence quantum yields and lifetimes were determined to be 39 ± 1% and 1.2 ns, 34 ± 1% and 1.1 ns under nitrogen and air, respectively. No phosphorescence of **2AZ-8CPP** was observed even in the 2-MTHF matrix condition at 77 K. The triplet energy of **2AZ-8CPP** was computed to be 58.6 kcal mol^{-1} (syn) and 59.0 kcal mol^{-1} (anti) at the UM06-2x/6-31G(d) level of theory[4] and the energy difference with the S_1 and T_1 state was estimated to 17.4 kcal mol^{-1} (syn) and 17.0 kcal mol^{-1} (anti). These energies are smaller than that of the singlet oxygen energy ($^1\Delta_g$ = 22.5 kcal mol^{-1}), suggesting that the slight quenching of the fluorescence of **2AZ-8CPP** in the presence of oxygen was quenching of the S_1 state by $^3O_2$[5].

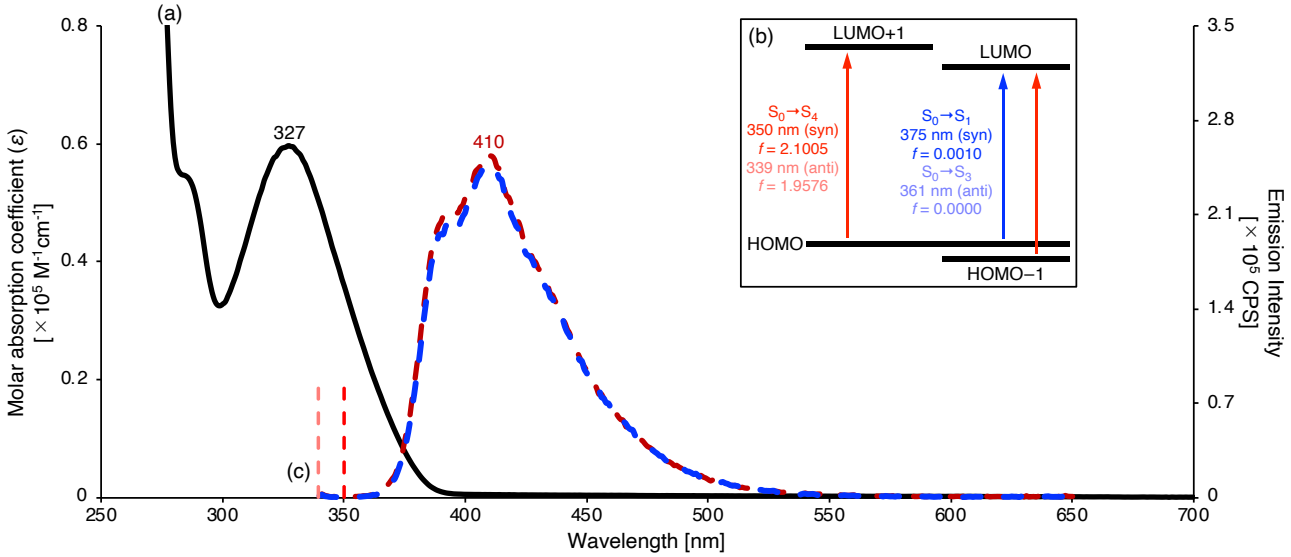

Figure 3.3: (a) UV-vis absorption spectrum and emission spectra of **2AZ-8CPP** in benzene solution. (b) Electronic transitions computed $S_0 \rightarrow S_1$ transition (blue, syn: λ_{calc} = 375 nm, f = 0.0010, anti: λ_{calc} = 361 nm, f = 0.0000) and $S_0 \rightarrow S_4$ transition (red and pink, syn: λ_{calc} = 350 nm, f = 2.1005, anti: λ_{calc} = 339 nm, f = 1.9576) at the TD-B3LYP/6-311G+(2d,p) level of theory. (c) Emission spectra for 330 nm excitation (Abs_{330} = 0.1) under an N_2 (red) and air (blue) atmosphere in benzene solution.

Section 3.4: Photolysis of azo compound **2AZ-8CPP**.

To confirm the photo-denitrogenation of **2AZ-8CPP,** the photoreaction of **2AZ-8CPP** in degassed C_6D_6 solution (0.9 mM) was monitored by ^{1}H NMR spectroscopy using a 365 nm LED light (Figure 3.4). During the irradiation, some new pairs of methyl groups originating from the photoreaction products were observed at the high magnetic field region (−1.37, 0.07, and 0.94 ppm). When the photolysis was continued, the new signals at the low magnetic field region (0.00, 0.04, and 0.90 ppm) gradually increased. Furthermore, these signals broadened as light irradiation was continued more, indicating that secondary photoreaction of the primary photoreaction product occurred to give a mixture. Identifying the photoreaction products by NMR analysis was difficult due to the existence of the isomer and some mixture. So, the photoreaction products were analyzed by HR mass spectrometry (p-ESI/MeOH)[7] after unsealing the NMR tube. The presence of products with $C_{68}H_{60}$ was confirmed, suggesting that double photo-denitrogenation of **2AZ-8CPP** occurred by the irradiation of the light. In addition, the presence of the oxygenated compound $C_{68}H_{60}O_4$ was observed, suggesting that the photoreaction products of **2AZ-8CPP** were O_2 reactive[6].

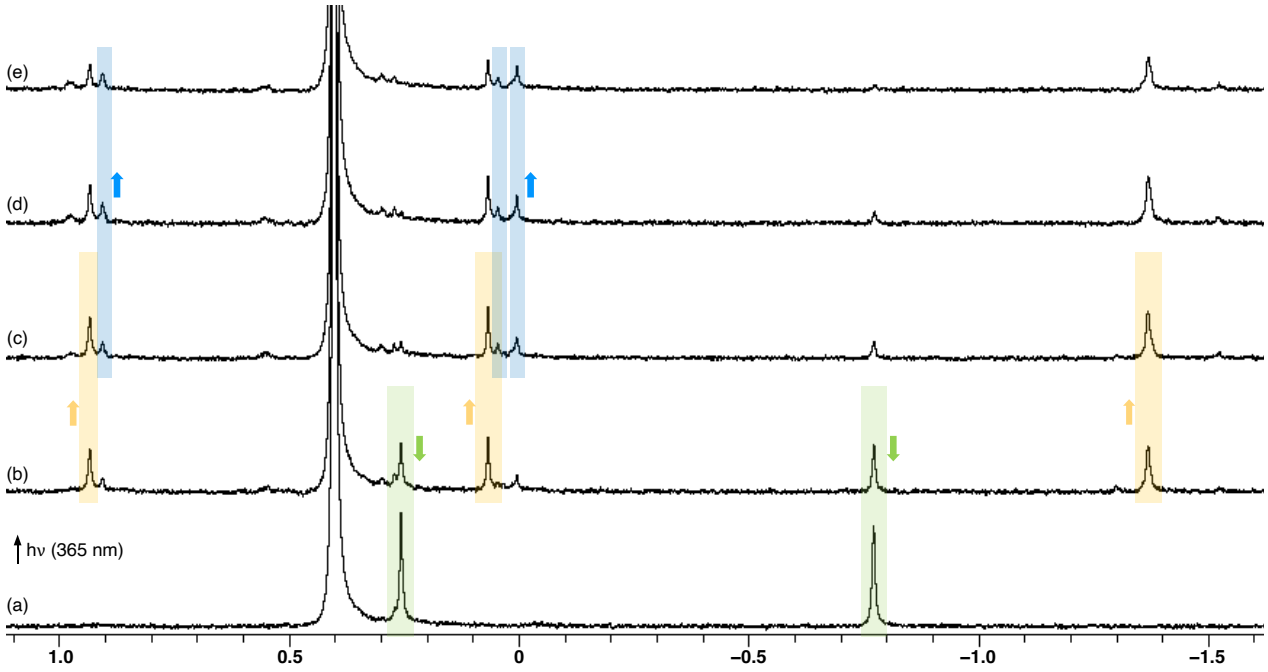

Figure 3.4: ^{1}H NMR analysis (400 MHz) of the photolysis of **2AZ-8CPP** (0.9 mM) by 365 nm LED light in degassed C_6D_6 solution: (a) before irradiation; (b) after 30 s irradiation; (c) after 60 s irradiation; (d) after 90 s irradiation; (e) after 180 s irradiation.

Section 3.5: Transient absorption measurement of macrocyclic azo compound **2AZ-8CPP**.

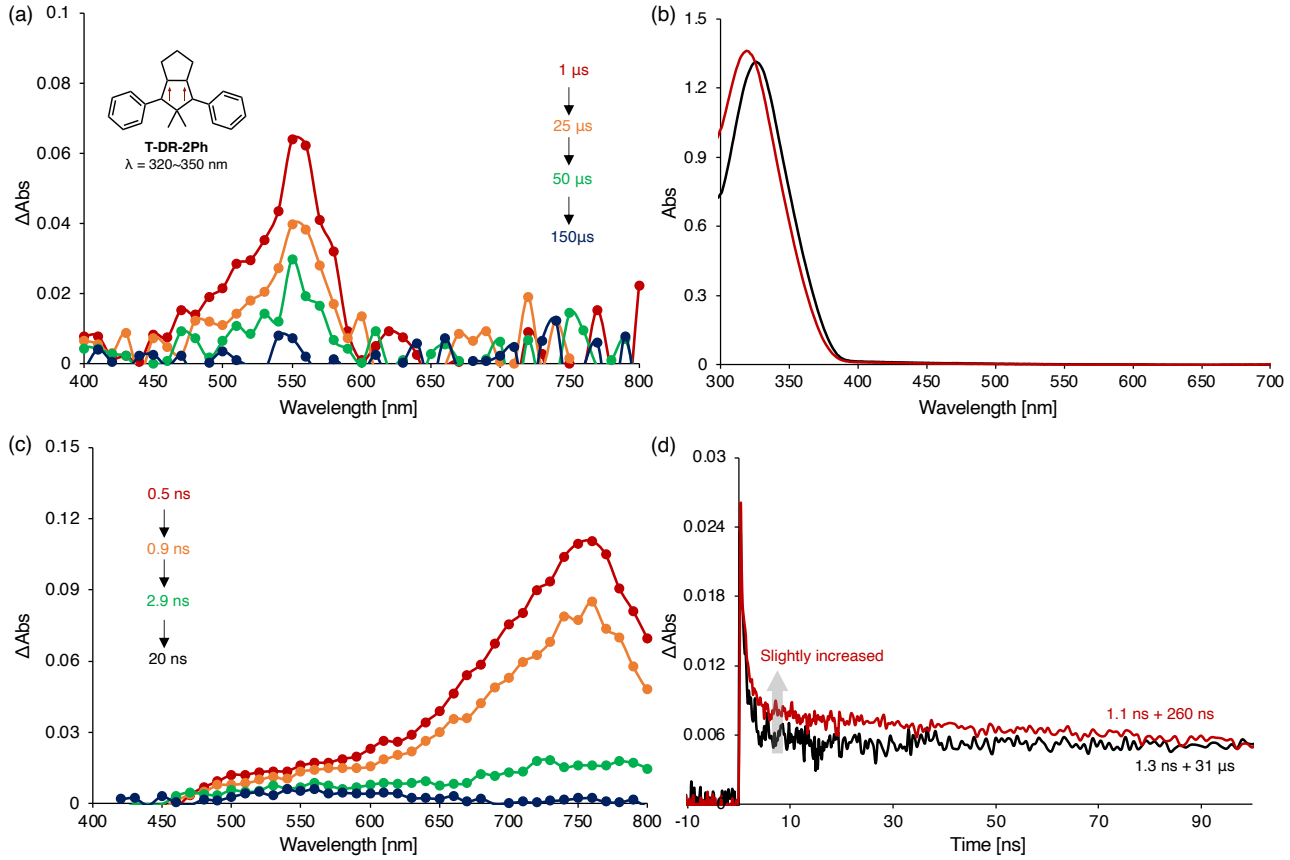

Figure 3.5: (a) Sub-microsecond time-resolved transient absorption spectra in benzene under N_2 atmosphere at 295 K. (b) UV-vis absorption spectra of the sample in benzene before (black) and after (red) measurement of sub-microsecond LFP. (c) Sub-nanosecond time-resolved transient absorption spectra in benzene under Ar atmosphere at 295 K. (d) Time profile at 570 nm in the sub-nanosecond time-resolved spectroscopic analysis in Ar (black) and air (red).

To detect the transient species generated by photo irradiation, sub-microsecond and sub-nanosecond transient absorption measurement were conducted in benzene solution at 295 K using laser flash photolysis (LFP) [(8)] and randomly interleaved pulse train (RIPT) method[(9)], respectively. Transient species with the lifetime $\tau = 31 \pm 1$ μs were observed with broad absorption at around 560 nm in the sub-microsecond TA analysis under N_2 atmosphere (Figure 3.5a). The lifetime of this transient species was dramatically shorted under air atmosphere ($\tau = 260 \pm 5$ ns), suggesting that this transient was triplet species. UV−vis absorption spectra of the sample before and after the TA measurements was different (Figure 3.5b), demonstrating that photo-denitrogenation of **2AZ-8CPP** might be occurred. So, HR-mass analysis (p-ESI/MeOH sol)[(7)] was conducted using the sample after LFP measurement and confirmed the presence of the product with $C_{68}H_{60}N_2$. The absorption of triplet 1,3-diphenylcyclopentane-1,3-diyl diradical **T-DR-2Ph** was reported to appear at approximately 320–350 nm[(10)], but the transient species with this absorption could not be identified due to the low generation of diradical, having the very short lifetime or overlapping the strong absorption of π-conjugated system. So, this transient species was assigned to the triplet excited state T_1 of π-conjugated system of para-phenylene moiety. The short-lived species ($\tau = 1.3 \pm 0.0$ ns under Ar and 1.1 ± 0.0 ns under air atmosphere, respectively) with a strong absorption maximum at ~ 750 nm was

observed in the sub-nanosecond TA spectroscopic analysis (Figure 3.5c). The lifetime was not changed in the presence of O_2 and nearly consistent with the fluorescence lifetime and assigned to the $S_1 \rightarrow S_n$ transition. Both the excited singlet and triplet states were simultaneously observed in the time profile at 570 nm (Figure 3.5d). Same as **AZ-6CPP** case, fluorescence quenching is due to enhance the intersystem crossing (ISC) from the S_1 to the T_1 state in the presence of $^3O_2$ was observed.

Section 3.6: EPR measurement of the photo-generated species of **2AZ-8CPP**.

To detect directly photo-generated species of **2AZ-8CPP**, EPR spectroscopic analysis was conducted. Low-temperature photolysis of **2AZ-8CPP** was conducted using an UV light at 20 K in degassed toluene matrix condition (0.1 mM). After photolysis for 1 h, EPR signals with zero-field splitting (zfs) parameters of $|D/hc| = 0.045$ cm^{-1} and $|E/hc| \leq 0.001$ cm^{-1} was observed (Figure 3.6a). The quintet state of the tetraradical **2DR-8CPP** with zero-field splitting (zfs) parameters of $|D/hc| = 0.012$ cm^{-1} (syn) and 0.014 cm^{-1} (anti) computed at the (RO)BP/EPR-II/B3LYP/6-31G(d) level of theory using ORCA 4.2.1[11] was not detected when continued photolysis (Figure 3.6b). The ratio of the signal intensity of the half-field region ($\Delta M_S = \pm 2$) which is forbidden transition to that of the allowed transition ($\Delta M_S = \pm 1$) was much stronger than that observed in typical signals of triplet species. So, the simulated EPR signals could not be reproduced by a common line-shape model based on a convolution of Gaussian and Lorentzian functions. For $S \geq 1$ spin systems, line broadening is often explained by considering the distributions of D and E originating from local structural heterogeneities (strain)[12]. The unusual intensity ratio was reproduced well using a phenomenological D-strain model because the half-field resonance position was dominated by the g values. Because the macrocyclic compound had a rigid structure, the structural distribution was due to being frozen under the EPR measurement conditions before the most stable structure was taken.

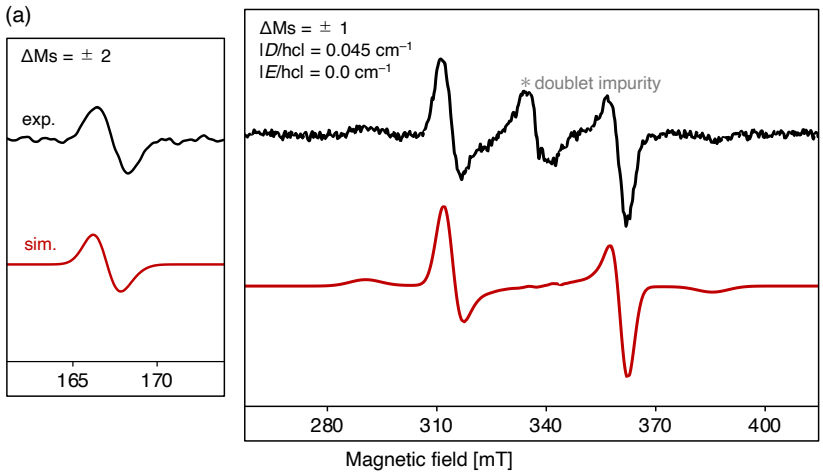

(b)

Compound	Spin, conformer	$\|D/hc\|/\|E/hc\|$ [cm^{-1}]
Diradical	Triplet, syn	0.041/0.007
	Triplet, anti	0.037/0.002
Tetraradical	Quintet, syn	0.012/< 0.001
	Quintet, anti	0.014/< 0.001

Figure 3.6: (a) EPR spectrum of the photolysis of **2AZ-8CPP** (0.1 mM) using a UV lamp (>250 nm) in 2-MTHF matrix at 20 K (black) and simulated EPR spectrum (red). (b) Computed zfs parameters (D and E) for triplet diradicals and quintet tetraradicals at the (RO)BP/EPR-II//UB3LYP/6-31G(d).

To determine the spin state of the multiradical, 2D-pulsed EPR measurement[13] was conducted in a toluene matrix (0.1 mM) condition. In this method, the spin state of the multiradical can be determined from the value of the nutation frequencies ω_n in the 2D pulsed EPR spectra using the following equation.

$$\omega_n = [S(S+1) - Ms(Ms-1)]^{1/2}\omega_1$$

S : Spin quantum number, Ms : Magnetic moment

Triplet species : $\sqrt{2}\omega_1$

The measurements were conducted after photolysis for 10 h by UV light at 20 K. A triplet species with a nutation frequency of 19.4 MHz was observed (Figure 3.7). The EPR signal at around 330 mT originated from a doublet species with a nutation frequency of $\omega_1 = 14$ MHz. A high-spin state such as a quintet state with a large nutation frequency was not

observed, suggesting that only triplet species existed by photolysis.

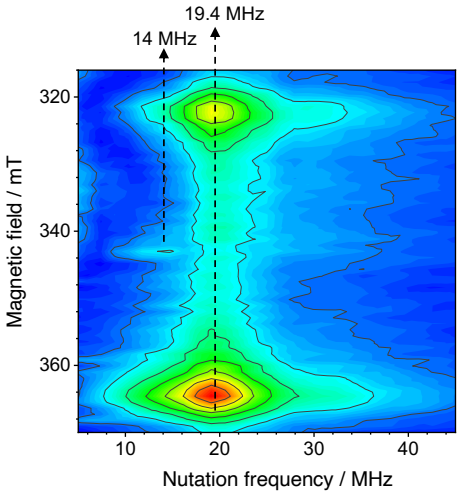

Figure 3.7: 2D-pulsed EPR signal at 20 K after photolysis of **2AZ-8CPP** for 10 h in toluene matrix (0.1 mM) using UV light under vacuum condition.

Section 3.7: Theoretical calculation.

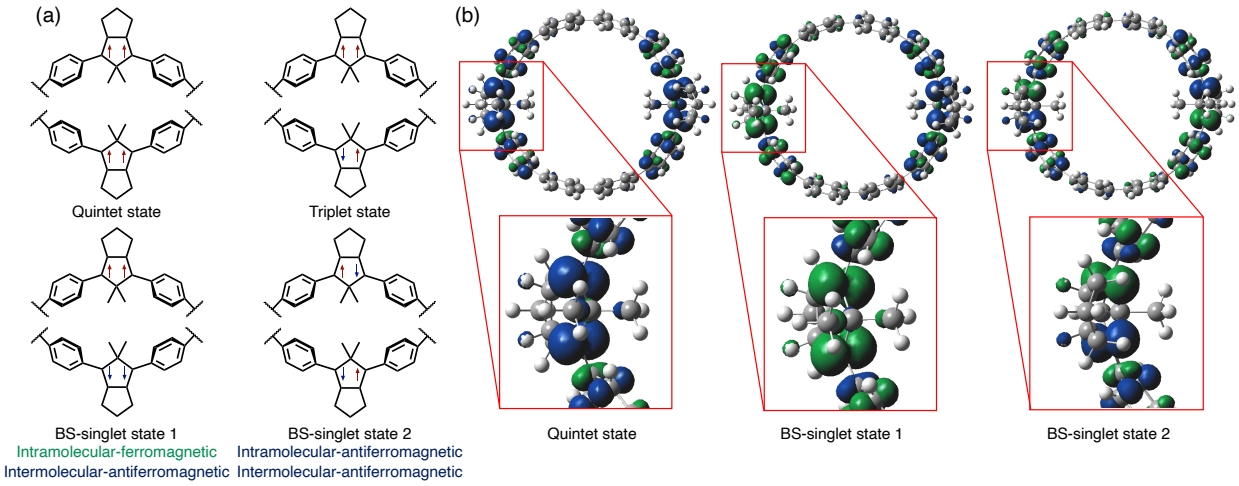

Figure 3.8: (a) Illustrations of spin state in the quintet, triplet, and broken symmetry (BS)-singlet states. (b) Calculated spin density distributions (isovalue = 0.005) of spin state in the quintet and BS-singlet states.

The quintet, triplet, and singlet states of **2DR-8CPP** were computed at the CAM-B3LYP/6-31G(d) level of theory using the Gaussian 16 rev. B01 program to estimate the ground spin state. Open-singlet is ground state for syn-conformer, while quintet is that for anti-conformer. However, the S^2 value is far from the theoretical value, suggesting that the effect of spin contamination is significant. In order to remove the effect of spin contamination, the Yamaguchi equation[14] with approximate spin projection method[15] is applied to investigate the most stable spins among quintet, triplet, and singlet states without spin contamination error with the cooperation of Professor Kitagawa at Osaka University. Tetraradical **2DR-8CPP** has two diradical units, so the combination of ferromagnetic and antiferromagnetic coupling between the intra- and intermolecular interactions should be considered (Figure 3.8a). Two alignments in the singlet state, intramolecular-ferromagnetic/intermolecular-antiferromagnetic and intramolecular-antiferromagnetic/intermolecular-antiferromagnetic were constructed and denoted as BS-singlet state 1 and BS-singlet state 2, respectively. Because the triplet state could not be represented by a single determinant and thus necessitated a multireference calculation method, we focused on the quintet and singlet states. The orbital-averaged spin coupling parameter (J) was obtained from the calculated energies by applying the Ising Hamiltonian, and the energy gap between the singlet and triplet states (S−T gap: $2J$). All calculations were conducted in both gas phase and THF solution. Optimization of the structure of each spin state was computed at first at the B3LYP/6-31G(d) level using the Gaussian 09 rev. D01 program. The optimized structures in THF solution and the gas phase were almost the same. A nearly circular structure was found in the closed-shell singlet state, whereas an elliptical structure was formed in the quintet state. The loss of planarity at the diradical unit in an open-shell structure was affected this formation. On the other hand, the quintet and BS-singlet states were not significantly different, indicating that the open-shell character of the diradical unit largely contributed to the ring skeleton. The spin density distributions of the quintet, BS-singlet 1, and BS-singlet 2 states were calculated using the optimized structure (Figure 3.8b). In all models, the spin density was located mainly in the diradical unit and phenyl rings on both sides. The spin densities in the diradical units were ferromagnetic in the quintet and BS-singlet 1 states and antiferromagnetic in the BS-singlet 2 state, although their distributions were not different. The ground spin state was estimated by comparing the total energies of the optimized

structures (Table 3.1). Both BS-singlet states were slightly more stable than the quintet state, indicating that the ground spin state of **2DR-8CPP** is a singlet. The closed-shell singlet state became unstable above 20 kcal mol^{-1}, indicating the significant effect of static electron correlation. Moreover, the energy of BS-singlet state 1 was lower than that of BS-singlet state 2 by 0.25 kcal mol^{-1} and no difference in relative stability due to the difference in chemical environment was observed.

Table 3.1: Relative energies of the optimized singlet states to that of the quintet state in THF solvent. Gas-phase values are also provided in parenthesis. Approximate spin-projected values for BS-singlet states are provided in square brackets.

	Spin state			
	Quintet	BS-singlet 1	BS-singlet 2	R-singlet
Relative Energy [kcal mol^{-1}]	0.00 (0.00)	−0.39 (−0.35) [−0.61]	−0.14 (−0.13) [−0.22]	+24.9 (+25.7)

Spin contamination error was included in the BS-open-shell singlet states[16]. To remove spin contamination error, one diradical unit in BS-singlet state 1 was regarded as spin S=1, and the spin projection method was applied for the magnetic interaction between the diradical units by assuming a two-spin Heisenberg model[15]. The relative energies of BS-singlet states 1 and 2 are slightly lowered upon removal of spin contamination using the Yamaguchi equation (−0.61 kcal mol^{-1} and −0.22 kcal mol^{-1}, respectively), indicating that spin contamination error cannot be ignored. The energy of BS-singlet state 2 was also expected to contain spin contamination error. However, the spin projection method cannot be applied because the two-site Heisenberg model is not strictly applicable to BS-singlet state 2. The energy excluding the spin contamination error was estimated to be stable at 0.08 kcal mol^{-1} if the magnetic interaction between the two diradical units can be ignored. Because spin contamination sometimes strongly affects even the optimized structure of an open-shell singlet[14], we also determined its effect by applying the approximate spin-projected optimization method. The optimized structure of BS-singlet state 1 was almost same before using the spin projection method, and the relative energy was almost unchanged at −0.61 kcal mol^{-1}. While the structure of BS-singlet state 2 changed very slightly, and the relative energy changed to −0.23 kcal mol^{-1} (Table 3.1). The discussion of details is difficult because the magnetic interaction between the two diradical units is presumably negligible in BS-singlet state 2. However, the structures of the quintet and BS-singlet 1 states are almost identical, whereas that of the BS- singlet 2 state is slightly different. In other words, the spin interactions in the diradical units of the quintet and BS-singlet 1 states are ferromagnetic, whereas that of the BS-singlet 2 state is antiferromagnetic, suggesting that the degree of curvature of the diradical unit is slightly different between the ferromagnetic and antiferromagnetic coupling states.

Finally, the magnetic interactions in the diradical unit (J_{intra}) and between the diradical units (J_{inter}) were estimated in the THF solution. J_{intra} was ferromagnetic (+0.16 kcal mol^{-1}) and J_{inter} was antiferromagnetic ferromagnetic (−0.21 kcal mol^{-1}). The energy levels of quintet, triple, and singlet were estimated from the J values. The ground spin state was determined to open-singlet state (Figure 3.9).

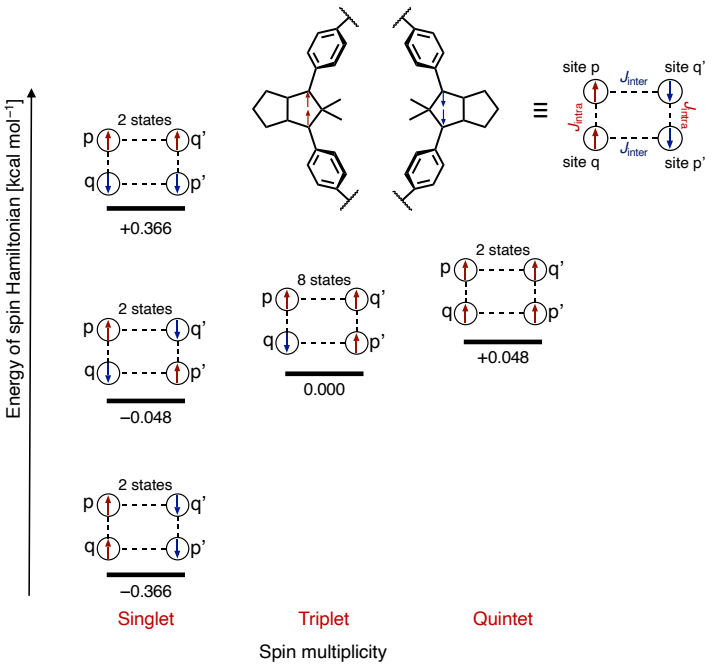

Figure 3.9: Energy diagram based on the calculated intra-(J_{intra} = +0.16 kcal mol^{-1}) and inter-(J_{inter} = −0.21 kcal mol^{-1}) molecular magnetic interactions.

Section 3.8: Various-temperature (VT)-EPR measurement of the photo-generated species of **2AZ-8CPP**.

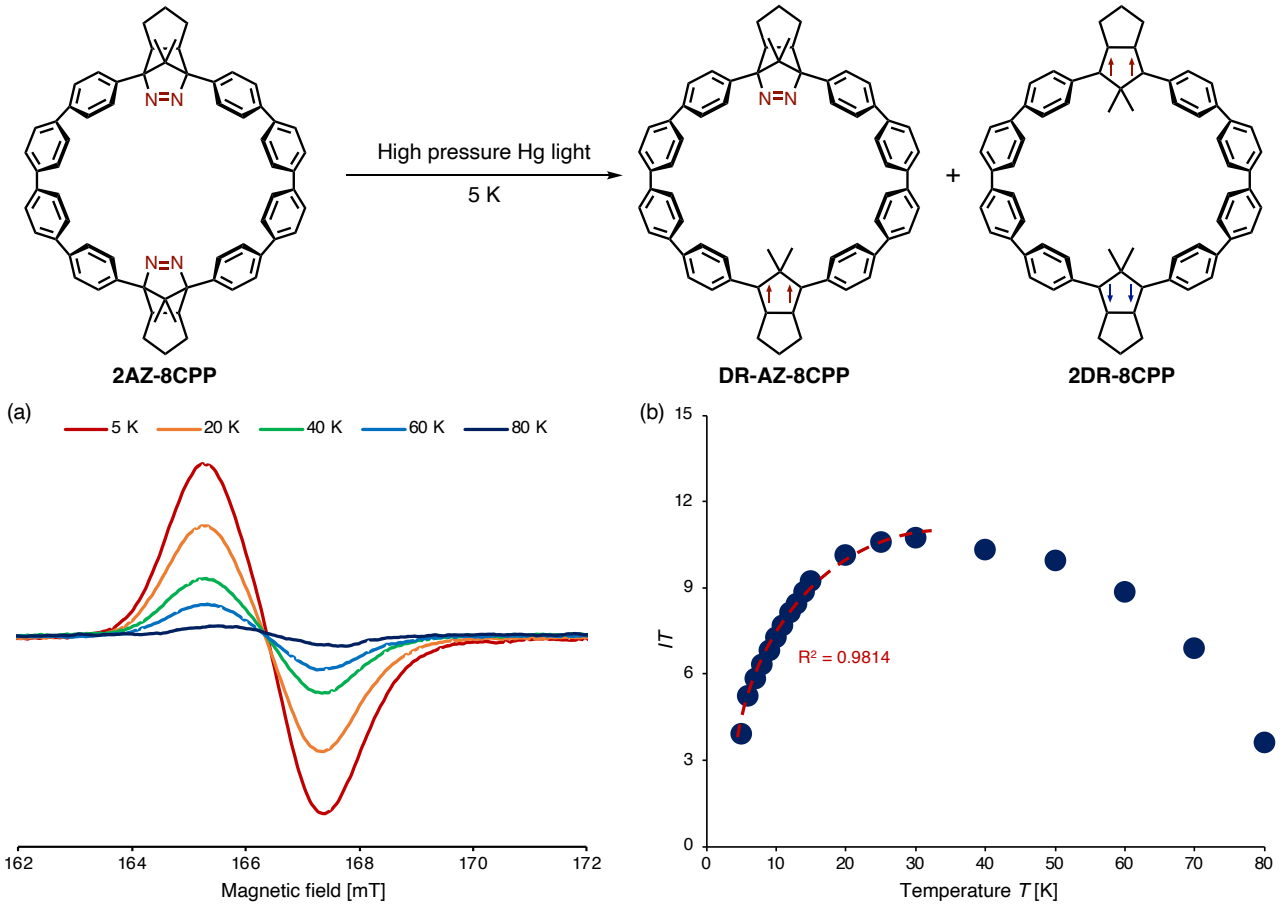

Figure 3.10: (a) Temperature dependence of the signal intensity at the half-field region after photolysis of **2AZ-8CPP** using high pressure Hg light in a 2-MTHF matrix. (b) Signal intensity I × Temperature T vs Temperature T (IT-T) plot and least-squares fit for the Bleaney−Bowers analysis.

To investigate more information about the behavior of multiradical generated by the photolysis of **2AZ-8CPP**, VT-EPR measurements was conducted. After 2 h of photolysis at 5 K by a high-pressure Hg light, EPR signal stemming from persistent triplet species was observed at the half-field region (~165 mT). At first, the dependence of the signal intensity to a microwave power was investigated at 5 K and the maximum power of the measurement is determined to 0.63 mW, for which saturation of the EPR signal was not observed even at 5 K. As the temperature gradually increased, a decrease in the EPR signal intensity at about 165 mT was observed (Figure 3.10a). In the signal intensity I × temperature T vs Temperature T (IT-T) plot using the value below 30 K, the IT value gradually increased with increasing temperature, indicating that the triplet state is thermally populated as an excited state. As observed for **DR-6CPP,** thermal reactivity was confirmed by the behavior that the EPR signal intensity at 5 K was not recovered after warming the EPR sample to 40 K. From the least-squares fit for the Bleaney−Bowers analysis[17] using the values from 5 K to 30 K, singlet and triplet energy gap ΔE_{S-T} was determined to be −23 ± 1 cal mol^{-1}, demonstrating the singlet ground state (Figure 3.10b). But this value was smaller than the calculated ΔE_{S-T} energy gap in the tetraradical species. There is the possibility of the three paramagnetic species, namely the triplet states of **DR-AZ-8CPP** and triplet and quintet state of **2DR-8CPP** may be detected by the EPR measurements. When the case of **2DR-8CPP**, the singlet state was expected to have a large population because it was computed to have

the singlet ground state. On the other hand, mono-denitoroganated compound **DR-AZ-8CPP**, *J* value in the diradical unit (J_{intra}) was estimated to the plus value, suggesting that **DR-AZ-8CPP** was predicted to have the triplet ground state. The EPR signal of the triplet state of **2DR-8CPP** might overlap with that of **DR-AZ-8CPP**. The experimentally determined small ΔE_{S-T} value was due to the generation of a mixture of **DR-AZ-8CPP** having a triplet ground state and **2DR-8CPP** having a singlet ground state. The distribution of the singlet, triplet, and quintet states was estimated by the results of the computed energy gaps of tetraradical **2DR-8CPP** (Figure 3.11). The population of the quintet state was almost negligible at 20 K, although a small amount of the triplet state was present, suggesting that detection of only the triplet species in the EPR analysis of **2DR-8CPP** is reasonable. The distribution of the quintet state could be augmented by increasing the temperature (population ≈ 0.001 at 30 K), but the decomposition of multiradical above 30 K hindered the observation of the quintet state.

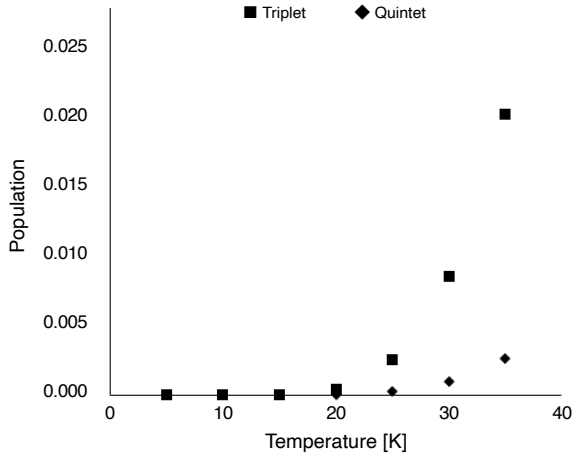

Figure 3.11: Simulated populations of the triplet and quintet states using the Boltzmann distribution.

Section 3.9: Summary of this chapter.

In this chapter, focusing on the behavior, reactivity, and spin–spin interaction of tetraradical embedded in the CPP structure and synthesize **2AZ-8CPP** with two isomers. The singlet and triplet excited states of the π-conjugated system at paraphenylene moiety were detected by transient absorption spectroscopy. Persistent triplet species were observed by the EPR measurements at 20 K after the photolysis of **2AZ-8CPP** in the matrix conditions. The quintet state of **2DR-8CPP** was not observed under the EPR measurement conditions because of its negligible population. Spin–spin interaction in **2DR-8CPP** within the curved CPP skeleton revealed by theoretical calculation. The magnetic interactions in the diradical unit (J_{intra}) and between the diradical units (J_{inter}) were found to the ferromagnetic and antiferromagnetic, respectively, and ground spin state of tetraradical was determined to singlet.

Section 3.10: Experimental section.

Section 3.10.1: General Information.

Reagents and solvents

All commercially available reagents were purchased from TCI, Wako, Oakwood Chemical and BLD Pharmatech and were used without further purification. Dry toluene for synthesis was obtained by distillation over CaH_2. Dry-DMF was purchased from Wako. 2-methyl tetrahydrofuran for EPR measurement was obtained by distillation over CaH_2 and Na. Dry solvents for spectroscopy analysis were purchased from commercial suppliers.

Procedure

All workup and purification procedures were performed with reagent-grade solvents in the air. Thin-layer chromatography (TLC) analyses were performed using commercial aluminum sheets of Merck silica gel 60 F_{254} and visualized with an ultraviolet lamp (λ = 254 nm). Column chromatography was performed with silica gel 60N (spherical, neutral, 63-210 μm, Kanto). Recycling chromatographic separation in GPC were performed by LC-9210, Japan Analytical Industry Co., Ltd. with chloroform as mobile phase.

Measurements

NMR spectra were recorded on a Bruker Ascend 400 (^{1}H NMR : 400 MHz, ^{13}C NMR : 100 MHz) and AVANCE NEO 700 (^{1}H NMR : 700 MHz, ^{13}C NMR : 176 MHz) spectrometer and referenced to residual solvent peak. Coupling constants (*J*) are denoted in Hz and chemical shifts (δ) in ppm. The abbreviations s, d, t, dd, dt, td and m stand for the resonance multiplicities singlet, doublet, triplet, doublet of doublets, doublet of triplets, triplet of doublets and multiplet, respectively. The X-ray diffraction data of the single crystals were collected on a Bruker APEX-II Ultra CCD diffractometer. The structures were solved using direct methods and refined by full-matrix least-squares techniques using the SHELX program package. Single crystal X-ray structure was visualized by Mercury (CCDC). A will-V (ARK TECH) or CL-1501 (ASAHI SPECTRA) was used for 365 nm LED light source. UV-vis spectra were recorded on a SHIMADZU UV-3600 Plus spectrometer. The spectra were collected at room temperature using a slit width of 1 nm with middle scan rate. IR spectrum was recorded on a JASCO MCT-6000M. The date of High-resolution Mass spectrometry (HRMS) was measured with Thermo Fisher Scientific LTQ Orbitrap XL using electrospray ionization (ESI) or atmospheric-pressure chemical ionization (APCI) method. Steady-state fluorescence spectra were recorded with a FluoroMax 4 spectroflurometer Horiba Yobin Yvon using a slit width of 1 nm. Fluorescence lifetime was measured by using FluoroHub-B, TemPro 01, TBX, and 373 nm NanoLED light (HORIBA). The excitation source for sub- microsecond laser flash photolysis (LFP) was a tunable Nd:YAG minilite laser at 355 nm. The monitoring system consisted of a 150 W Xenon arc lamp as light source, a Unisoku MD200 monochromator detection and a photomultiplier. The temperature was controlled by Unisoku CoolSpek USP- 203-B. Sub-nanosecond transient absorption measurements were conducted with Unisoku PicoTAS system in 2 mm cuvette. The excitation source was a passive Q-SWITCH microchip laser at 355 nm. Cw-EPR spectra were recorded on Bruker BioSpin ELEXSYS E500 spectrometer at Hiroshima university and Bruker BioSpin ELEXSYS E600 spectrometer at Osaka Metropolitan University. 2D-pulse EPR spectra were recorded on Bruker ESP380 E at Osaka Metropolitan University. SUPERCURE-351S (SAN-EI) was used for UV light source. Simulation of EPR signal was conducted by Easyspin (open-source MATLAB toolbox).

Section 3.10.2: Synthesis and spectral data.

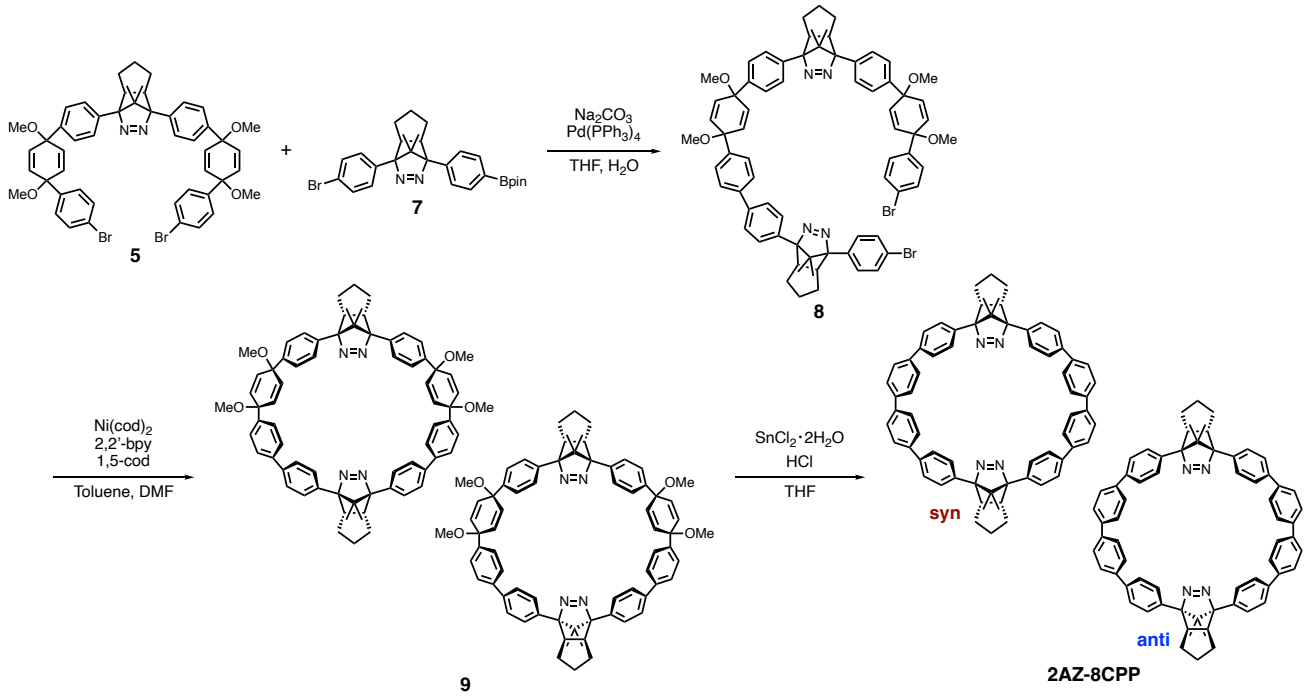

Synthesis of compound **8**.

Under nitrogen atmosphere, **5** (555 mg, 0.61 mmol), **7** (126 mg, 0.24 mmol), Na_2CO_3 (69 mg, 0.65 mmol), and $Pd(PPh_3)_4$ (19 mg, 0.02 mmol) were dissolved in THF (8 mL) and H_2O (1 mL). The reaction flask was replaced with nitrogen atmosphere after freeze pump thaw cycling (three times). The mixture was stirred at 65°C for 16.5 h (overnight). The reaction was quenched by the addition of NH_4Claq. The organic layer was extracted with EtOAc two times, washed with brine, and dried over Na_2SO_4. After filtration, the solvent was removed under reduced pressure. The crude mixture was purified by silica gel column chromatography to give **8** (113 mg, 0.09 mmol) in 38 % yield. This reaction was repeated several times. **^{1}H NMR** ($CDCl_3$, 400 MHz) δ 0.12 (s, 3H), 0.19 (s, 3H), 0.92 (s, 3H), 1.00 (s, 3H), 1.41–1.45 (m, 2H), 1.55–1.59 (m, overlap with water, 10H), 3.44–3.57 (s and m, 12H and 4H), 6.07–6.20 (m, 8H), 7.29–7.31 (d, J = 8.7 Hz, 2H), 7.42–7.48 (d, J = 8.6 and 8.5 Hz, 4H), 7.53–7.55 (dd, J = 8.5 Hz, J = 1.3 and 1.4 Hz, 4H), 7.60–7.70 (m, 12H), 7.78–7.80 (d, J = 8.4 Hz, 2H). **^{13}C NMR** ($CDCl_3$, 100 MHz) δ 17.14, 17.17, 17.95, 18.02, 25.58, 25.67, 28.74, 49.01, 49.14, 49.25, 52.17, 52.22, 66.49, 74.69, 74.82, 74.91, 74.97, 97.98, 98.36, 98.42, 98.63, 121.75, 122.05, 126.04, 126.13, 126.68, 127.20, 127.27, 127.72, 127.76, 128.01, 128.06, 129.36, 131.69, 131.72, 133.18, 133.29, 133.48, 133.55, 133.75, 133.80, 133.86, 133.95, 135.20, 135.52, 135.67, 135.85, 140.19, 140.31, 142.73, 143.00. **HRMS** (p-ESI, MeOH sol) m/z: Calcd for $C_{72}H_{72}N_4O_4Br_2Na$ $[M + Na]^+$, 1237.38125, found 1237.38123. **IR** (KBr plate [cm^{-1}]) 537, 561, 664, 756, 774, 807, 821, 952, 1010, 1027, 1038, 1077, 1174, 1229, 1302, 1372, 1395, 1448, 1469, 1491, 1507, 2822, 2876, 2939, 3033.

Synthesis of compound **9**.

Under nitrogen atmosphere, 1,5-cyclooctadiene (0.1 mL, 0.80 mmol) and 2,2'-bipyridyl (121 mg, 0.77 mmol) were dissolved in dry-toluene (6 mL) and dry-DMF (6 mL). The reaction flask was replaced with argon atmosphere after freeze pump thaw cycling (four times). $Ni(cod)_2$ (235 mg, 0.85 mmol) was added, and replacement of argon atmosphere was conduct again. The mixture was stirred at 70°C for 30 min.

On the other hand, under nitrogen atmosphere, **8** (194 mg, 0.16 mmol) was dissolved in dry-toluene (30 mL). The reaction flask was replaced with argon atmosphere after freeze pump thaw cycling (four times). The solution of **8** was added to the Ni-catalyst solution for 1 h at 70°C. The mixture was stirred for 3 h, then cooled down to room temperature. The reaction mixture was added to 1 M HClaq and stirred for 15 min at room temperature. The organic layer was extracted with EtOAc two times, washed with 1 M HClaq and brine, and dried over Na_2SO_4. After filtration, the solvent was removed under reduced pressure. The crude mixture was purified by silica gel column chromatography (Hex : EtOAc = 6 : 1→ 5 : 1) to give **9** (31 mg, 0.03 mmol) in 19 % yield. **^{1}H NMR** ($CDCl_3$, 400 MHz) δ −0.78 and −0.68 (s, 3H), −0.09 and −0.05 (s, 3H), 0.49, 0.71, 0.76 (s, 6H), 1.48–1.50 (m, 6H), 1.74 (m, 4H), 1.88 (m, 2H), 3.43–3.49 (s and m, 12H and 2H), 3.61–3.65 (m, 2H), 5.79–5.85 (td, 2H), 6.10–6.29 (td, 6H), 7.30–7.36 (d, *J* = 8.4 Hz, 4H), 7.41–7.46 (d, *J* = 8.6 and 8.5 Hz, 4H), 7.54–7.56 (s and d, *J* = 8.1 Hz, 6H), 7.63–7.70 (d and m, *J* = 8.4 Hz, 10H). **^{13}C NMR** (CDCl3, 100 MHz) δ 17.11, 17.16, 17.51, 17.59, 18.13, 18.29, 25.62, 25.75, 28.61, 28.66, 29.34, 29.85, 47.85, 48.05, 48.40, 48.48, 52.02, 52.34, 52.35, 66.74, 66.83, 67.50, 67.63, 74.78, 75.01, 75.12, 75.17, 97.99, 98.11, 98.70, 98.76, 125.93, 125.95, 126.76, 127.44, 127.78, 127.84, 127.92, 131.27, 131.42, 131.52, 132.07, 135.06, 135.15, 135.22, 135.66, 135.84, 136.11, 140.02, 140.33, 140.61, 141.00, 142.34, 142.36, 142.97, 143.05. **HRMS** (p-ESI, MeOH sol) m/z: Calcd for $C_{72}H_{72}N_4O_4Na$ $[M + Na]^+$, 1079.54458, found 1079.54358. **IR** (KBr plate [cm^{-1}]) 544, 559, 665, 686, 755, 772, 809, 821, 869, 955, 984, 1005, 1016, 1029, 1039, 1082, 1115, 1174, 1183, 1192, 1227, 1261, 1301, 1371, 1389, 1449, 1469, 1494, 1508, 1609, 1735, 2821, 2878, 2937, 3031.

Synthesis of **2AZ-8CPP**.

Under nitrogen atmosphere, $SnCl_2 \cdot 2H_2O$ (96 mg, 0.42 mmol) was dissolved in THF (0.5 mL). HClaq (12 M, 0.07 mL, 0.84 mmol) was added to the solution and the mixture was stirred at room temperature for 30 min.

On the other hand, under nitrogen atmosphere, **9** (31 mg, 0.03 mmol) was dissolved in THF (7 mL). The solution of H_2SnCl_4aq (0.2 mL) was added to the solution of **9** and stirred at room temperature to 65°C and 65°C for 13 h (overnight). After cooled down to room temperature, the solvent was removed under reduced pressure. The crude mixture was purified by silica gel column chromatography ($CHCl_3$) and preparative gel permeation chromatography using chloroform as the eluent to give **2AZ-8CPP** (6.3 mg, 6.8 μmol) as white solid in 23 % yield. **^{1}H NMR** ($CDCl_3$, 400 MHz) δ −1.19 (s, 6H), 0.22 (s and s, 6H), 1.67–1.87 (m, 12H), 3.52–3.53 (m, 4H), 7.28–7.29 (m, overlap with water, 2H), 7.51–7.53 (d, *J* = 8.3 Hz, 2H), 7.57–7.75 (m, 24H), 7.82–7.88 (dd and d, *J* = 8.1, *J* = 1.8 and 1.2 Hz, *J* = 8.5 Hz, 4H). **^{13}C NMR** ($CDCl_3$, 100 MHz) δ 17.08, 17.44, 17.49, 25.59, 29.29, 47.44, 47.53, 67.76, 97.84, 97.92, 124.50, 124.93, 125.20, 126.81, 127.15, 127.36, 127.61, 127.71, 129.36, 134.56, 134.63, 138.00, 138.27, 138.56, 138.70, 138.82, 139.12. **HRMS** (p-ESI, MeOH sol) m/z: Calcd for $C_{68}H_{61}N_4$ $[M + H]^+$, 933.48907, found 933.48932. **IR** (on CsI plate [cm^{-1}]) 522, 542, 567, 703, 739, 757, 810, 850, 865, 943, 959, 1002, 1018, 1026, 1043, 1068, 1074, 1110, 1154, 1254, 1333, 1346, 1372, 1389, 1447, 1469, 1484, 1497, 1526, 1599, 2860, 2924, 2930, 2946, 2953, 3025, 3035, 3042, 3050, 3068, 3078.

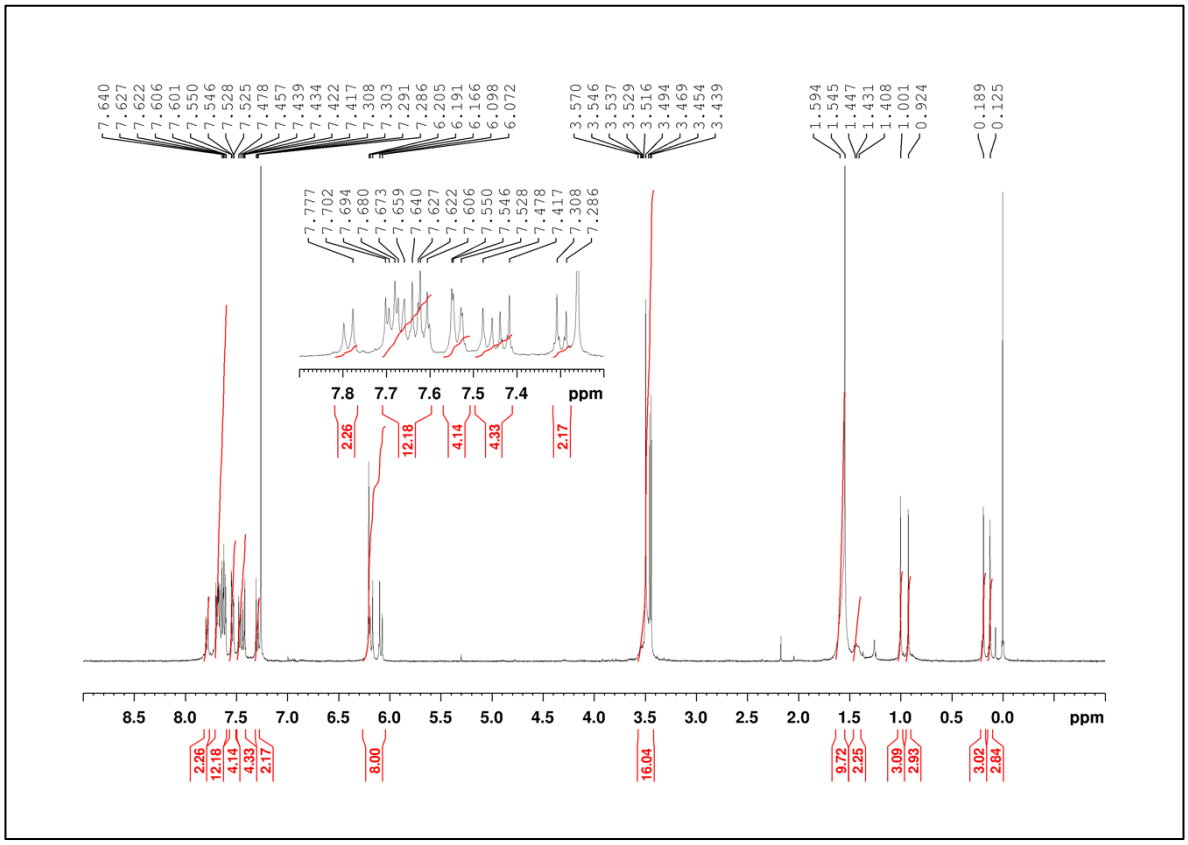

Figure S3.1: ^{1}H NMR spectrum of compound **8**.

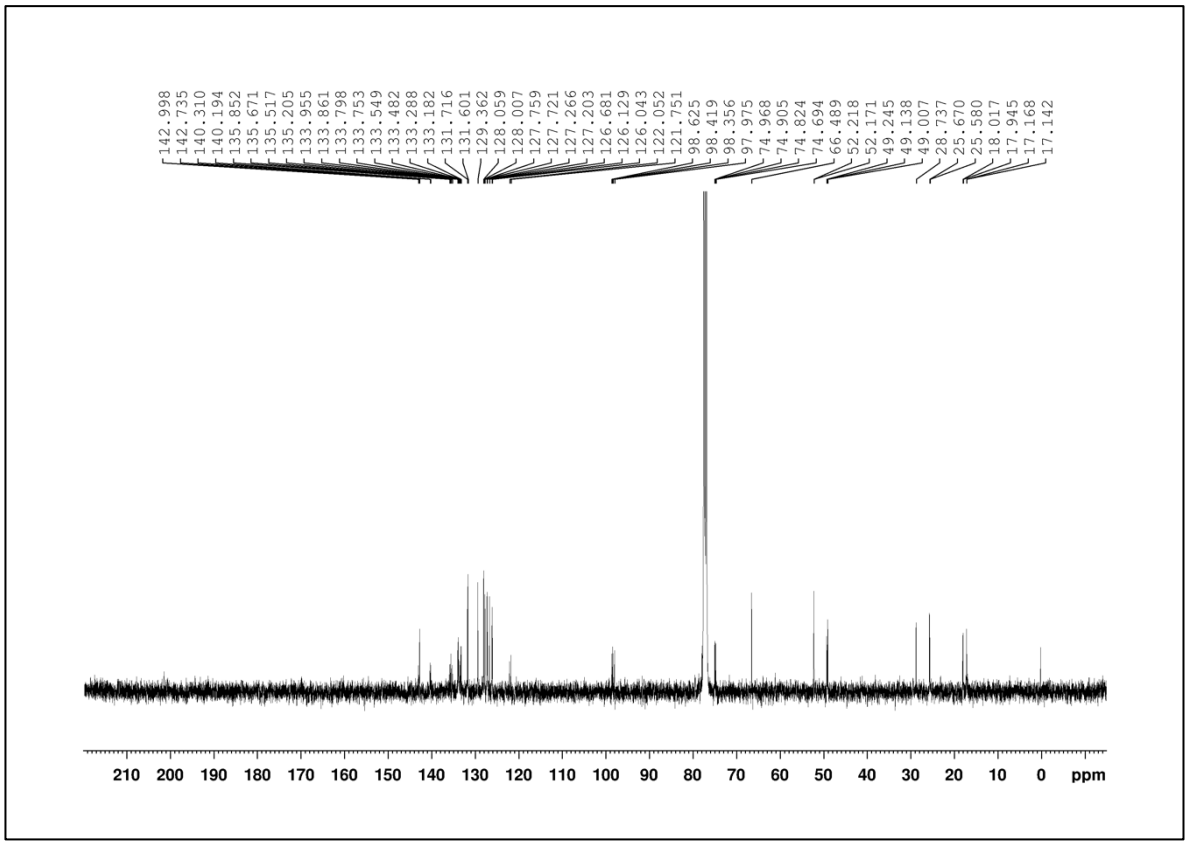

Figure S3.2: ^{13}C NMR spectrum of compound **8**.

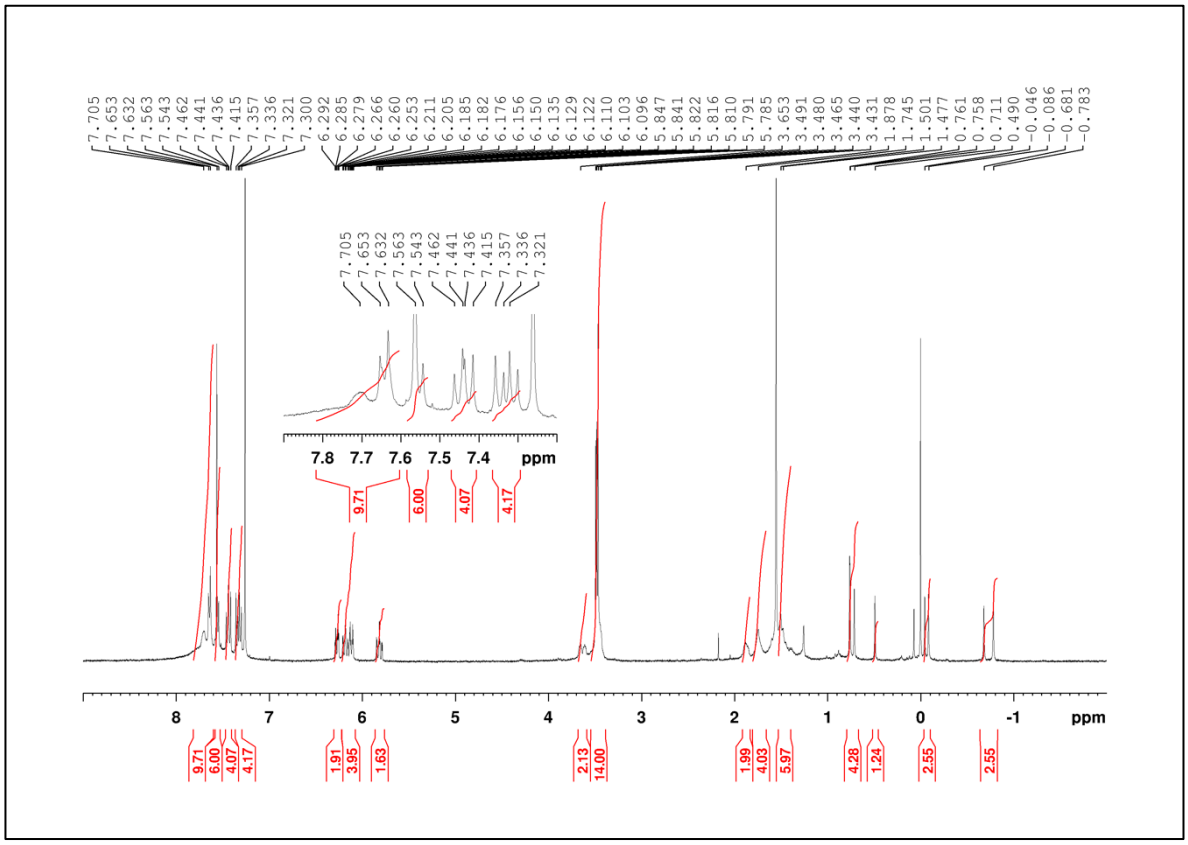

Figure S3.3: ^{1}H NMR spectrum of compound **9**.

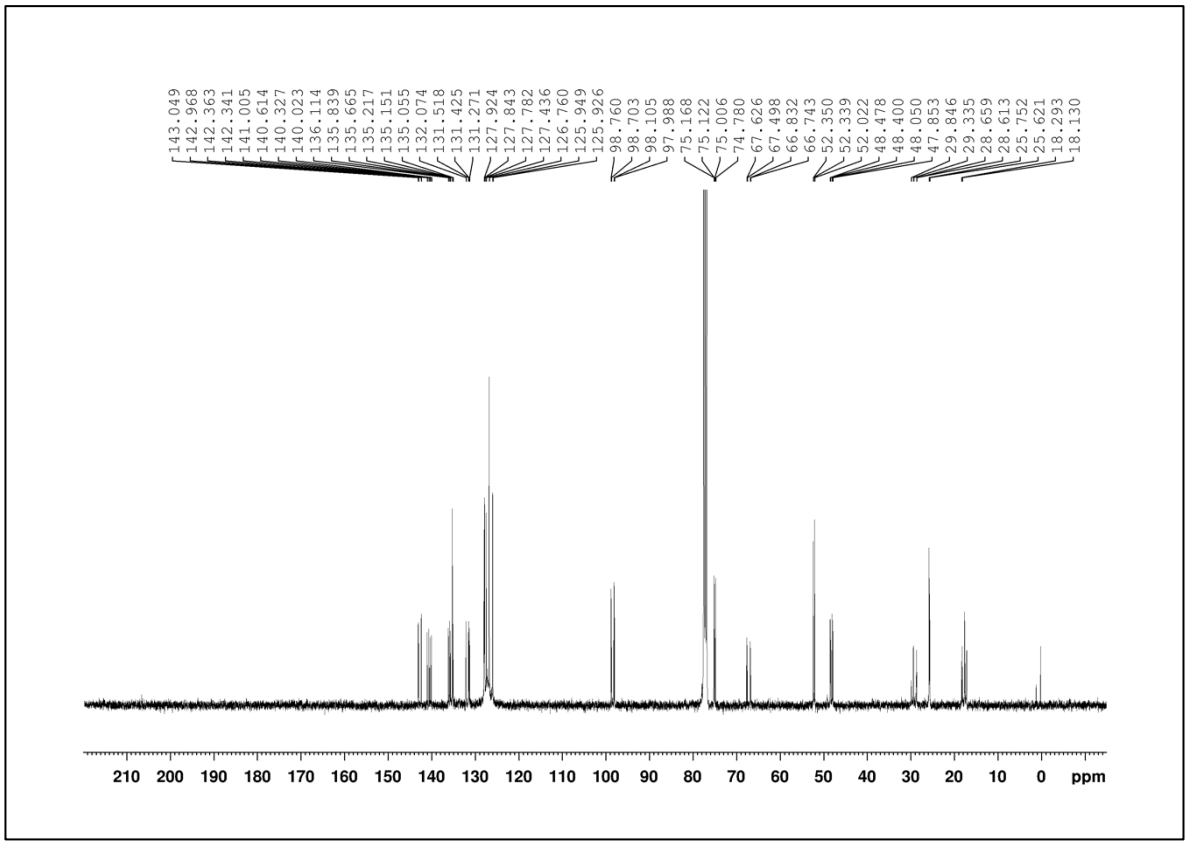

Figure S3.4: ^{13}C NMR spectrum of compound **9**.

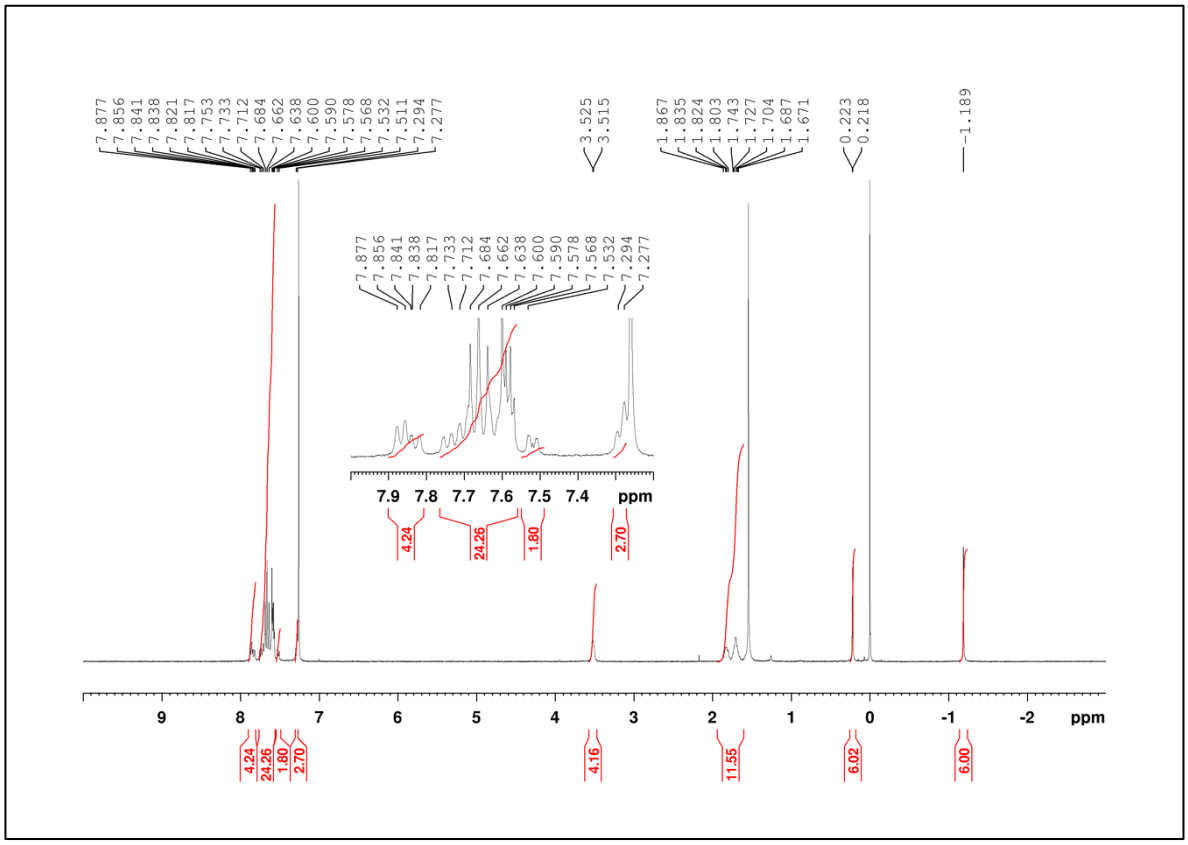

Figure S3.5: ^{1}H NMR spectrum of **2AZ-8CPP**.

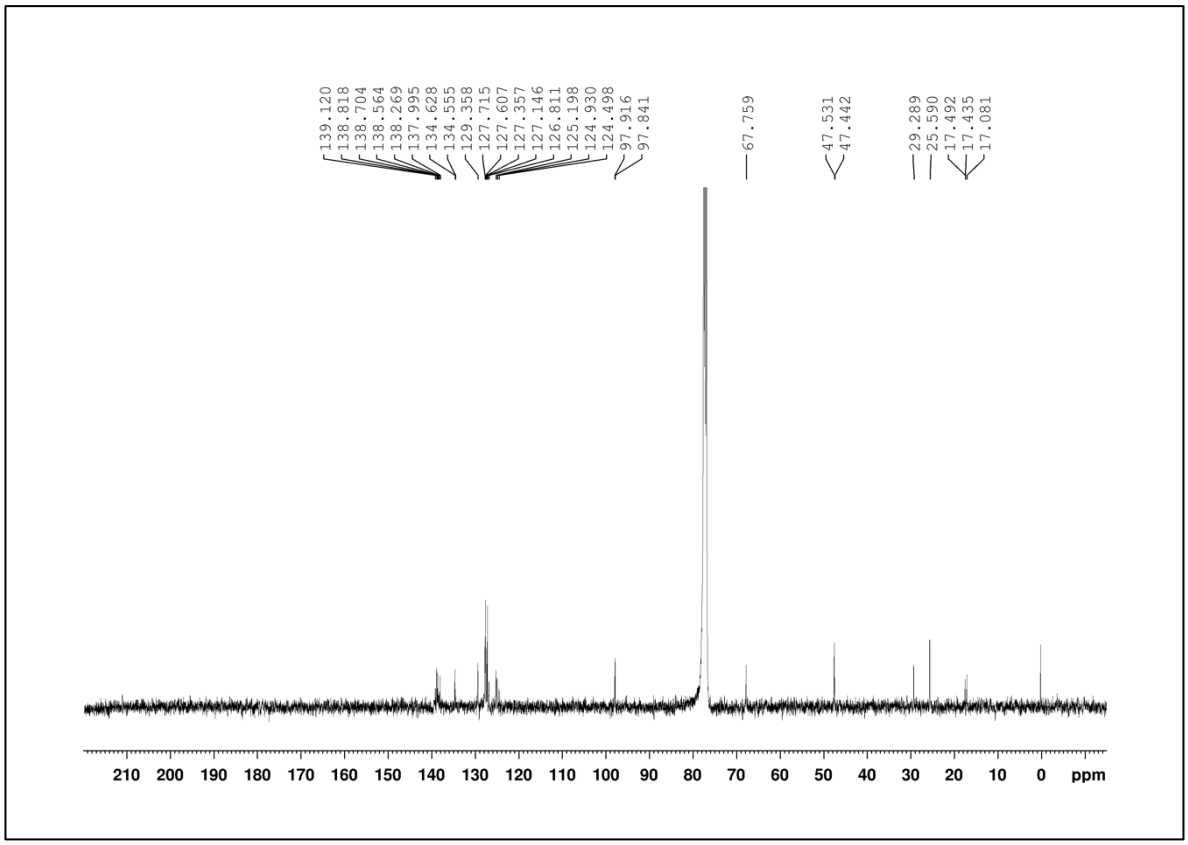

Figure S3.6: ^{13}C NMR spectrum of **2AZ-8CPP**.

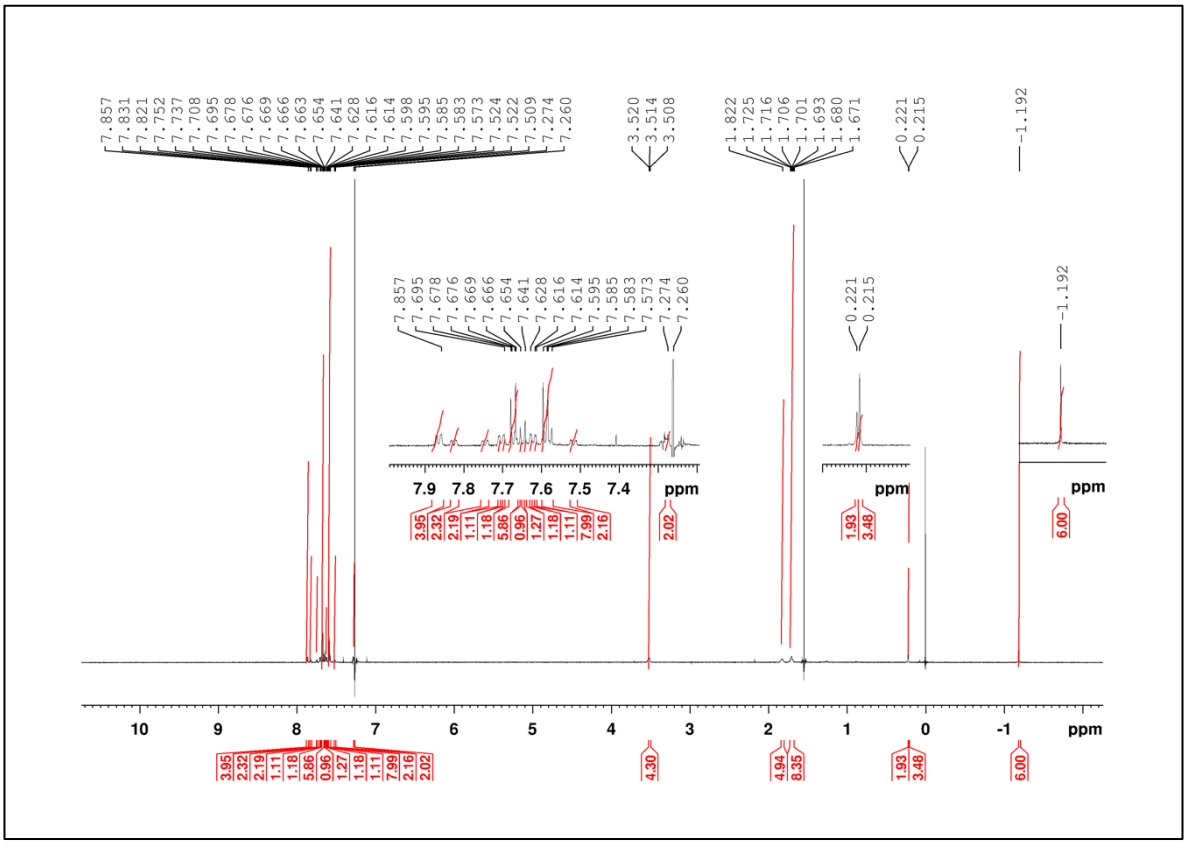

Figure S3.7: [1]H NMR spectrum of **2AZ-8CPP** (700 MHz).

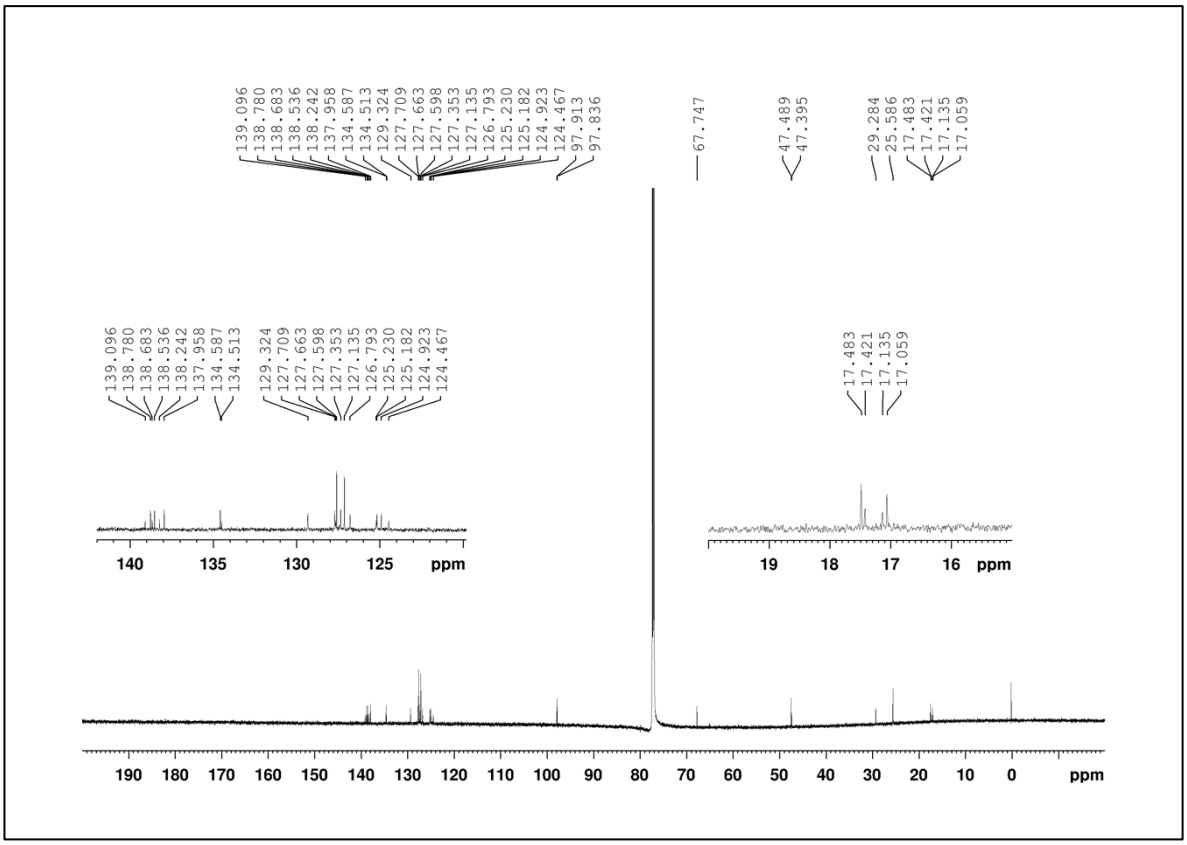

Figure S3.8: [13]C NMR spectrum of **2AZ-8CPP** (176 MHz).

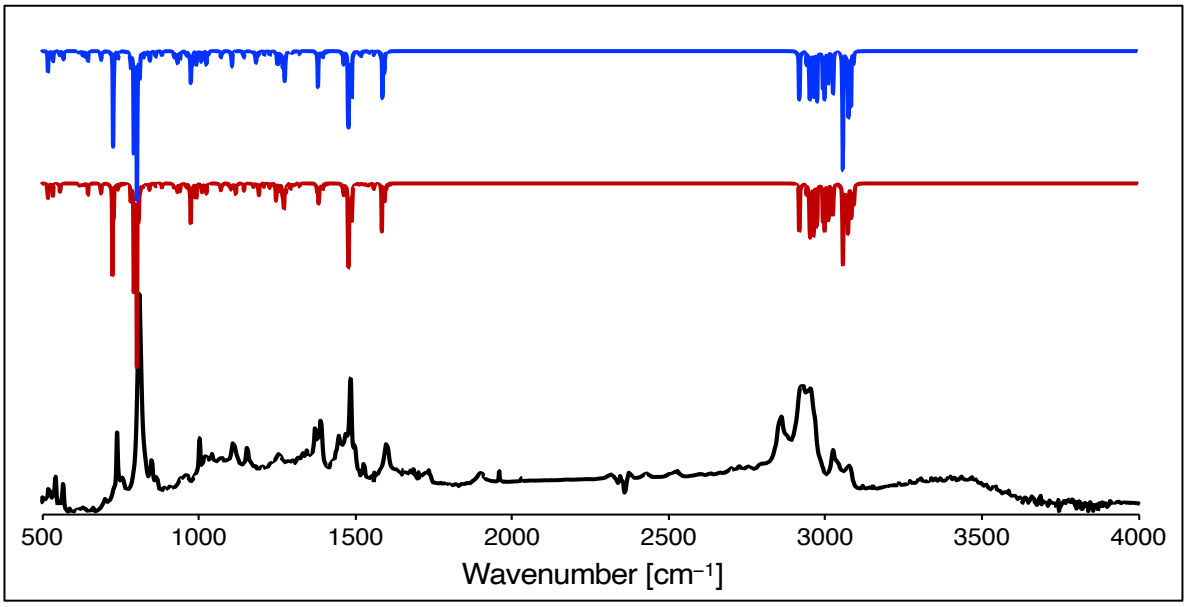

Figure S3.9: Experimental (balck) and computed (red: syn, blue: anti) IR spectra of **2AZ-8CPP** on CsI plate.

Table S3.1: Crystal data and structure refinement for **2AZ-8CPP** with thermal ellipsoids at 50% probability (gray : C, blue : N, red : O, white : H).

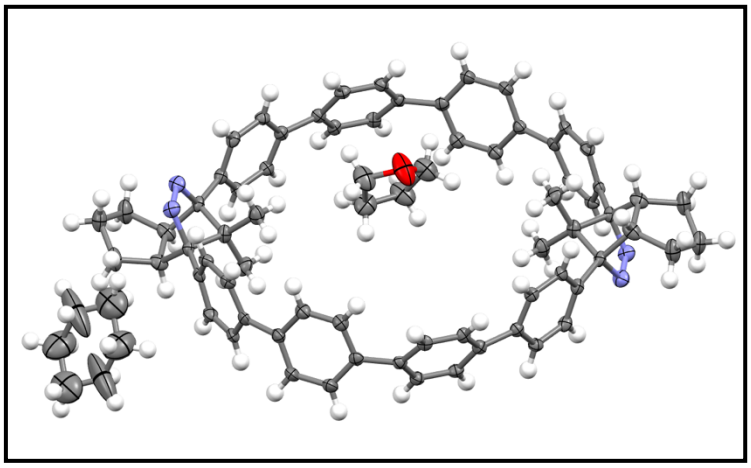

Type of the radiation	MoKα
Formula	$C_{78}H_{80}N_4O$
Weight	1089.46
Temperature *T* (K)	90
Wavelength λ (Å)	0.71073
Crystal system	Monoclinic
Space group	$P12_1/c1$
Unit cell	a (Å) = 20.514(8) α (deg) = 90 b (Å) = 8.040(3) β (deg) = 109.926(5) c (Å) = 20.740(7) γ (deg) = 90
Volume	3216.(2)
z	2
Density (calculation)	1.125
μ (mm^{-1})	0.066
F(000)	1168
Crystal shape	Needle
Color	Colorless
Cryst size (mm^3)	0.01×0.05×0.10
Theta range for data collection (deg)	1.99 to 25.39
Index ranges	−13<=h<=24, −9<=k<=9, −24<=l<=24
Number of Reflns	5890
Params	399
Goodness-of-fit on F^2	1.033
*R*1, *wR*2 [*I*>2σ (*I*)]	0.0788, 0.1946
*R*1, *wR*2 (all data)	0.1502, 0.2342

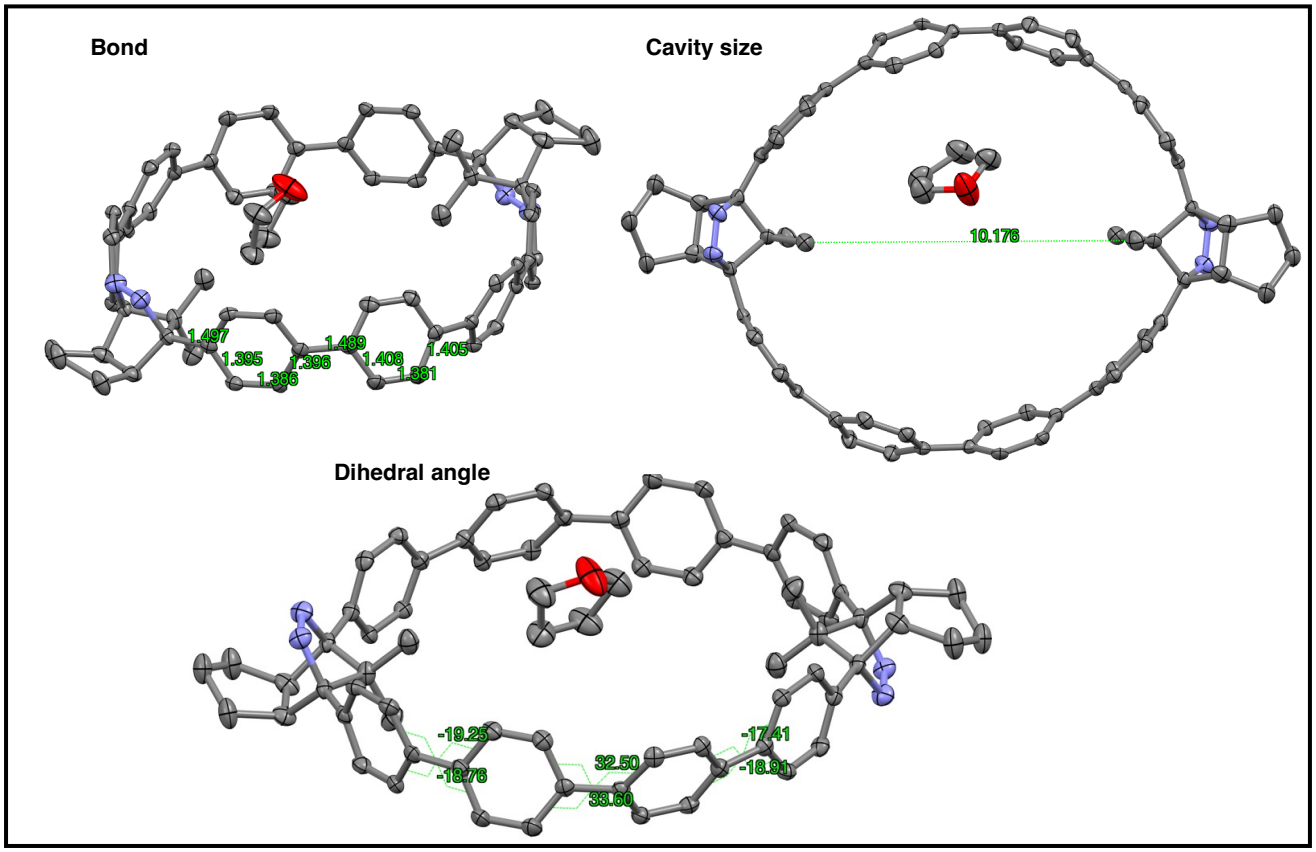

Figure S3.10: Bond length, cavity size, and dihedral angle of **2AZ-8CPP**. Cyclohexane and hydrogen atoms are omitted for clarity.

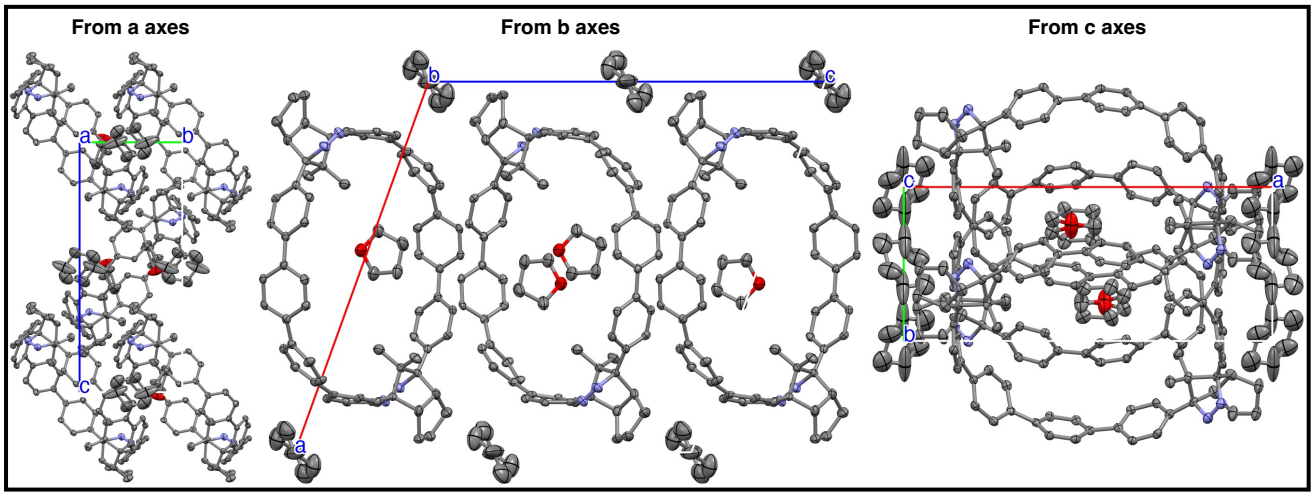

Figure S3.11: Crystal packing structure along a, b, and c axes, respectively. Hydrogen atoms are omitted for clarity.

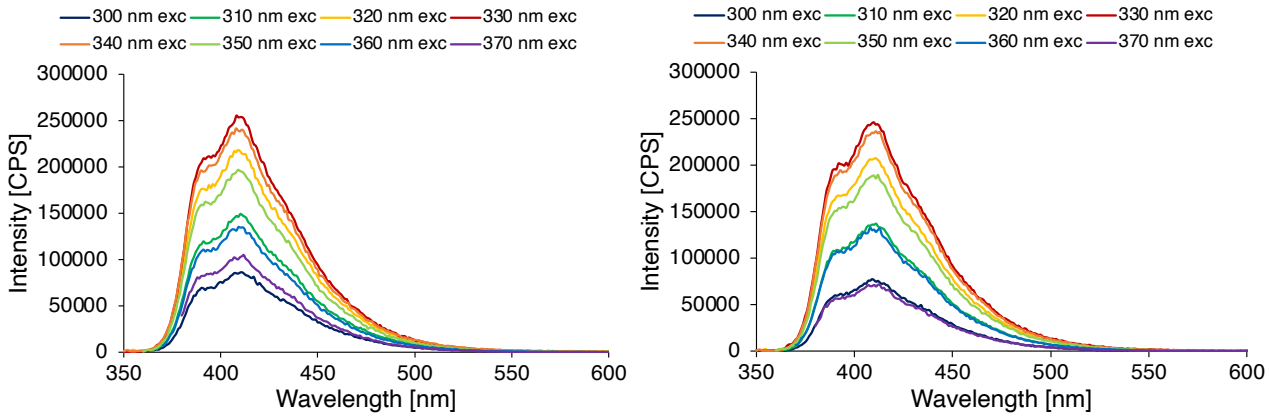

Figure S3.12: Emission spectra of **2AZ-8CPP** under nitrogen (left) and air (right) atmosphere (exc = excitation wavelength). Emission quantum yield $\Phi_f = 0.39 \pm 0.01$ (under nitrogen) and 0.34 ± 0.01 (under air) calculated by comparing with the emission intensity of 9,10-diphenylantracene ($\Phi_f = 0.91$). Emission lifetime $\tau = 1.2 \pm 0.0$ ns (under nitrogen) and 1.1 ± 0.0 ns (under air).

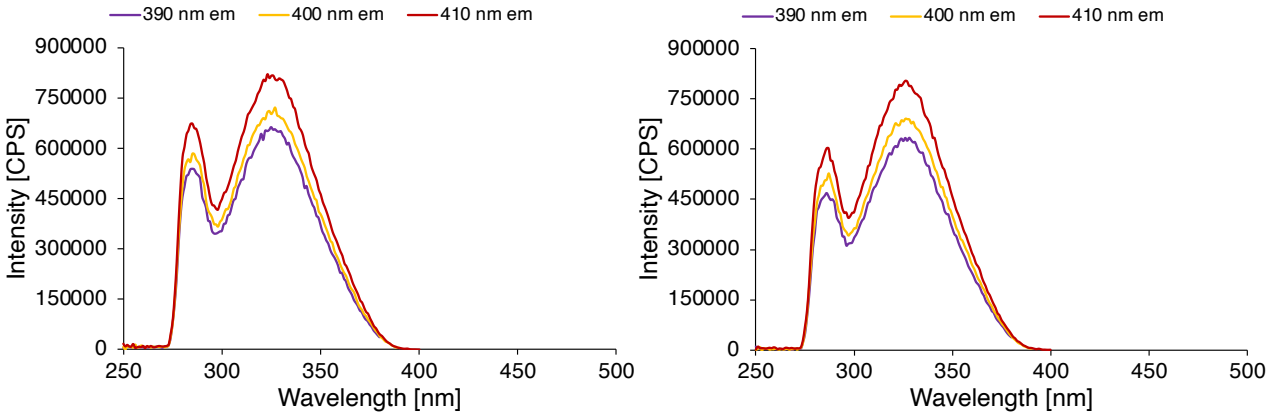

Figure S3.13: Excitation spectra of **2AZ-8CPP** under nitrogen (left) and air (right) atmosphere (em = monitoring emission wavelength).

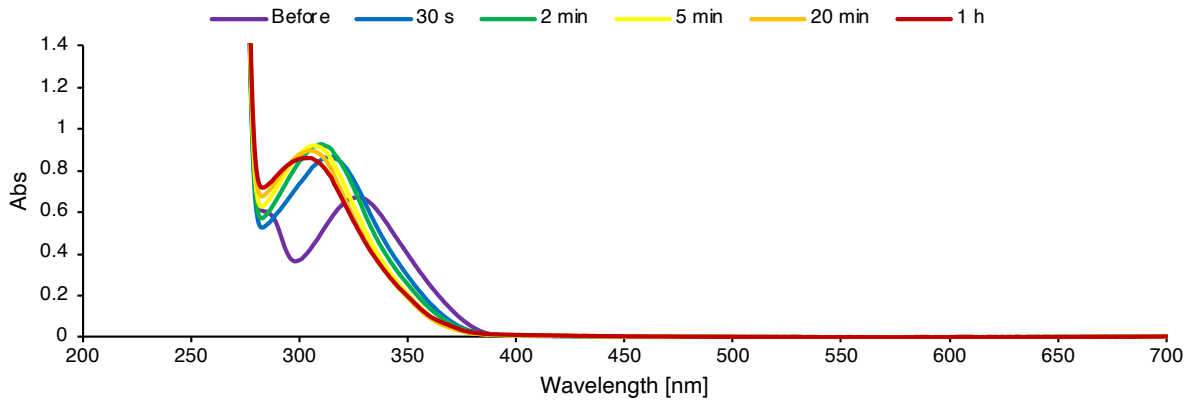

Figure S3.14: Photoreaction of **2AZ-8CPP** with 365 nm LED light monitored by UV-vis absorption spectroscopy in degassed benzene.

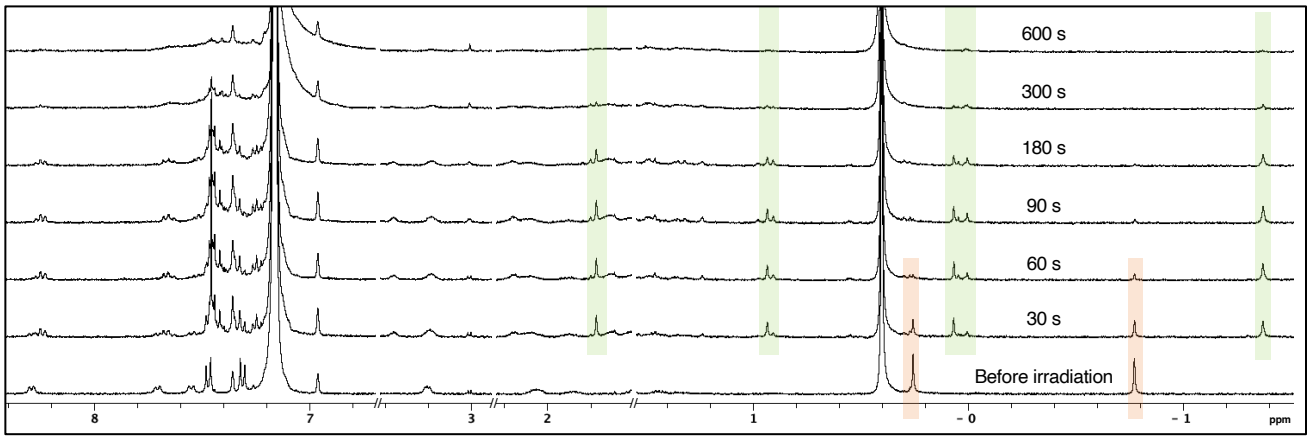

Figure S3.15: ^{1}H NMR analysis (400 MHz) of the photolysis of **2AZ-8CPP** (0.9 mM) by 365 nm LED light in degassed C_6D_6 solution.

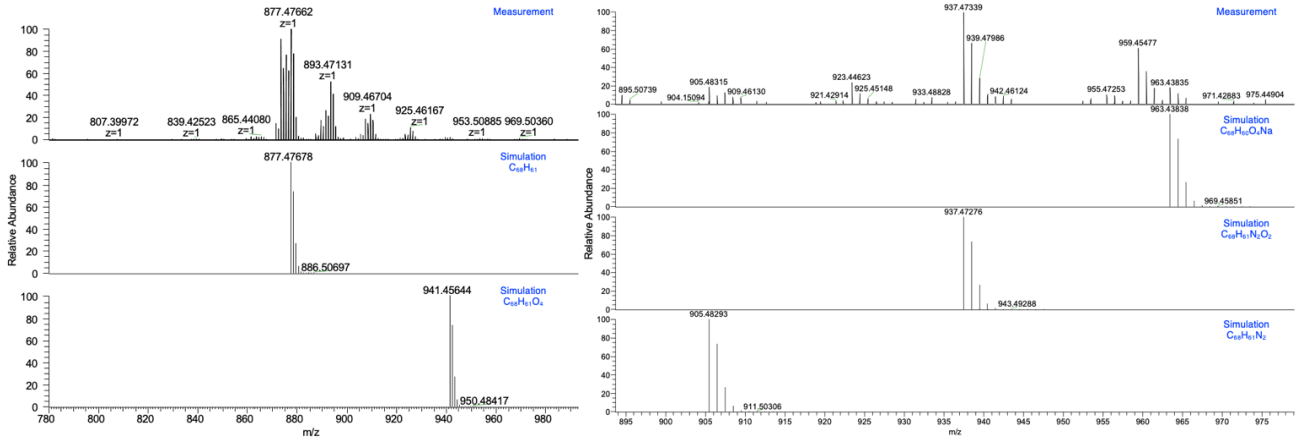

Figure S3.16: HRMS data (APCI and p-ESI, MeOH sol) and simulation of products (left: UV sample, right: NMR sample).
Calcd for $C_{68}H_{61}N_2$ $[M + H]^+$, 877.47678, found 877.47662 / $C_{68}H_{61}O_4$ $[M + H]^+$, 941.45644, found 941.45697.
Calcd for $C_{68}H_{60}O_4Na$ $[M + Na]^+$, 963.43838, found 963.43835 / $C_{68}H_{61}N_2O_2$ $[M + H]^+$, 937.47276, found 937.47339 / $C_{68}H_{61}N_2$ $[M + H]^+$, 905.48293, found 905.48315.

Section 3.10.3: Experimental data.

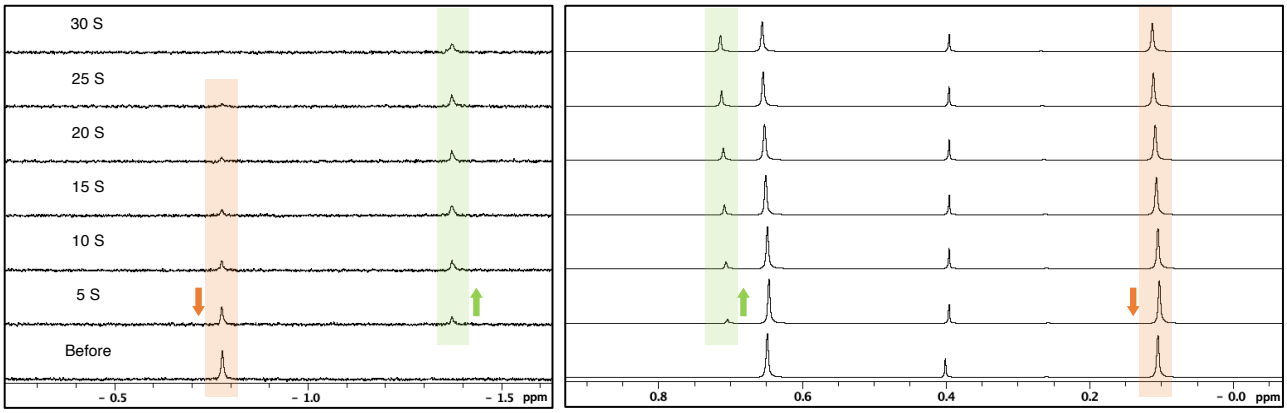

Figure S3.17: In-situ ^{1}H NMR analysis of determination of first denitrogenation quantum yield of **2AZ-8CPP** (left) and reference of denitrogenation quantum yield of **AZ-2Ph** in degassed C_6D_6 (right) with 365 nm LED light.

Table S3.2: Determination parameter of denitrogenation quantum yield of **2AZ-8CPP**.

	Integral ratio		**2AZ-8CPP**		
Time / s	0.38 – 0.41 (H_2O) / ppm	−0.76 – −0.80 / ppm	Ratio / ×100 %	Con : I / μM	Log[$(10^{I_0} - 1)/(10^{I} - 1)$]
0	1	0.0369	1	113 (I_0)	0
5	1	0.0182	0.493	55.7	0.307
10	1	0.0106	0.287	32.5	0.542
15	1	0.0055	0.149	16.8	0.827
20	1	0.0024	0.065	7.35	1.187
25	1	0.0019	0.051	5.82	1.288
30	1	0.0012	0.031	3.52	1.506

Table S3.3: Determination parameter of denitrogenation quantum yield of **AZ-2Ph**.

	Integral ratio		**AZ-2Ph**		
Time / s	0.38 – 0.41 (H_2O) / ppm	0.09 – 0.13 / ppm	Ratio / ×100 %	Con : I / mM	Log[$(10^{I_0} - 1)/(10^{I} - 1)$]
0	1	3.9396	1	19 (I_0)	0
5	1	3.6925	0.937	17.8	0.029
10	1	3.6256	0.920	17.5	0.037
15	1	3.4251	0.869	16.5	0.062
20	1	3.3213	0.843	16.0	0.076
25	1	3.0920	0.785	14.9	0.107
30	1	2.9456	0.748	14.2	0.129

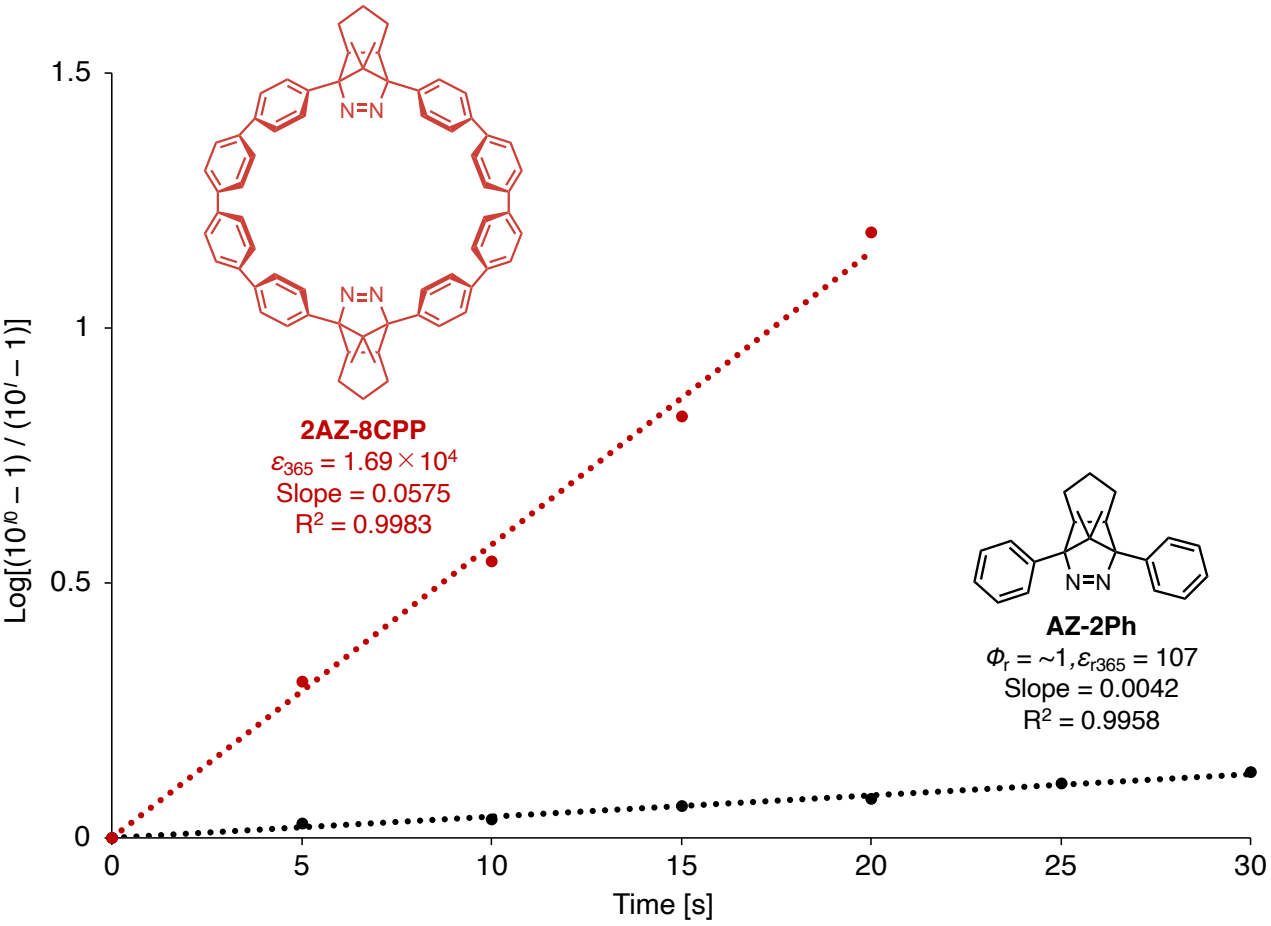

Figure S3.18: Time profiles of decomposition of azoalkane **AZ-2Ph** (black) and **2AZ-8CPP** (red) as monitored by ^{1}H NMR spectroscopy using 365 nm LED light.

First Quantum yield of denitrogenation $\Phi_{\mathbf{2AZ\text{-}8CPP}} = \text{Slope}_{\mathbf{2AZ\text{-}8CPP}} / \text{Slope}_{\mathbf{AZ\text{-}2Ph}} \times \varepsilon_{r365} / \varepsilon_{365} \times \Phi_r = 0.086$

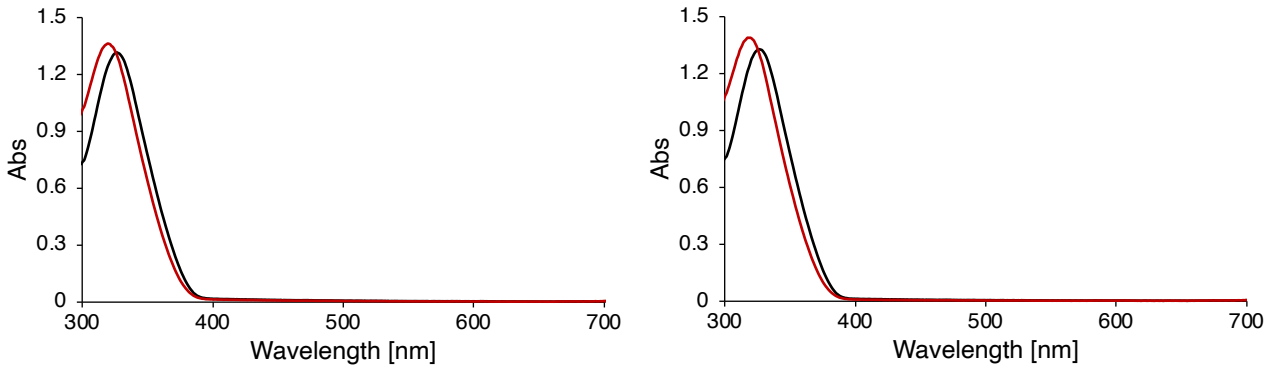

Figure S3.19: UV-vis absorption spectra of sub-microsecond LFP measurement under nitrogen (left) and air (right) atmosphere (black: before, red: after, benzene solution: 38 μM).

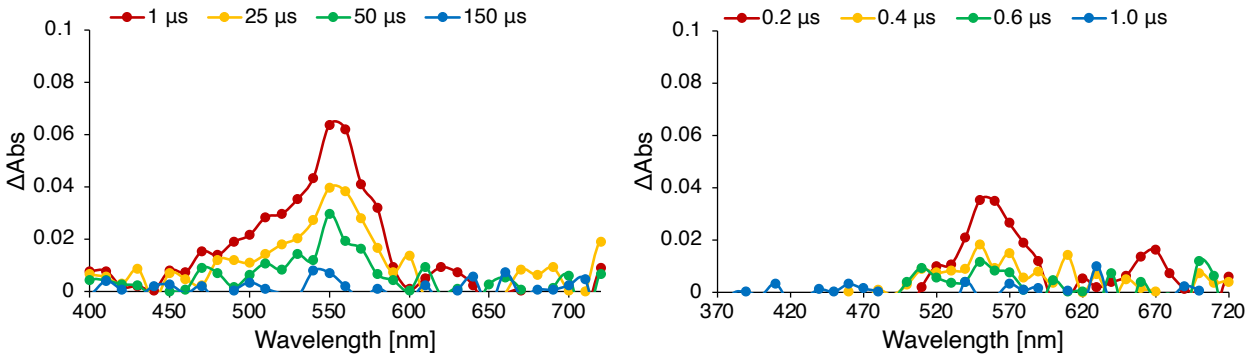

Figure S3.20: Transient absorption spectra of sub-microsecond LFP measurement at 295 K under nitrogen (left) and air (right) atmosphere with 355 nm laser (4.0 mJ) in benzene.

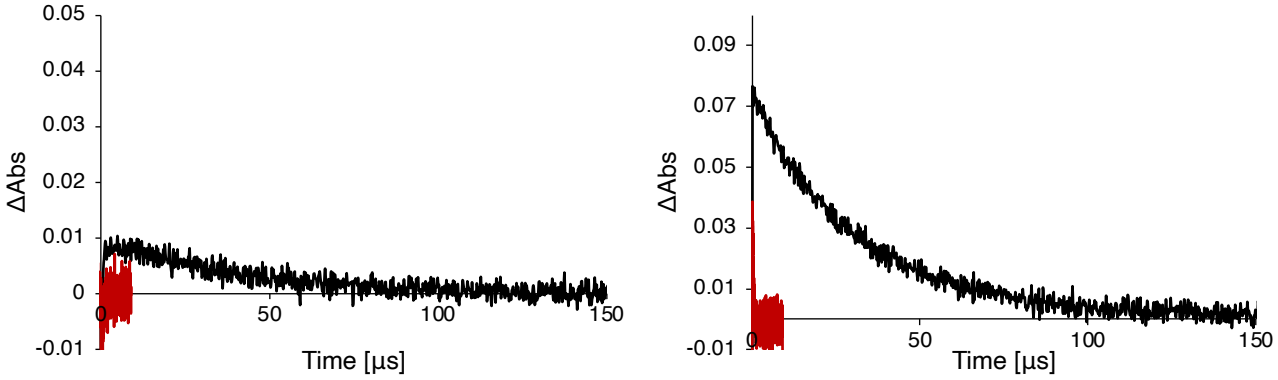

Figure S3.21: Time profile at 400 nm (left) and 560 nm (right) in nitrogen (black) and air (red) atmosphere.

Table S3.4: Time profile at 400 nm (left) and 560 nm (right) in nitrogen (black) and air (red) atmosphere.

Condition	Lifetime at 400 nm [µs]	Lifetime at 560 nm [µs]
Under N_2	40.7 ± 0.2	30.7 ± 0.1
Under air	n.d	0.3 ± 0.0

n.d: Not determined.

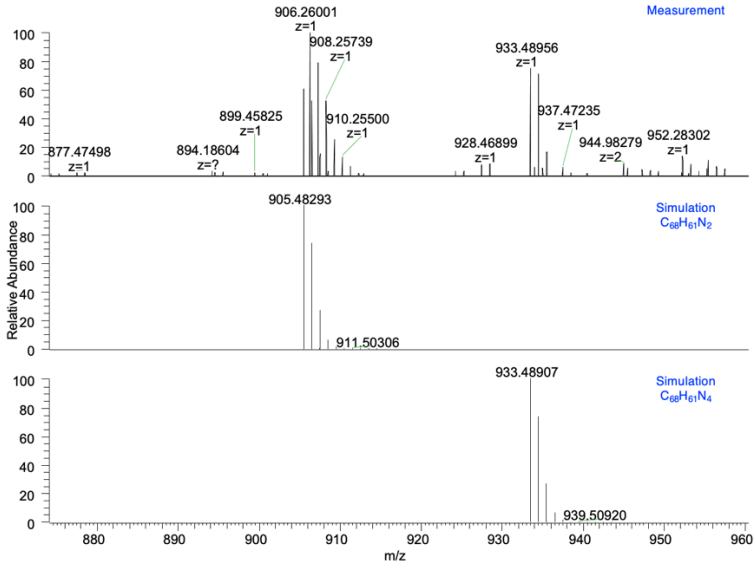

Figure S3.22: HRMS data (p-ESI, MeOH sol) and simulation of sample after LFP measurement under nitrogen. Calcd for $C_{68}H_{61}N_2$ $[M + H]^+$, 905.48293, found 905.48315 / $C_{68}H_{61}N_4$ $[M + H]^+$, 933.48907, found 933.48956.

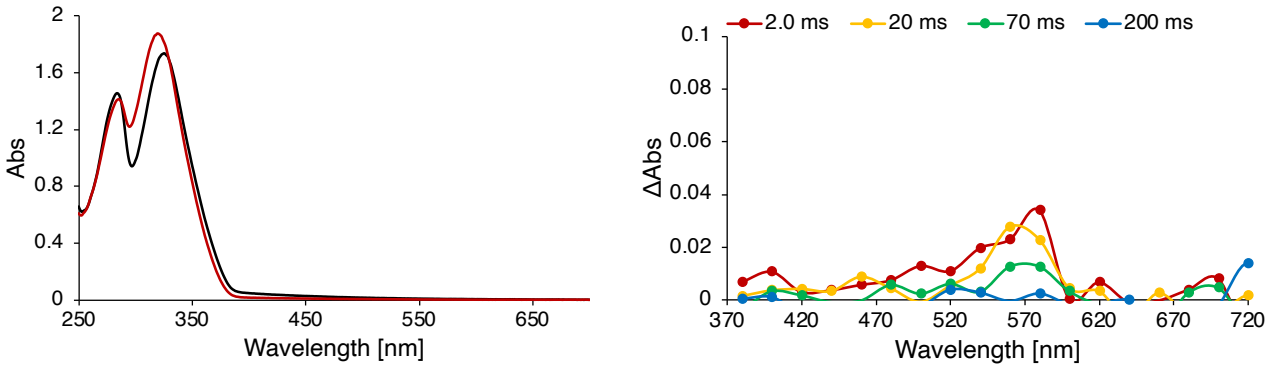

Figure S3.23: UV-vis absorption spectra of sub-microsecond LFP measurement under argon atmosphere (black: before, red: after, 2-MTHF solution: 56 μM) and transient absorption spectra of sub-microsecond LFP measurement at 124 K under argon atmosphere with 355 nm laser (4.3 mJ) in 2-MTHF.

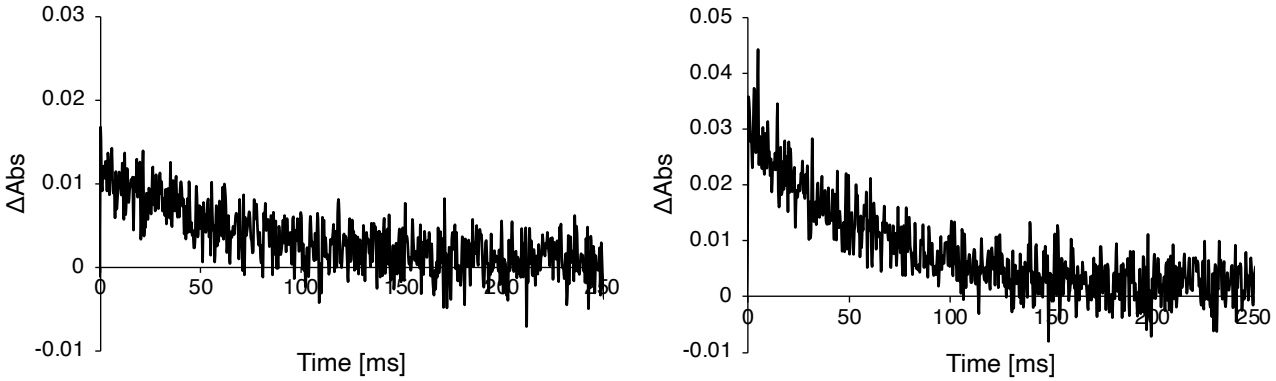

Figure S3.24: Time profile at 400 nm (left) and 560 nm (right) at 124 K in argon atmosphere.

Table S3.5: The lifetime of transient species at each wavelength.

Condition	Lifetime at 400 nm [ms]	Lifetime at 560 nm [ms]
Under Ar	66.5 ± 0.5	57.7 ± 0.4

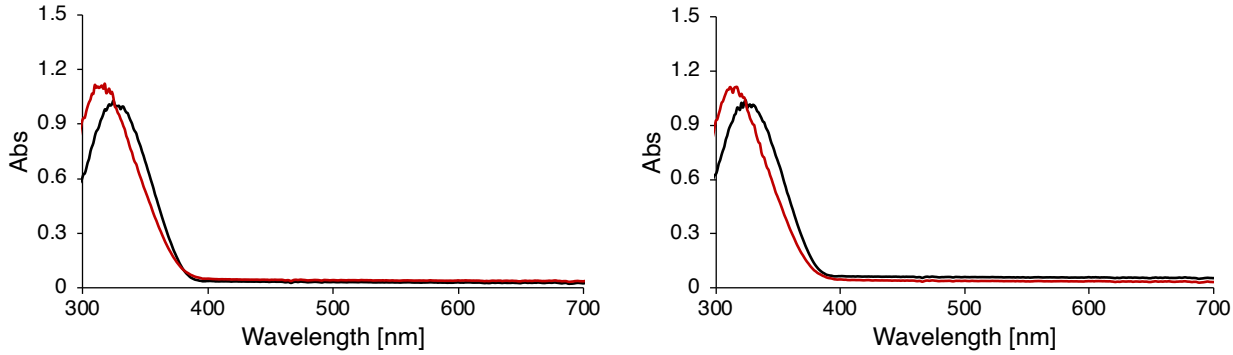

Figure S3.25: UV-vis absorption spectra of sub-nanosecond LFP measurement under nitrogen (left) and air (right) atmosphere (black: before, red: after, benzene solution: 0.2 mM).

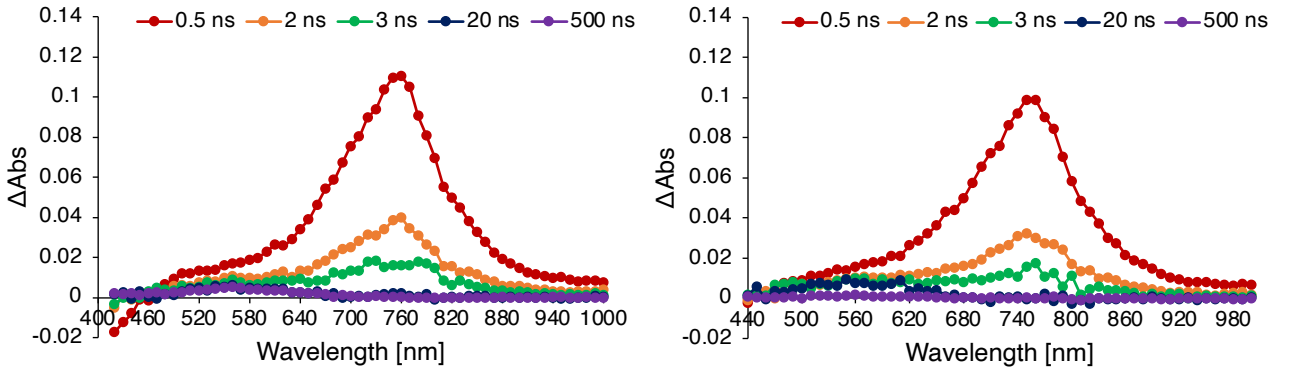

Figure S3.26: Transient absorption spectra of sub-nanosecond LFP measurement at 295 K under argon (left) and air (right) atmosphere with 355 nm laser (10 μJ) in benzene.

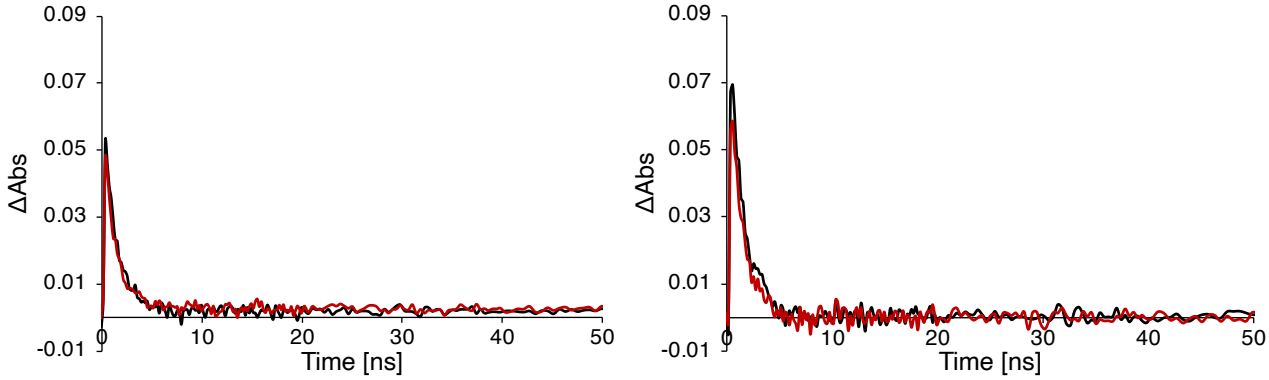

Figure S3.27: Time profile at 660 nm (left) and 800 nm (right) in argon (black) and air (red) atmosphere.

Table S3.6: The lifetime of transient species at each wavelength.

Condition	Lifetime at 660 nm [ns]	Lifetime at 800 nm [ns]
Under Ar	1.28 ± 0.01	1.34 ± 0.02
Under air	1.21 ± 0.01	1.24 ± 0.01

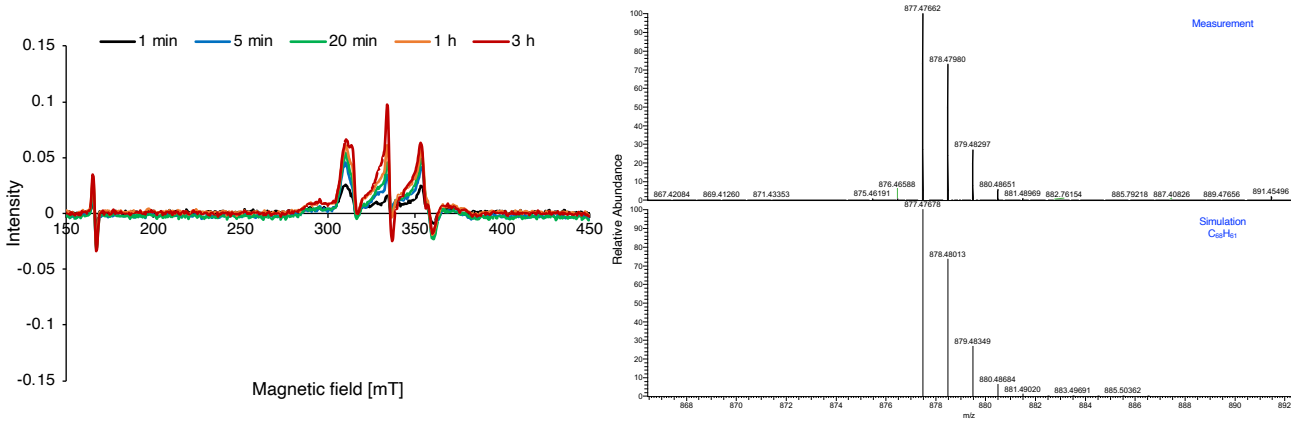

Figure S3.28: EPR spectra of the photolysis of **2AZ-8CPP** (0.1 mM) using 365 nm LED light in 2-MTHF matrix in a sealed quartz tube at 5 K under vacuum conditions and HR-mass spectra (p-ESI, MeOH sol) with simulation of sample after EPR measurement. Calcd for $C_{68}H_{61}$ $[M + H]^+$, 877.47678, found 877.47662.

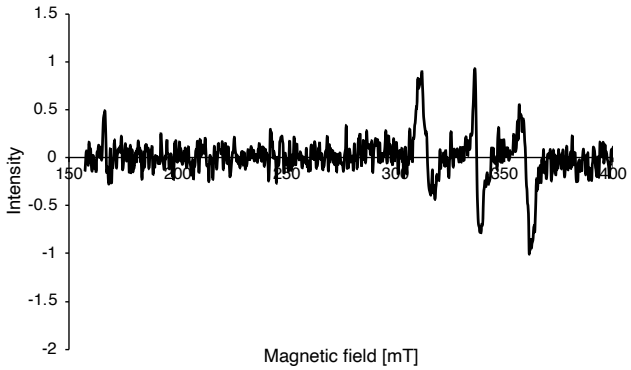

Figure S3.29: EPR spectrum at 20 K after photolysis of **2AZ-8CPP** using UV light in toluene matrix (0.1 mM) in a sealed quartz tube under vacuum condition.

Table S3.7: Computed zfs parameters (|*D*/hc| and |*E*/hc|) for diradical and tetraradical.

Sim	Spin state	|*D*/hc| (|*E*/hc|) [cm^{-1}]
1	Di-radical (Triplet, syn)	0.041 (0.007)
2	Di-radical (Triplet, anti)	0.037 (0.002)
3	Tetra-radical (Quintet, syn)	0.012 (< 0.001)
4	Tetra-radical (Quintet, anti)	0.014 (< 0.001)

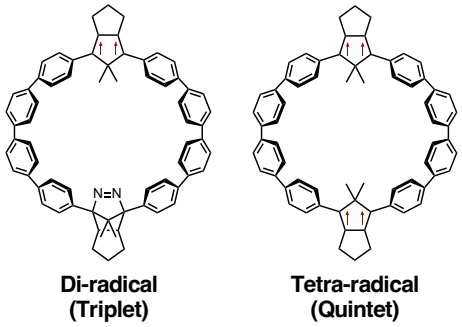

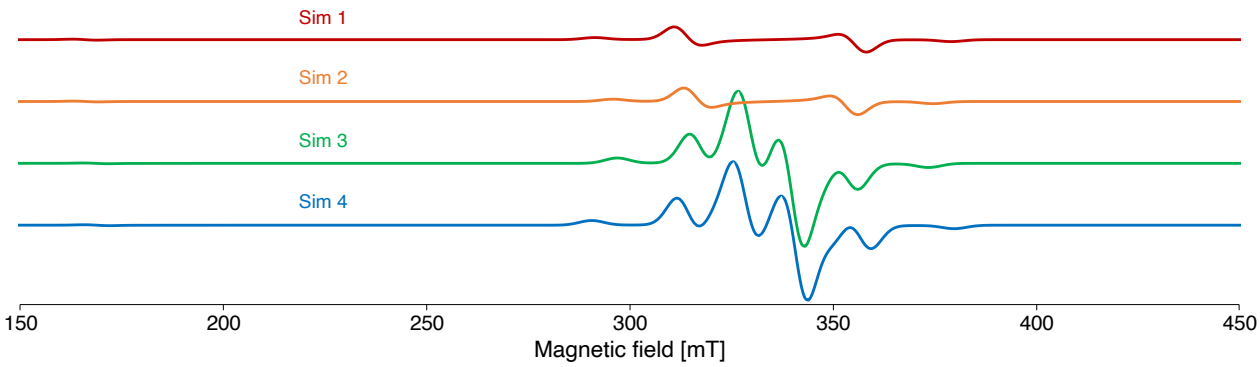

Figure S3.30: Simulated EPR signals using the computed zfs parameters at each spin state.

Section 3.10.4: Computational details.

Quantum chemical computations in gas phase have been performed with the Gaussian 16 (Revision B.01) suite of programs. The energy minimum structures and transition state structures were confirmed by vibrational frequency analysis. Zero-field splitting (zfs) parameters (*D* tensor and *E*/*D* ratio) calculation were performed with ORCA 4.2.1 program at restricted open-shell (RO) BP/EPR-II level of theory. The calculated geometries were optimized at (U)CAM-B3LYP/6-31G(d) level of theory with Gaussian 16 (Revision B.01) before zfs parameters calculations. The automatic auxiliary basis sets (AutoAux) were used in zfs calculations. The *D* tensor calculation included the spin-spin components (SS). The DSS part is an expectation value that involves the spin density of the calculated system directly used the canonical orbitals from the spin density. Anisotropy of the induced current density (ACID) analyses were performed with AICD 3.0.4 software package. The NMR with CSGT method were calculated at UB3LYP/6-31G(d) level of theory. POV-Ray 3.7 on Windows was used for visualization of ACID maps.

Table S3.8: Energy gaps calculated at the R(U)B3LYP/6-31G(d) (upper) and R(U)CAM-B3LYP/6-31G(d) (lower) level of theory.

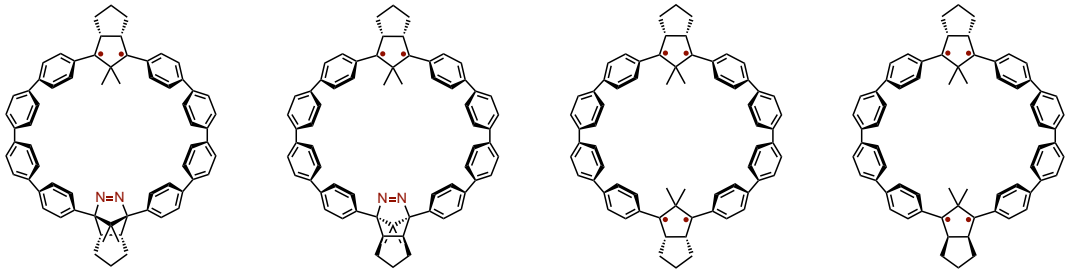

DR-AZ-8CPP	Spin	$<S^2>$	ΔE_{S-T} [kcal mol^{-1}]
syn	Singlet	n.d	n.d
	Triplet	2.0678	0
syn	Singlet	1.0144	−1.54
	Triplet	2.1301	0

DR-AZ-8CPP	Spin	$<S^2>$	ΔE_{S-T} [kcal mol^{-1}]
anti	Singlet	1.0643	+0.12
	Triplet	2.0678	0
anti	Singlet	1.1309	+0.19
	Triplet	2.1345	0

n.d: Open singlet state couldn't be optimized.

2DR-8CPP	Spin	$<S^2>$	$\Delta E_{S,T-Q}$ [kcal mol^{-1}]
syn	Singlet	2.1356	−0.57
	Triplet	3.1305	−0.67
	Quintet	6.1318	0
	R-singlet	0	+25.0
syn	Singlet	2.2866	−0.05
	Triplet	3.2724	−0.04
	Quintet	6.2588	0
	R-singlet	0	+57.2

2DR-8CPP	Spin	$<S^2>$	$\Delta E_{S,T-Q}$ [kcal mol^{-1}]
anti	Singlet	2.1213	+0.13
	Triplet	2.0674	+13.5
	Quintet	6.1235	0
	R-singlet	0	+26.5
anti	Singlet	2.2385	+0.13
	Triplet	3.2350	+0.06
	Quintet	6.2319	0
	R-singlet	0	+59.2

Table S3.9: Strain Energies of **2AZ-8CPP** and **2DR-8CPP** calculated at the R(U)B3LYP/6-31G(d) level of theory.

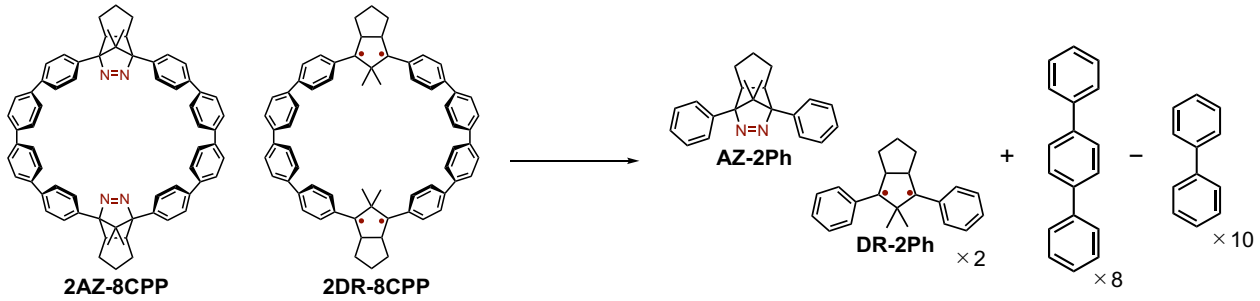

Compound	Strain energy [kcal mol^{-1}]
2AZ-8CPP (syn)	45.2
2AZ-8CPP (anti)	42.6
2DR-8CPP (syn, Quintet)	59.7
2DR-8CPP (anti, Quintet)	58.4

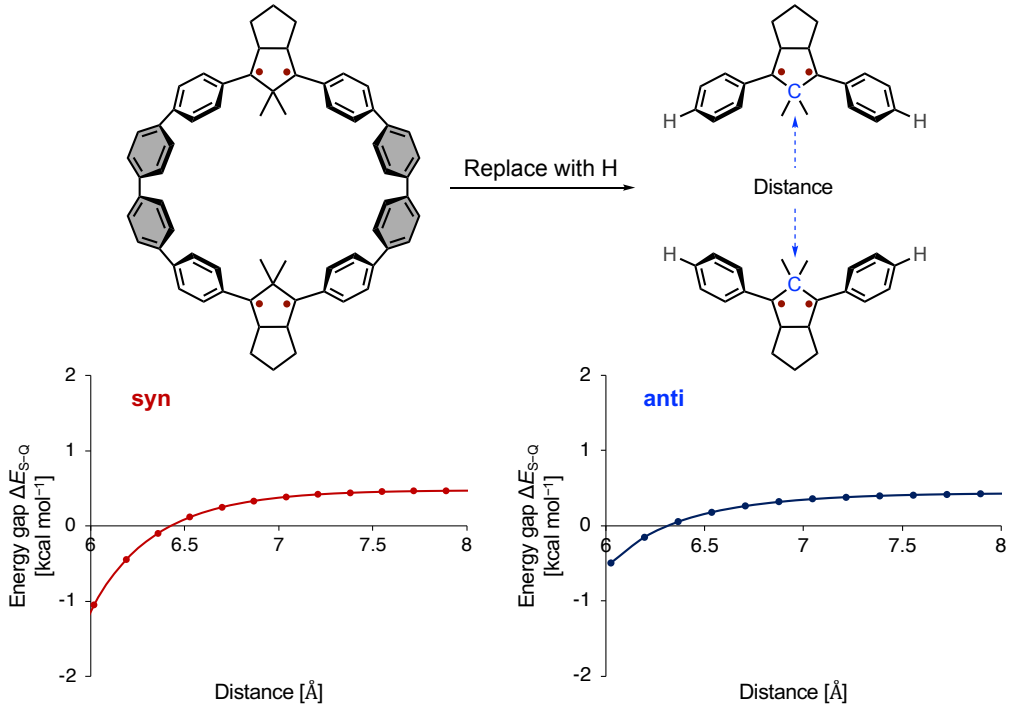

Figure S3.31: Scan calculation between two diradical units using UCAM-B3LYP/6-31G(d) level of theory (ΔE_{S-Q} = Singlet energy E_S − Quintet energy E_Q).

Table S3.10: Results of scan calculation between two diradical units (step size 0.17 Å).

syn		**anti**	
Distance [Å]	ΔE_{S-Q} [kcal mol^{-1}]	Distance [Å]	ΔE_{S-Q} [kcal mol^{-1}]
10.78	0.474	10.96	0.432
10.61	0.474	10.79	0.432
10.44	0.474	10.62	0.432
10.27	0.474	10.45	0.432
10.10	0.474	10.28	0.432
9.93	0.474	10.11	0.432
9.76	0.474	9.94	0.432
9.59	0.474	9.77	0.432
9.42	0.474	9.60	0.432
9.25	0.474	9.43	0.432
9.08	0.474	9.26	0.432
8.91	0.474	9.09	0.432
8.74	0.474	8.92	0.432
8.57	0.474	8.75	0.432
8.40	0.473	8.58	0.432
8.23	0.473	8.41	0.431
8.06	0.471	8.24	0.430
7.89	0.468	8.07	0.427
7.72	0.463	7.90	0.424
7.55	0.455	7.73	0.418
7.38	0.442	7.56	0.410
7.21	0.420	7.39	0.398
7.04	0.387	7.22	0.380
6.87	0.334	7.05	0.354
6.70	0.251	6.88	0.317
6.53	0.118	6.71	0.262
6.36	-0.095	6.54	0.180
6.19	-0.448	6.37	0.053
6.02	-1.047	6.20	-0.150
5.85	-2.104	6.03	-0.491

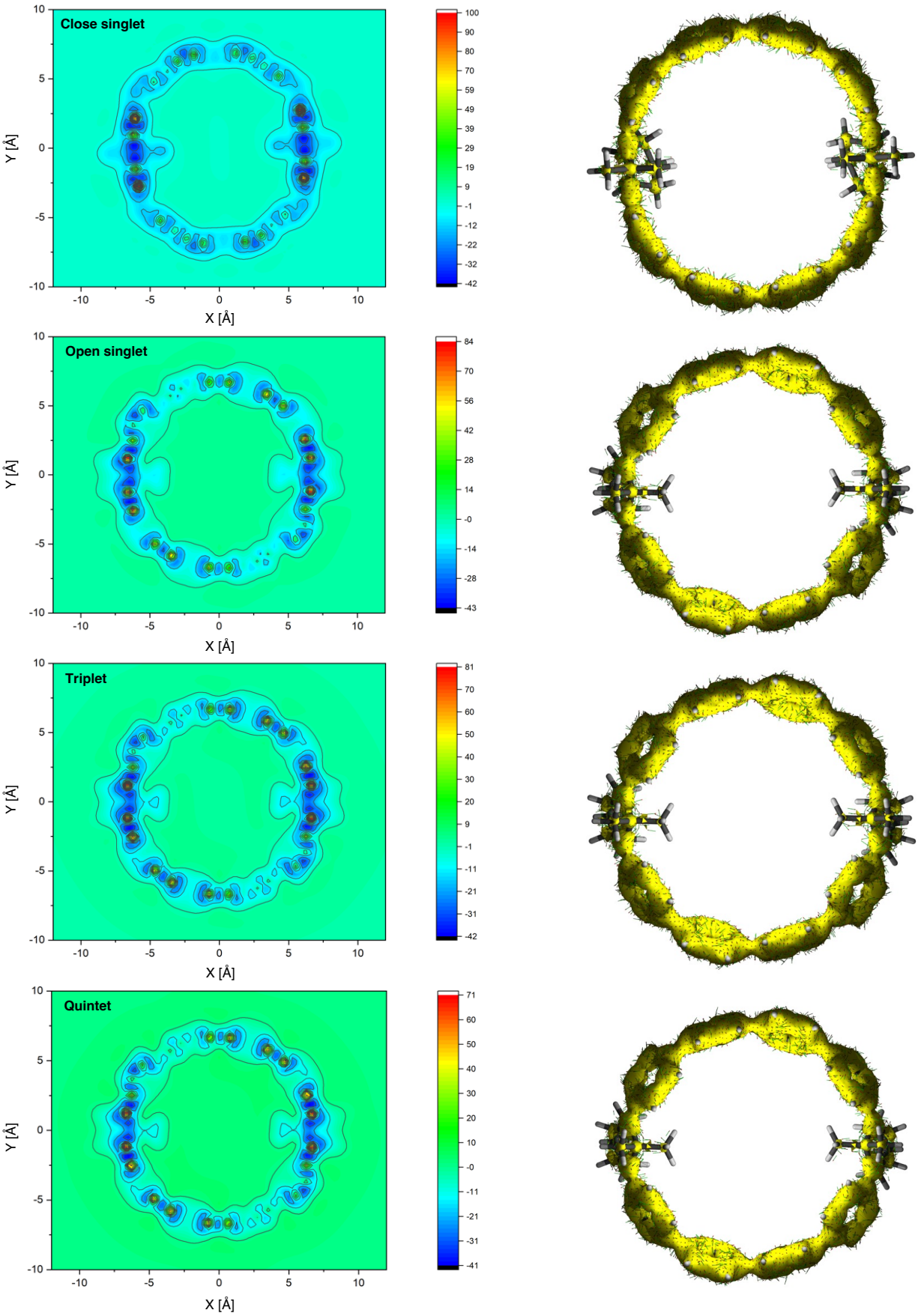

Figure S3.32: A grid plot of the NICS(0)zz value in the XY plane of 2DR-8CPP (syn) and ACID maps.

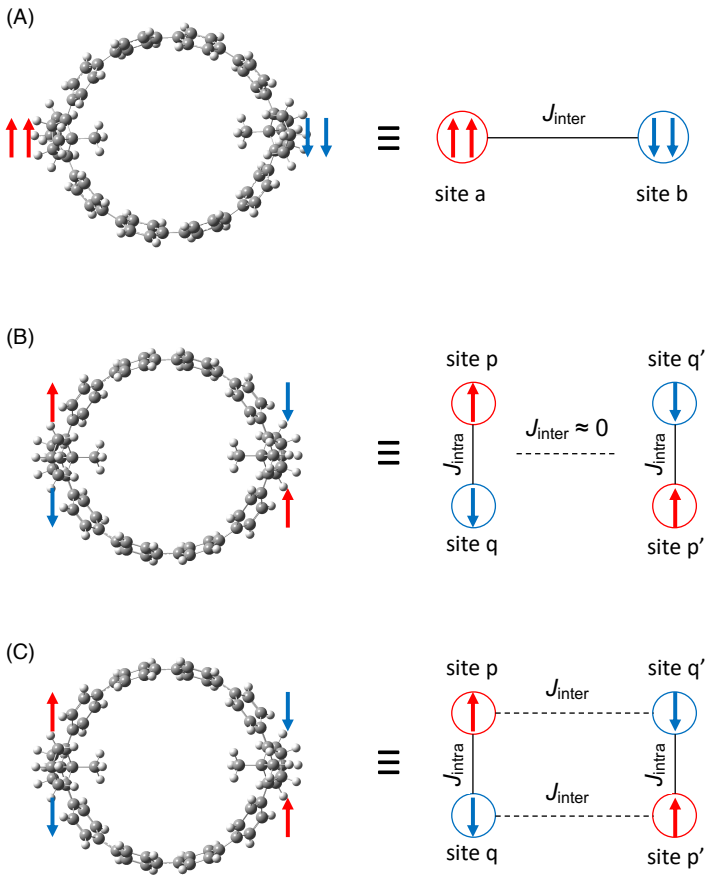

Figure S3.33: Calculation model of tetraradical **2DR-8CPP**.

Appendix I

As shown in (A), if the BS-singlet 1 state is a model consisting of two spin sites, site a and b, the Heisenberg Hamiltonian is

$$H = -2J_{inter}S_aS_b \ldots\ldots \text{(A1)}.$$

According to the approximate spin projection method, J_{inter}, excluding the spin contamination error, is denoted when the energies of the Quintet and BS-singlet 1 states are E_Q and E_{BS1},

$$J_{inter} = (E_{BS1} - E_Q) / (\langle S^2\rangle_Q - \langle S^2\rangle_{BS1}) \ldots\ldots \text{(A2)}.$$

Where $\langle S^2\rangle_X$ is the $\langle S^2\rangle$ value of the spin state X. Since this value does not include spin contamination errors, it is equivalent to the value calculated from the energy of the correct singlet state, considering static electron correlations, and excluding spin contamination errors.

$$J_{inter} = (E_S - E_Q) / (\langle S^2\rangle_Q - \langle S^2\rangle_S) \ldots\ldots \text{(A3)}$$

Where E_S is the energy of the correct singlet state determined by the approximate spin projection method, and $\langle S^2\rangle_S$ is correct singlet $\langle S^2\rangle$ value ($\langle S^2\rangle_S = 0$).

From (A2) and (A3), $E_S = E_{BS1}\langle S^2\rangle_Q / (\langle S^2\rangle_Q - \langle S^2\rangle_{BS1}) - E_Q\langle S^2\rangle_{BS1} / (\langle S^2\rangle_Q - \langle S^2\rangle_{BS1})$ ……(A4)

Next, as shown in Figure S43(B), assuming the BS-singlet 2 state to be a dimer model consisting of two spin sites (p (p') and q(q')) and $J_{inter} \approx 0$, Heisenberg Hamiltonian is

$$H = -2J_{intra}S_pS_q - 2J_{intra}S_{p'}S_{q'} = -4J_{intra}S_pS_q \ldots\ldots \text{(A5)}.$$

When the energies of the Quintet and BS-singlet 2 states are E_Q and E_{BS2},

$$E_Q = -4J_{intra}\langle S_pS_q\rangle_Q \ldots\ldots \text{(A6i)}$$

$$E_{BS2} = -4J_{intra}\langle S_pS_q\rangle_{BS2} \ldots\ldots \text{(A6j)}.$$

Where $\langle S_pS_q\rangle_X$ is the spin correlation function of state X. Total spin Hamiltonian is $S = S_p + S_q$.

$$\text{From } S^2 = S_p^2 + S_q^2 + 2S_pS_q \ldots\ldots \text{(A7)},$$

$$E_Q = -2J_{intra}\{\langle S^2\rangle_Q - \langle S_p^2\rangle_Q - \langle S_q^2\rangle_Q\} \ldots\ldots \text{(A8i)}$$

$$E_{BS2} = -2J_{intra}\{\langle S^2\rangle_{BS2} - \langle S_p^2\rangle_{BS2} - \langle S_q^2\rangle_{BS2}\} \ldots\ldots \text{(A8j)}$$

There is no change in the spin density distribution between quintet and BS-singlet 2 states,

$$\langle S_p^2\rangle_Q = \langle S_p^2\rangle_{BS2} \ldots\ldots \text{(A9i)}$$

$$\langle S_q^2\rangle_Q = \langle S_q^2\rangle_{BS2} \ldots\ldots \text{(A9j)}$$

$$\text{From } E_{BS2} - E_Q = 2J_{intra}(\langle S^2\rangle_Q - \langle S^2\rangle_{BS2}) \ldots\ldots \text{(A10)},$$

$$J_{intra} = (E_{BS2} - E_Q) \,/\, \{2(\langle S^2\rangle_Q - \langle S^2\rangle_{BS2})\} \ldots\ldots \text{(A11)}.$$

Since this J_{intra} is a value without spin contamination error, as in the discussion of (A2) and (A3),

E_S is determined as follows from $(E_S - E_Q) \,/\, \{2(\langle S^2\rangle_Q - \langle S^2\rangle_S)\} = (E_{BS2} - E_Q) \,/\, \{2(\langle S^2\rangle_Q - \langle S^2\rangle_{BS2})\} \ldots \text{(A12)}$.

$$E_S = E_{BS2}\,\langle S^2\rangle_Q \,/\, (\langle S^2\rangle_Q - \langle S^2\rangle_{BS1}) - E_Q\,\langle S^2\rangle_{BS2} \,/\, (\langle S^2\rangle_Q - \langle S^2\rangle_{BS1}) \ldots\ldots \text{(A13)}.$$

Appendix II

In the case of spin contamination error in the structure of BS-singlet 1 and BS-singlet 2 state, the nuclear coordinate derivatives of E_S in (A4) or (A13) should be obtained. nuclear coordinate derivatives of E_S is

$$G_s(\mathrm{R}) = \{\alpha(\mathrm{R})G_{BS1}(\mathrm{R}) - \beta(\mathrm{R})G_Q(\mathrm{R})\} + \partial\alpha \,/\, \partial\mathrm{R}\{E_{BS1} - E_Q\} \ldots\ldots \text{(A14i)}.$$

Also, for BS-singlet 2 state,

$$G_s(\mathrm{R}) = \{\alpha(\mathrm{R})G_{BS2}(\mathrm{R}) - \beta(\mathrm{R})G_Q(\mathrm{R})\} + \partial\alpha \,/\, \partial\mathrm{R}\{E_{BS2} - E_Q\} \ldots\ldots \text{(A14j)}.$$

Where G is nuclear coordinate derivative of energy, α and β is put as follows,

$$\alpha = (\langle S^2\rangle_Q - \langle S^2\rangle_S) \,/\, (\langle S^2\rangle_Q - \langle S^2\rangle_{BS1 \text{ or } 2})$$

$$\beta = \alpha - 1$$

Also,

$$\partial\alpha \,/\, \partial\mathrm{R} \approx \{(\langle S^2\rangle_Q - \langle S^2\rangle_S) \,/\, (\langle S^2\rangle_Q - \langle S^2\rangle_{BS1 \text{ or } 2})\}\; \partial\langle S^2\rangle_{BS1 \text{ or } 2} \,/\, \partial\mathrm{R}$$

In this open shell molecules, the second term in (A14) can be neglected because $\langle S^2\rangle$ value does not change with a small shift in coordinates, and the energy difference between the singlet and the quintet is very small.

Therefore, for BS-singlet 1 state, $G_s(\mathrm{R}) \approx \{\alpha(\mathrm{R})G_{BS1}(\mathrm{R}) - \beta(\mathrm{R})G_Q(\mathrm{R})\} \ldots\ldots \text{(A15i)}$.

Also, for BS-singlet 2 state, $G_s(\mathrm{R}) \approx \{\alpha(\mathrm{R})G_{BS2}(\mathrm{R}) - \beta(\mathrm{R})G_Q(\mathrm{R})\} \ldots\ldots \text{(A15j)}$

Using this energy derivative equation, structural optimization was performed using the BS-singlet 1 and BS-singlet 2 structures as initial structures. The convergence condition conforms to the opt = loose condition of Gaussian 09.

Appendix III

Finally, as shown in Figure (C), all spins of p, q, p', and q' are regarded as spin sites. Considered a four-spin site model with J_{intra} and J_{inter} as the spin coupling parameters within and between biradical sites, respectively.

Spin Hamiltonian is

$$H = -2J_{intra}S_pS_q - 2J_{intra}S_{p'}S_{q'} - 2J_{inter}S_pS_{q'} - 2J_{inter}S_qS_{p'} \ldots\ldots \text{ (A16).}$$

Since the energies of the Quintet state in the BS-singlet 1 and BS-singlet 2 structures and the energy in the Quintet structure are almost identical (maximum difference is 0.03 kcal mol^{-1}), the structures can be regarded as almost energetically same. Assuming the most stable BS-singlet 1 structure, J_{intra} and J_{inter} are calculated from the energy difference between BS-singlet 1, BS-singlet 2 and Quintet states. The spin Hamiltonians corresponding to Quintet, BS-singlet1, and BS-singlet2 when assuming the Ising model are

$$\text{Quintet : } H^{Quintet} = -J_{intra} - J_{inter} \ldots\ldots \text{(A17i)}$$

$$\text{BS-singlet 1 : } H^{BS1} = -J_{intra} + J_{inter} \ldots\ldots \text{(A17j)}$$

$$\text{BS-singlet 2 : } H^{BS2} = J_{intra} + J_{inter} \ldots\ldots \text{(A17k)}$$

From these equations, J_{intra} and J_{inter} are calculated from

$$J_{inter} = -(E^{Quintet} - E^{BS1}) / 2 \ldots\ldots \text{(A18i)}$$

$$J_{intra} = -(E^{BS1} - E^{BS2}) / 2 \ldots\ldots \text{(A18i)}$$

Table S3.11: Calculated total energies and $<S^2>$ values of optimized structures in THF.

	Singlet			
	BS-singlet 1	BS-singlet 2	Spin-projected BS1	Spin-projected BS2
Total energy [a.u.]	-2627.21466602	-2627.21427358	-2627.21466072	-2627.21426700
$<S^2>$	2.1252	2.1273	2.1255	2.1277
Quintet state energy on the singlet structure				
Total energy [a.u.]	-2627.21400633	-2627.21403090	-2627.21398820	-2627.21400289
$<S^2>$	6.1230	6.1282	6.1230	6.1286
BS-singlet 2 state energy on the BS-singlet 1 structure				
Total energy [a.u.]	-2627.21416072			
$<S^2>$	2.1204			
Spin-projected energy [a.u.]	-2627.21501671	-2627.21440261	-2627.21501830	-2627.21440746

	Quintet	Triplet	Singlet
			Spin restricted
Total energy [a.u.]	-2627.21404832	-2627.21418431	-2627.17432752
$<S^2>$	6.1206	3.1190	0.0000

Table S3.12: Calculated total energies and $<S^2>$ values of optimized structures in the gas phase.

	Singlet		
	BS-singlet 1	BS-singlet 2	Spin restricted
Total energy [a.u.]	-2627.20205681	-2627.20170505	-2627.16048075
$<S^2>$	2.1268	2.1295	0.00000
Quintet state energy on the singlet structure			
Total energy [a.u.]	-2627.20147181	-2627.20152844	
$<S^2>$	6.1243	6.1302	
AP energy [a.u.]	-2627.20236805	-2627.20179906	

	Quintet	Triplet
Total energy [a.u.]	-2627.20150186	-2627.20161387
$<S^2>$	6.1228	3.1214

Reference.

1. Jasti, R.; Bhattacharjee, J.; Neaton, J. B.; Bertozzi, C. R., *J. Am. Chem. Soc*. **2008**, *130*, 17646–17647.
2. (a) Lee, C.; Yang, W.; Parr, R. G. *Phys. Rev. B*. **1988**, *37*, 785–789. (b) Becke, A. D. *J. Chem. Phys*. **1993**, *98*, 5648–5652. (c) Ditchfield, R. *Mol. Phys*. **1974**, *27*, 789–807. (d) Er, N. B.; Mcweenyt, R. *Phys. Rev*. **1962**, *126*, 1028– 1034. (e) Wolinskv, K.; Hinton, J. F.; Pulay, P. *J. Am. Chem. Soc*. **1990**, *112*, 8251–8260.
3. Stratmann, R. E.; Scuseria, G. E. Frisch, M. J. *J. Chem. Phys*. **1998**, *109*, 8218–8224.
4. (a) Zhao, Y.; Truhlar, D. G. *Theor. Chem. Acc*. **2008**, *120*, 215–241. (b) Abe, M.; Watanabe, S.; Tamura, H.; Boinapally, S. Kanahara, K.; Fujiwara, Y. *J. Org. Chem*. **2013**, *78*, 1940–1948.
5. Ahmd, I.; Ahmed, S.; Sheraz, M. A.; Aminuddin, M.; Hussain, F.; Vaid, M. *Chem. Pharm. Bull*. **2009**, *57*, 1363–1370.
6. Miyazawa, Y.; Wang, Z.; Matsumoto, M.; Hatano, S.; Antol, I.; Kayahara, E.; Yamago, S.; Abe, M. *J. Am. Chem. Soc*. **2021**, *143*, 7426–7439.
7. (a) Fenn, J. B.; Mann, M.; Meng, C. K.; Wong, S. F.; Whitehouse, C. M. *Science*. **1989**, *246*, 64–71. (b) Zeleny, J. *Phys. Rev.* **1914**, *3*, 69–91.
8. (a) Prter, G. *Proc. R. Soc. Lond*. **1950**, *A200*, 284–300. (b) Norrish, R.; Porter, G. *Nature*. **1949**, *164*, 658.
9. Nakagawa, T.; Okamoto, K.; Hanada, H.; Katoh, R. *Opt. Lett*. **2016**, *41*, 1498–1501.
10. Adam, W.; Maas, W.; Nau, W. M. *J. Org. Chem*. **2000**, *65*, 8790–8796.
11. (a) Neese, F. *Wiley Interdiscip. Rev.*: *Comput. Mol. Sci*. **2012**, *2*, 73−78. (b) Neese, F. *Wiley Interdiscip. Rev.*: *Comput. Mol. Sci*. **2018**, *8*, 4−9.
12. Matsuoka, H.; Ozawa, N.; Kodama, T.; Nishikawa, H.; Ikemoto, I.; Kikuchi, K.; Furukawa, K.; Sato, K.; Shiomi, D.; Takui, T.; Kato, T. *J. Phys. Chem. B*. **2004**, *108*, 13972–13976.
13. (a) Sato, K.; Yano, M.; Furuici, M.; Shiomi, D.; Takui, T.; Abe, K.; Itoh, K.; Higuchi, A.; Katsuma, K.; Shirota, Y. *J. Am. Chem. Soc*. **1997**, *119*, 6607–6613. (b) Matsuoka, H.; Sato, K.; Shiomi, D.; Takui, T. *Appl. Magn. Reson*. **2003**, *23*, 517–538. (c) Astashkin, A. V.; Schweiger, A. *Chem. Phys. Lett*. **1990**, *174*, 595–602.
14. (a) Yamaguchi, K.; Fljeno, T.; *Chem. Phys. Lett*. **1989**, *159*, 465–471. (b) Kitagawa, Y.; Saito, T.; Ito, M.; Shoji, M.; Koizumi, K.; Yamanaka, S.; Kawakami, T.; Okumura, M.; Yamaguchi, K. *Chem. Phys. Lett*. **2007**, *442*, 445–450. (c) Yamaguchi, K.; Okumura, M.; Mori, W.; Maki, J.; Takada, K.; Noro, T.; *Chem. Phys. Lett*. **1993**, *210*, 201–210.
15. Kitagawa, Y.; Saito, T.; Yamaguchi, K. *In Symmetry (Group Theory) and Mathematical Treatment in Chemistry, Editor*: Akitsu, T., IntechOpen, **2018**, chapter 7.
16. Kitagawa, Y.; Saito, T.; Nakanishi, Y.; Kataoka, Y.; Matsui, T.; Kawakami, T.; Okumura, M.; Yamaguchi, K. *J. Phys. Chem. A*. **2009**, *113*, 15041–15046.
17. Bleaney, B.; Bowers, K.D. *Proc. R. Soc. A* **1952**, *43*, 372−374.

Acknowledgement of this chapter.

This work was supported by JSPS KAKENHI Grant Number 22J10450. Manabu Abe. acknowledges financial support from JSPS KAKENHI (grant nos. JP17H03022, 20K21197, 21H01921, and 22K19033) and JST CREST (grant no. JPMJCR18R4). Mass and single-crystal XRD measurements were performed at the Natural Science Center for Basic Research and Development (N-BARD) of Hiroshima University. Yasutaka Kitagawa. acknowledges financial support from JSPS KAKENHI (grant nos. JP21H01951 and JP22H02050) and QIQB, ICS-OTRI, and ICS- SRN at Osaka University.

Chapter 4. Summary and Outlook

Cycloparaphenylene (CPP), in which all benzene rings are connected at the para position to form a ring structure, has been reported to have a unique HOMO-LUMO energy gaps. In the case of linear paraphenylene molecules, when the number of benzene rings in the molecule increases, the conjugated system expands, and the energy gap becomes smaller. While in the case of CPP, the HOMO-LUMO gap becomes smaller as the number of benzene rings decreases. This behavior is caused by an increase in the contribution of the quinoidal form due to spin interactions induced by distortion of the benzene ring in the macrocyclic structure. In this study, we focused on multiradical in the curved structure (macrocyclic structure) and revealed the behavior and spin-spin interaction of multiradical. Multiradical within bend structure were found to form singlet ground state and to be more reactive than linear one. In addition, diradical molecules with small ring size were found to have a unique in-plane aromaticity generated by the quinoidal form and the homoconjugation was revealed. The results of this study will lead to the elucidation of new photo- and electronic properties of quinoidal chemical species. The curved quinoidal chemical species are expected to have high redox activity and photo-response in visible and near infrared region due to have a smaller HOMO-LUMO gap than those with linear structures. They are expected to be used for organic conductors, imaging materials, and redox catalysts that can easily transfer electrons.

CCC RightsLink

Sign in/Register

ACS Publications
Most Trusted. Most Cited. Most Read.

1,3-Diradicals Embedded in Curved Paraphenylene Units: Singlet versus Triplet State and In-Plane Aromaticity

Author: Yuki Miyazawa, Zhe Wang, Misaki Matsumoto, et al
Publication: Journal of the American Chemical Society
Publisher: American Chemical Society
Date: May 1, 2021

PERMISSION/LICENSE IS GRANTED FOR YOUR ORDER AT NO CHARGE

This type of permission/license, instead of the standard Terms and Conditions, is sent to you because no fee is being charged for your order. Please note the following:

- Permission is granted for your request in both print and electronic formats, and translations.
- If figures and/or tables were requested, they may be adapted or used in part.
- Please print this page for your records and send a copy of it to your publisher/graduate school.
- Appropriate credit for the requested material should be given as follows: "Reprinted (adapted) with permission from {COMPLETE REFERENCE CITATION). Copyright {YEAR} American Chemical Society." Insert appropriate information in place of the capitalized words.
- One-time permission is granted only for the use specified in your RightsLink request. No additional uses are granted (such as derivative works or other editions). For any uses, please submit a new request.

If credit is given to another source for the material you requested from RightsLink, permission must be obtained from that source.

BACK CLOSE WINDOW

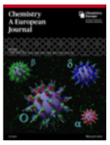

Generation and Characterization of a Tetraradical Embedded in a Curved Cyclic Paraphenylene Unit

Author: Yuki Miyazawa, Zhe Wang, Sayaka Hatano, et al
Publication: Chemistry - A European Journal
Publisher: John Wiley and Sons
Date: Jun 16, 2023

Order Completed

Thank you for your order.

This Agreement between Hiroshima university -- Yuki Miyazawa ("You") and John Wiley and Sons ("John Wiley and Sons") consists of your license details and the terms and conditions provided by John Wiley and Sons and Copyright Clearance Center.

Your confirmation email will contain your order number for future reference.

License Number	5684450195624
License date	Dec 08, 2023

Printable Details

Licensed Content

Licensed Content Publisher	John Wiley and Sons
Licensed Content Publication	Chemistry - A European Journal
Licensed Content Title	Generation and Characterization of a Tetraradical Embedded in a Curved Cyclic Paraphenylene Unit
Licensed Content Author	Yuki Miyazawa, Zhe Wang, Sayaka Hatano, et al
Licensed Content Date	Jun 16, 2023
Licensed Content Volume	29
Licensed Content Issue	42
Licensed Content Pages	9

Order Details

Type of use	Dissertation/Thesis
Requestor type	Author of this Wiley article
Format	Print and electronic
Portion	Full article
Will you be translating?	No

Acknowledgements of my research

The studies described in this thesis have been conducted under the direction of Professor Manabu Abe at the research group of reaction organic chemistry of Department of Chemistry, Graduate School of Advanced Science and Engineering, Hiroshima University.

Special thanks to Japan Society for the Promotion of Science (JSPS) and Japan Science and Technology Agency (JST) for supporting our research fund and living expenses in a doctoral program.

I am deeply indebted to Professor Manabu Abe for his helpful discussions, experimental guidance and advice, contribution to the revision of the manuscripts, and so on. I am also grateful to Dr. Sayaka Hatano and Dr. Ryukichi Takagi for valuable discussions, assistance with synthesis and measurements, revising the manuscripts, and so on. In addition, I would like to thank all the lab members of Reaction Organic Chemistry for helping with my experiments, some discussions, and relieving stress.

I would like to acknowledge the invaluable support offered by Mrs. Tomoko Amimoto and Mrs. Naomi Kawata from Natural Science Center for Basic Research and Development (N-BARD), Hiroshima University, for providing a high-resolution (HR) mass spectrometer and single-crystal X-ray diffraction analysis.

I appreciate the discussion and supporting on my research study from Professor Shigeru Yamago and Dr. Eiichi Kayahara from Kyoto University.

I appreciate the supporting of the theoretical calculation on my research study from Dr. Ivana Antol from Ruđer Bosǩović Institute.

I thankful to Dr. Hideto Matsuoka at Osaka Metropolitan University for their helpful discussion about the spin state of tetraradical and EPR measurement.

I thankful to Dr. Yasutaka Kitagawa at Osaka university for their helpful discussion about the spin state of tetraradical and theoretical calculation.

I would like to express my deep gratitude to my family, Shigehiro, Akiko, Takako, Tomoko, Sho, Miyu, and house cat (Tora, Moa) for their kind continuous encouragement and support of my college life in Hiroshima for a long time.

Yuki Miyazawa